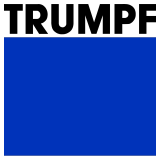

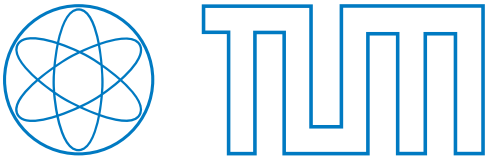

Lehrstuhl für Laser- und Röntgenphysik E11

Thin-disk laser pumped high-energy few-cycle OPCPA

Stephan Prinz

Vollständiger Abdruck der von der Fakultät für Physik der Technischen Universität München zur Erlangung des akademischen Grades eines

Doktors der Naturwissenschaften (Dr. rer. nat.)

genehmigten Dissertation.

Vorsitzender:		Prof. Dr. Frank Pollmann
Prüfer der Dissertation:	1.	Prof. Dr. Reinhard Kienberger
	2.	Prof. Dr. Franz Pfeiffer

Die Dissertation wurde am 11.04.2018 bei der Technischen Universität München eingereicht und durch die Fakultät für Physik am 26.10.2018 angenommen.

Kurzzusammenfassung

Energetische Pulse mit wenigen optischen Zyklen bei gleichzeitig hohen Repetitionsraten werden heutzutage standardmäßig im Bereich der Ultrakurzzeitphysik eingesetzt und sind die Grundlage wegweisender Anwendungen in verschiedensten Fachgebieten. Üblicherweise werden solche Pulse in Titan-Saphir-basierten Verstärkersystemen erzeugt, die jedoch aufgrund des hohen Quantendefekts im Lasermedium sowie durch die verstärkungsbedingte Bandbreitenreduktion eine grundsätzliche Beschränkung aufweisen. Der weitere Fortschritt in der Ultrakurzzeitphysik ist deshalb abhängig von der Entwicklung neuartiger Laserquellen mit gleichzeitig hoher Energie, mittlerer Leistung und kompakter Baugröße.

In dieser Arbeit werden Entwurf, Aufbau und Anwendung eines hochenergetischen optisch-parametrischen Verstärkersystems mit Pulsdauern von nur wenigen optischen Zyklen vorgestellt. Dieses System ist in der Lage, moderne Titan-Saphir-Verstärker in heutigen Standardanwendungen gleichwertig zu ersetzen oder sogar zu übertreffen. Dank der einzigartigen Eigenschaften des parametrischen Verstärkungsprozesses wie etwa hohe Verstärkungsfaktoren, direkte breitbandige Verstärkung sowie minimale thermische Effekte bietet diese Technologie ein hohes Potential für die zukünftige Skalierbarkeit von Pulsenergie und mittlerer Leistung. Mit Ausnahme des kommerziellen Titan-Saphir-Oszillators, welcher hier als Ausgangsstrahlquelle (auch als *Seedlaser* bezeichnet) genutzt wird, wurden alle benötigten Subsysteme eigens im Rahmen dieser Arbeit entwickelt.
Die hochenergetischen Pumppulse werden in einem regenerativen Verstärker, basierend auf einer Ytterbium-dotierten dünnen Scheibe als aktives Medium, erzeugt. Bei einer Pumpwellenlänge von 969 nm und einer Pumpleistung von 400 W wird eine Ausgangsleitung von bis zu 170 W erreicht, was bei einer Repetitionsrate von 6 kHz einer Pulsenergie von 28 mJ entspricht. Mit Pulsdauern von etwa 1 ps sowie einer nahezu beugungsbegrenzten Strahlqualität ist das System hervorragend als Pumpquelle für den optisch parametrischen Verstärker geeignet.
Da zeitliche Fluktuationen zwischen den Pump- und Seedpulsen die Stabilität der parametrischen Verstärkung stark beeinflussen, wurde ein aktives Pulsstabilisierungssystem entwickelt, welches nur einen Bruchteil der Gesamtenergie von Pump- und Seedlaser benötigt. Die Pulsankunftszeiten können nun mit einer verbleibenden Standardabweichung von weniger als 3 fs genau kontrolliert werden, wobei gleichzeitig ein Messbereich von 20 ps abgedeckt wird.
Pump- und Seedpulse interagieren letztendlich in einem dreistufigen optisch-parametrischen Verstärker und erzeugen dadurch Pulsenergien von mehr als 1.8 mJ bei einer hohen mittleren Leistung von über 10 W und Repetitionsraten von 6 kHz. Pulse mit stabiler Träger-

Einhüllenden-Phase und Pulsdauern um die 7 fs werden erreicht, was weniger als drei optischen Zyklen entspricht und Pulsspitzenleistungen von >160 GW ermöglicht. Nichtlineare Effekte in Luft beeinflussen das Gesamtverhalten des Systems und werden durch ein speziell angepasstes optisches Design minimiert. Die erzeugten Parameter in Kombination mit exzellenter Langzeitstabilität sowie der kompakten Gesamtgröße erlauben es, bestehende Titan-Saphir-Verstärker ohne Weiteres durch das im Rahmen dieser Arbeit entwickelte optisch-parametrische Verstärkersystem zu ersetzen. Dies wird durch eine erste experimentelle Anwendung bestätigt, bei der erfolgreich die Erzeugung hoher Harmonischer in Neon demonstriert wird.

Abstract

Energetic pulses in the few-cycle regime at high repetition rates are nowadays routinely used in ultrafast science and enable a number of groundbreaking applications in the fields of physics, chemistry and lifescience. Usually, these pulses are provided by Titanium-sapphire-based amplifiers. However, these systems face fundamental limitations in average power and pulse duration due to the high quantum defect of the laser material and unavoidable spectral gain narrowing. Thus, further progress in ultrafast science can only be achieved by a new generation of energetic, powerful and compact laser sources.

In this work, the design, setup and application of a high-energy few-cycle optical parametric chirped pulse amplification (OPCPA) system is presented which is able to replace or even outperform existing state-of-the-art Titanium-sapphire amplifiers in routine applications. Thanks to the unique properties of the parametric process such as high gain, broadband amplification and minimum thermal effects, this technology offers excellent prospects for future power- and energy scalability. Apart from the commercial Titanium-sapphire oscillator used as the master seed source, all major subsystems are developed in the context of this thesis.

The energetic pump-pulses are generated in a regenerative amplifier, utilizing an Ytterbium-doped thin-disk as the active medium. Pumped at 969 nm with up to 400 W, output powers as high as 170 W are obtained, corresponding to >28 mJ at a repetition rate of 6 kHz. With pulse durations around 1 ps, near-diffraction limited beam quality and excellent long-term stability, this system is ideally suited to pump the OPCPA.

Because timing fluctuations between pump and seed pulses significantly impair the performance of the parametric amplifier, an active pump-seed synchronization system is developed. Only minor fractions of the total pump and seed energy are necessary to lock the pulse arrival times with a remaining standard deviation of less than 3 fs, featuring a detection range of 20 ps at the same time.

Finally, pump and seed pulses interact in a three-stage OPCPA which yields pulse energies of >1.8 mJ combined with a high average power above 10 W at 6 kHz repetition rate. Carrier-envelope-phase-stable pulses with sub-3 cycle pulse durations around 7 fs are generated, resulting in peak powers exceeding 160 GW. The overall performance is affected by the onset of nonlinear effects in air, which are consequently minimized by an adapted system design. The achieved parameters paired with an excellent long-term stability and table-top size allow the system to readily replace existing Titanium-sapphire amplifiers. This is underlined by a first proof-of-principle experiment, demonstrating high-harmonic generation in Neon.

Contents

1. Introduction **1**

1.1. Structure of the Thesis 2

2. Theoretical Foundations **5**

2.1. Nonlinear Optical Susceptibility and Polarization 5

2.2. Optical Parametric Amplification 6

2.2.1. Coupled Wave Equations 7

2.2.2. Phase Matching 8

2.2.3. Optical Parametric Chirped Pulse Amplification 9

2.3. Higher Order Processes 10

2.3.1. Optical Kerr Effect 10

2.3.2. B-Integral 11

2.4. Ultrashort Pulses 12

2.4.1. Dispersion 12

2.4.2. Carrier-Envelope Phase 12

2.5. High Harmonic Generation 13

2.5.1. The Three-Step Model 14

3. Seed Source **17**

3.1. venteon dual CEP 17

4. Thin-Disk Regenerative Amplifier **21**

4.1. Short-Pulsed Picosecond Pumping 21

4.2. Yb-based Thin-Disk Laser Head 22

4.3. Regenerative Amplifier 24

4.4. Cavity Design and CPA 25

4.5. Experimental Setup 28

4.6. Pulse Amplification Dynamics 30

4.7. Beam Quality 31

4.8. Temporal Pulse Contrast 33

4.9. Long-term Performance 36

4.10. Second Harmonic Generation 37

4.11. Summary 38

5. Pump-Seed Synchronization **41**
5.1. Motivation . . . 41
5.2. Pulse Delay Measurement . . . 42
5.2.1. Intensity Cross-Correlation . . . 42
5.2.2. Balanced Optical Cross-Correlation . . . 43
5.2.3. Spectrally Resolved Cross-Correlation . . . 44
5.3. Experimental Implementation . . . 45
5.3.1. Optical Setup . . . 45
5.3.1.1. Error Signal Generation . . . 45
5.3.1.2. Error Signal Characterization . . . 47
5.3.1.3. Error Signal Measurement . . . 48
5.3.2. Electronics . . . 50
5.3.3. Calibration . . . 52
5.4. Results . . . 54
5.4.1. Synchronization . . . 55
5.4.1.1. Short-term Timing Jitter . . . 55
5.4.1.2. Spectral Analysis . . . 56
5.4.1.3. Out-of-loop Performance . . . 56
5.4.2. Beam Pointing Influence . . . 57
5.5. Summary and Outlook . . . 58

6. Optical Parametric Chirped Pulse Amplifier **61**
6.1. General Design Considerations . . . 61
6.1.1. Nonlinear Crystal Choice . . . 61
6.1.2. Dispersion Management . . . 62
6.2. Preamplification . . . 64
6.2.1. Simulation . . . 65
6.2.1.1. Parametric Superfluorescence . . . 66
6.2.1.2. Seed Chirp . . . 69
6.2.2. Experiment . . . 69
6.3. Challenges at High Peak Powers . . . 71
6.4. Concept A: Pump Recycling . . . 74
6.4.1. Experimental Setup . . . 74
6.4.2. Experimental Results . . . 74
6.4.3. Summary . . . 75
6.5. Concept B: Individual Pumping . . . 75
6.5.1. Experimental Setup . . . 75
6.5.2. Parametric Amplification . . . 76
6.5.3. Pulse Compression . . . 78
6.5.4. Summary . . . 79
6.6. Concept C: Multiple SHG Stages . . . 80
6.6.1. Experimental Setup . . . 80
6.6.2. Second Harmonic Generation . . . 80

6.6.3. Parametric Amplification . . . 81
6.6.4. Pulse Compression . . . 85
6.6.5. Long-Term Performance . . . 87
6.6.6. Summary . . . 88
6.7. Carrier-Envelope Phase . . . 89
6.8. OPCPA Output Characteristics . . . 91
6.8.1. Beam Caustic . . . 91
6.8.2. Spatial Chirp . . . 93
6.8.3. Temporal Contrast . . . 93
6.9. Summary . . . 94

7. High Harmonic Generation **97**
7.1. Experimental Setup . . . 97
7.2. Results . . . 100
7.2.1. HHG Spectrum . . . 100
7.2.2. CEP Dependency . . . 101
7.3. Summary . . . 101

8. Conclusion **103**

9. Outlook **107**

List of figures **111**

List of tables **113**

List of acronyms **116**

Bibliography **117**

Appendix **129**
A. Measurement Devices . . . 129
B. THG-Autocorrelator . . . 130

1. Introduction

The advancement of laser sources delivering ultrashort laser pulses comprising only a few optical cycles enabled a revolution in ultrafast science during the past decades. In 1985, 27 fs-short pulses were generated in a dye laser oscillator for the first time [110]. Only one year later, Titanium-sapphire (Ti:Sa) oscillators were introduced [62] and quickly took over the field. Nowadays, they provide sub-two cycle pulse durations as short as 5 fs directly from the oscillator [25] and favour low-energy applications such as high-resolution multiphoton spectroscopy [122]. A step towards higher pulse energies and peak powers was achieved by Ti:Sa-based amplifiers. Combined with nonlinear pulse shortening techniques and a controlled carrier-envelope phase (CEP) they opened a whole new field of research - attosecond science [49]. The first demonstration of an isolated attosecond pulse in 2001 from a spectrally broadened Ti:Sa-amplifier delivering 0.5 mJ, 7 fs-short pulses at 1 kHz [37] paved the way for metrology on the attosecond timescale and facilitated unprecedented observation and control of electron dynamics in atoms, molecules, ions and solids [65, 94]. Since then, Ti:Sa-amplifiers have been the workhorse for ultrafast science, enabling further groundbreaking applications such as time-resolved spectroscopy on a femtosecond scale (e.g. transient absorption spectroscopy [10], fluorescence spectroscopy [123] or photoelectron spectroscopy [95]), high-harmonic generation [51], laser wakefield acceleration [73] or ultrafast material ablation [66]. Today, typical Ti:Sa-based laser systems offer a few tens of milijoules at repetition rates around 1 kHz [1]. Due to gain narrowing, pulse durations are limited to around 20 - 30 fs, requiring nonlinear spectral broadening techniques such as gas-filled hollow-core fibers [64] to restore few-cycle pulse durations.
A further leap in the development of Ti:Sa-amplifiers seems unlikely out of two main reasons. On the one hand, the comparably high quantum defect of Ti:Sa (typically >30 %) hampers scaling of average power as a result of thermally induced distortions. On the other hand, the damage threshold of hollow-core fibers ultimately limits the achievable pulse energy in the few-cycle regime to a few mJ [13]. Thus, only new laser sources based on different technologies can spark the next revolution in ultrafast science.

On the route towards higher energies at multi-kHz repetition rates, the concept of optical parametric chirped pulse amplification (OPCPA) has the potential to substantially extend the parameter limits. Based on a second-order nonlinear three-wave mixing process, the energy of a strong pump beam is transferred to a weak seed beam under generation of a so-called idler. Direct amplification of large bandwidths with high gain is enabled, simultaneously preserving the CEP of the seed pulses [5]. The instantaneous nature of the process reduces thermal effects inside the nonlinear medium and allows for high power pumping with excellent prospects for average power scalability. With the advent of innovative solid-state laser concepts such as Ytterbium-based Fiber-, Slab- and Thin-disk lasers, average pumping powers approaching the kW-level are becoming available right now [68] and are ready to unlock the potential of OPCPA.
Some important milestones of OPCPA technology have been achieved so far. Parametric amplification of ultrabroad bandwidths has been demonstrated already in 2002 by Baltuška et al. who realized a 4 fs-short pulse utilizing an angular dispersed broadband pump beam [6]. Output powers as high as 22 W at 1 MHz repetition rate (22 µJ of pulse energy) [82] and 15 W at 300 kHz (50 µJ) have been obtained in the last years [72], essentially limited by the available pump power. At repetition rates as low as 10 Hz, the feasibility of pulse energies up to 130 mJ could be shown in large laser facilities [38] and recently, record values of 53 W at 1 kHz (53 mJ) were achieved by combining multiple high-energy pump sources and a total of 6 OPCPA stages [15].

In this thesis, a compact (table-top) few-cycle OPCPA system is developed with the goal in mind to replace or even outperform existing state-of-the-art Ti:Sa-amplifiers in routine operations, which is the first step in the establishment of a new technology. The targeted application is the generation of isolated attosecond pulses in the extreme ultraviolet (XUV) via high-harmonic generation (HHG), covering photon energies of 80 eV and more. For the associated experiments, pulse energies in the multi-mJ range paired with multi-kHz repetition rates are desirable to generate a high XUV photon flux and increase the signal to noise ratio [85], potentially enabling XUV-XUV pump-probe spectroscopy [100]. Direct amplification of CEP-stable sub-3 cycle pulses (<8 fs at 800 nm) is envisaged which theoretically allows to produce a XUV continuum with >8 eV bandwidth, supporting an isolated 500 as-pulse [8].

1.1. Structure of the Thesis

This manuscript is structured as follows: The next chapter introduces the relevant theoretical foundations. Nonlinear interactions of second and higher order are explained, with emphasis on parametric amplification and its associated properties. Afterwards, essential features of ultrashort pulses such as the role of dispersion and CEP are discussed.
After the theoretical part, the design, setup and characterization of the complete OPCPA system is presented, subdivided into the different core components according to figure 1.1.

Chapter 3 starts with the introduction of the master seed source, a commercial Ti:Sa-oscillator, which simultaneously provides the seed pulses for the OPCPA and the pump

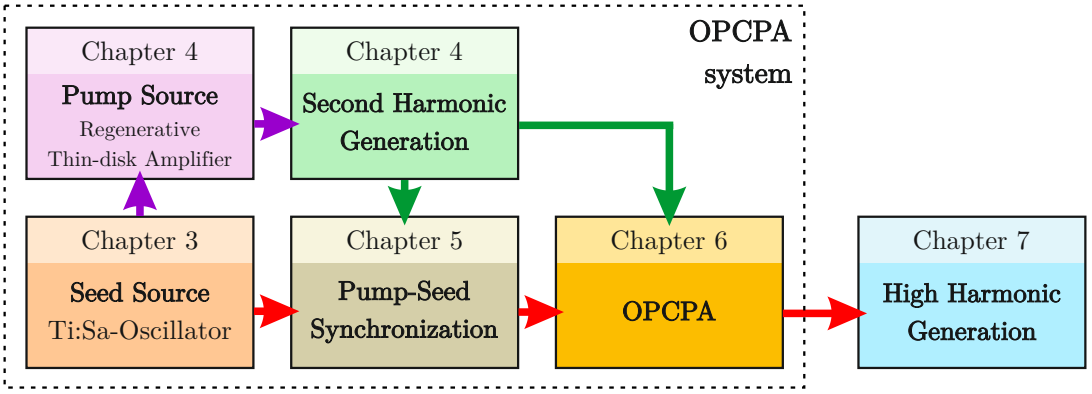

Figure 1.1.: Simplified relationship between the core components of the OPCPA system and the resulting structure of this thesis. The core components are presented in chapters 3 to 6. The application of the system for HHG is presented in chapter 7.

laser.

The development of the pump source is described in chapter 4. First, the benefits of utilizing ∼1 ps-short pump pulses in the parametric amplification process are elucidated, followed by the design and implementation of the Ytterbium-based thin-disk regenerative amplifier. A complete characterization of all relevant parameters is provided. Second-harmonic generation finally converts the pulses to the appropriate pump wavelength of 515 nm, where a significant increase in conversion efficiency could be achieved by improving the temporal pulse contrast of the fundamental beam.

To lock the temporal overlap of pump and seed pulses in time, an innovative pump-seed synchronization system is presented in chapter 5. A method to measure and control the timing offset with femtosecond precision covering a detection range of 20 ps is introduced which requires only a few picojoule of seed pulse energy. The performance of the feedback loop is analyzed in detail and guarantees exact timing of the pulse arrival times in the parametric amplification stages.

In chapter 6, the parametric amplification of the seed pulses towards the mJ-level is treated. General design considerations of a high-energy few-cycle OPCPA are followed by the simulation and implementation of the preamplification stage. Challenges at high peak powers, arising from nonlinear effects in air affecting the pump beam are pointed out. After that, three different system designs are realized, in which the nonlinearities are gradually reduced to achieve the desired performance. At the end of the chapter, the properties of the OPCPA are carefully characterized.

The first experimental application of the system is presented in chapter 7. High-harmonic generation up to the 61st order is demonstrated in Neon, yielding photon energies of 93 eV. Additionally, the characteristic CEP-dependency of the produced spectrum is verified.

A summary of the complete system performance and an overview of potential improvements are finally given in chapters 8 and 9 and complete this work.

2. Theoretical Foundations

This chapter provides basic insight about the most important and for this thesis relevant theroetical foundations in the field of ultrashort pulses. For more details, the interested reader is kindly refered to [14, 16, 106] and [116], which form the basis of this chapter.

2.1. Nonlinear Optical Susceptibility and Polarization

If an optical field with strength $E(t)$ is applied to a material, the induced dipole moment per unit volume, also known as the polarization $P(t)$, can be expressed as

$$\begin{aligned} P(t) &= \epsilon_0 \left[\chi^{(1)} E(t) + \chi^{(2)} E^2(t) + \chi^{(3)} E^3(t) + \dots \right] \\ &\equiv P^{(1)}(t) + P^{(2)}(t) + P^{(3)}(t) + \dots . \end{aligned} \tag{2.1}$$

In this equation, $\chi^{(1)}$ denotes the linear susceptibility, $\chi^{(2)}$, $\chi^{(3)}$ the second- and third-order nonlinear susceptibility and ϵ_0 the permittivity of free space. In linear optics, only the linear polarization $P^1(t) = \epsilon_0 \chi^{(1)} E(t)$ is considered. In nonlinear optics, on the other hand, processes such as second-harmonic generation (SHG), sum-frequency generation (SFG) and difference-frequency generation (DFG)/optical parametric amplification (OPA) are induced by second-order nonlinear polarization $P^2(t) = \epsilon_0 \chi^{(2)} E^2(t)$ or, in case of e.g. third-harmonic generation (THG), self-phase modulation (SPM) and cross-polarized wave generation (XPW), by third-order nonlinear polarization $P^3(t) = \epsilon_0 \chi^{(3)} E^3(t)$. The sum of all higher-order polarization components is referred to as the nonlinear polarization P_{NL}. If, for example, two optical waves with frequencies ω_1 and ω_2 and a combined optical field

$$E(t) = E_1 e^{-i\omega_1 t} + E_2 e^{-i\omega_2 t} + \text{c.c.} \tag{2.2}$$

propagate through a medium with $\chi^{(2)} \neq 0$, a nonlinear polarization according to equation 2.1 leads to the generation of new frequencies:

$$P^{(2)}(t) = \epsilon_0 \chi^{(2)} \Bigg[\underbrace{E_1^2 e^{-2i\omega_1 t}}_{\text{SHG}} + \underbrace{E_2^2 e^{-2i\omega_2 t}}_{\text{SHG}} + \underbrace{2E_1 E_2 e^{-i(\omega_1+\omega_2)t}}_{\text{SFG}} + \underbrace{2E_1 E_2^* e^{-i(\omega_1-\omega_2)t}}_{\text{DFG, OPA}} + \text{c.c.} \Bigg] + \dots . \tag{2.3}$$

Considering a real nonlinear medium, e.g. a nonlinear optical crystal with losses and/or dispersion, electric field and polarization can no longer be described as a scalar but must be represented as vectors in three-dimensional space with indices i,j and k to take the crystal properties into account. The second-order susceptibility then becomes a tensor $\chi^{(2)}_{ijk}$ and the second-order nonlinear polarization is expressed as

$$P_i(\omega_n + \omega_m) = \epsilon_0 \sum_{j,k} \sum_{(m,n)} \chi^{(2)}_{ijk} E_j(\omega_n) E_k(\omega_m). \tag{2.4}$$

For a fixed geometry, the nonlinear polarization giving rise to a specific second-order nonlinear process can be expressed again by a scalar relationship, as e.g. for SFG

$$P(\omega_3) = 4\epsilon_0 d_{\text{eff}} E(\omega_1) E(\omega_2), \tag{2.5}$$

introducing the effective nonlinear optical coefficient d_{eff}. Using d_{eff} allows an easy calculation of the fields and an intuitive comparison between different crystals.

2.2. Optical Parametric Amplification

OPA is an instantaneous three-wave mixing process that allows for the direct amplification of ultrashort pulses thanks to a large supported bandwidth, depending on the choice of amplification medium. The process is illustrated schematically in figure 2.1 and can be considered as a repeated DFG process, in which energy from the so-called *pump* beam with frequency ω_1 is transferred to an incident *signal* beam with frequency ω_2 under the generation of an *idler* beam with frequency $\omega_3 = \omega_1 - \omega_2$ to satisfy the energy conservation law

$$\hbar\omega_1 = \hbar\omega_2 + \hbar\omega_3, \tag{2.6}$$

where $\hbar$ represents the Planck constant. As the beams propagate through the gain medium, the presence of the idler now promotes the generation of new signal photons, since for every new ω_3 photon stimulating the DFG process a matching ω_2 photon is produced and vice versa. Simultaneously, a pump photon at $\omega_1 > \omega_2, \omega_3$ is destroyed, giving rise to an exponential growth. For an efficient interaction, also the momentum conservation (or phase matching condition)

$$\hbar\vec{k_1} = \hbar\vec{k_2} + \hbar\vec{k_3} \tag{2.7}$$

has to be fulfilled, where $\vec{k_1}$, $\vec{k_2}$ and $\vec{k_3}$ are the wave vectors of pump, signal and idler, respectively.

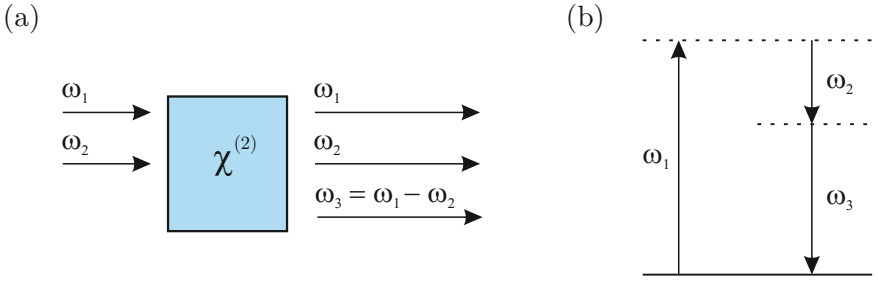

Figure 2.1.: DFG/OPA (a) interaction geometry and (b) energy-level description.

Compared to DFG, the pump in OPA is typically much stronger than the seed which is to be amplified, and the generated idler is usually of no interest. In the context of OPA and in this thesis, the indices for pump, signal and idler are changed to $1 \rightarrow p$, $2 \rightarrow s$ and $3 \rightarrow i$, respectively to allow an intuitive identification.

2.2.1. Coupled Wave Equations

Under the assumption of three linearly polarized, monochromatic waves at frequencies $\omega_p > \omega_s > \omega_i$ with amplitudes A_p, A_s and A_i and within the slowly-varying-envelope approximation ($|d^2A/dz^2| \ll 2k|dA/dz|$), the following coupled wave equations can be derived to describe the (collinear) propagation along z in a medium with second-order nonlinear polarization:

$$\frac{dA_p}{dz} = -i\frac{\omega_p d_{\text{eff}}}{n_p c_0} A_i A_s e^{i\Delta kz}, \tag{2.8}$$

$$\frac{dA_s}{dz} = -i\frac{\omega_s d_{\text{eff}}}{n_s c_0} A_i^* A_p e^{-i\Delta kz}, \tag{2.9}$$

$$\frac{dA_i}{dz} = -i\frac{\omega_i d_{\text{eff}}}{n_i c_0} A_s^* A_p e^{-i\Delta kz}. \tag{2.10}$$

Here, n denotes the refractive index of the medium at the respective frequency. The term $\Delta k = k_p - k_s - k_i$ is the so-called wave-vector mismatch in the case of non-perfect phase matching, as described by equation 2.7. Without pump depletion ($A_p \cong$ const.) and under the assumption of an initial signal intensity $I_{s,0}$ (referred to as the seed beam) and no initial idler ($A_i = 0$), the coupled wave equations can be solved analytically to calculate signal and idler intensities after a length L of the nonlinear medium:

$$I_s(L) = I_{s,0}\left[1 + \frac{\Gamma^2}{g^2}\sinh^2(gL)\right], \tag{2.11}$$

$$I_i(L) = I_{s,0}\frac{\omega_i}{\omega_s}\frac{\Gamma^2}{g^2}\sinh^2(gL), \tag{2.12}$$

where

$$g = \sqrt{\Gamma^2 - \left(\frac{\Delta k}{2}\right)^2} \tag{2.13}$$

is the small signal gain and

$$\Gamma^2 = \frac{\omega_i \omega_s d_{\text{eff}}^2 |A_p|^2}{n_i n_s c_0^2} = \frac{8\pi^2 d_{\text{eff}}^2 I_p}{n_i n_s n_p \lambda_i \lambda_s \epsilon_0 c_0}. \tag{2.14}$$

is known as the nonlinear coefficient.

Usually, those boundary conditions are not fulfilled in a real OPA system and numerical simulations have to be used to solve the coupled wave equations in order to describe the parametric process more precisely. For this purpose, the software *Chi2D* [50] is utilized in the context of this thesis.

2.2.2. Phase Matching

Fulfilling the condition of momentum conservation stated by equation 2.7 requires the wave-vector mismatch to become zero, $\Delta k = 0$, which can be recast in the form

$$n_p \omega_p = n_i \omega_i + n_s \omega_s. \tag{2.15}$$

Because this condition cannot be satisfied in isotropic materials with normal dispersion ($n_p > n_s > n_i$), birefringent crystals in combination with perpendicular polarized beams are utilized. Two types of phase matching are distinguished: in *type I* phase matching, both signal and idler have the same polarization, perpendicular to the pump, while in *type II* phase matching, one of the two is polarized in parallel to the pump.
The phase matching condition is usually achieved by adjusting the angle θ between the wave vector of the propagating beams and the optical axis of the medium, known as angular phase matching. Another possibility is a change of the crystal temperature to adjust the refractive indices, called temperature phase matching.

In the collinear configuration, the amplification bandwidth is limited by the group-velocity mismatch (GVM) between signal and idler. This means that in this case, the largest bandwidth can be achieved at degeneracy ($\omega_s = \omega_i$). However, the bandwidth can be significantly increased by utilizing a noncollinear configuration, where an angle between signal and idler is set such that the signal group velocity matches the projected idler group velocity along the signal direction. This condition can be transferred to an equivalent angle α between pump and signal, which in practical applications is more convenient to use. The noncollinear interaction geometry is schematically depicted in figure 2.2 (a). Applying the cosine rule, Δk can be calculated according to

$$\Delta k = \sqrt{k_p^2 + k_s^2 - 2 k_p k_s \cos\alpha} - k_i. \tag{2.16}$$

Figure 2.2 (b) shows the example of a type I OPA, utilizing β-barium borate, $Ba(BO_2)_2$ (BBO) as nonlinear medium pumped at $\lambda_p = 515\,\text{nm}$ under different angles θ. At $\theta = 24.5°$, broadband phase matching is achieved in a bandwidth between 700 nm and 900 nm under a noncollinear pump-seed angle of $\alpha = 2.5°$. This angle of broadband perfect phase matching is often referred to as the *magic angle*.

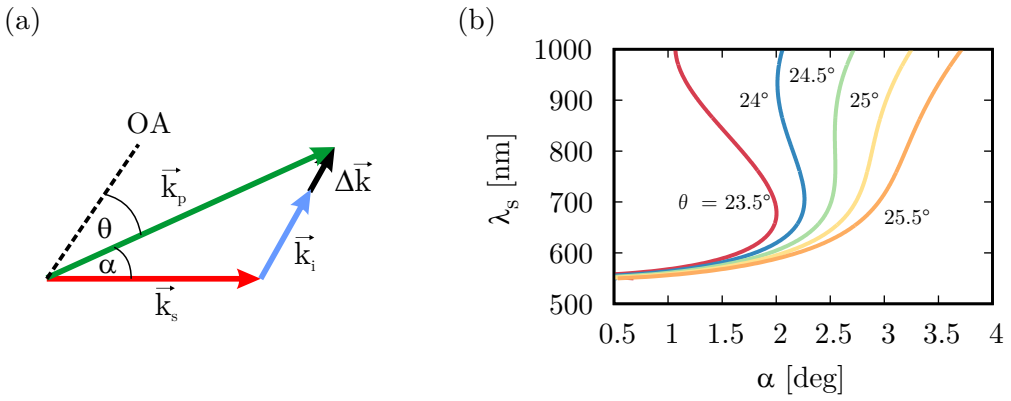

Figure 2.2.: (a) Interaction geometry in the noncollinear configuration. OA: optical axis. (b) Phase matching curves for a noncollinear type I BBO-based OPA pumped at 515 nm under different angles θ.

Phase Matching Geometries

In negative uniaxial crystals ($n_e < n_o$), the Poynting vector of the extraordinary wave points to a different direction than the propagation vector due to birefringence. Thus, the energy is distributed away from the optical axis, which is known as *walk-off*.
In the previous example of a noncollinear type I BBO-based OPA with an extraordinary polarized pump wave, two amplification geometries result:

- *Poynting-vector-walk-off compensation geometry (PVWC)*
  In Poynting-vector-walk-off compensation (PVWC) geometry, the pump walk-off is towards the signal beam, partially compensating the angular displacement between both beams, effectively enhancing the interaction length. One drawback arises from the parasitic phase matched SHG of signal and idler, which limits the conversion efficiency and eventually distorts the spectral phase of the amplified signal.

- *Tangential-phase matching geometry (TPM)*
  In tangential-phase matching (TPM) geometry, the pump walk-off is away from the signal. Thus, the spatial overlap of the involved beams is lost much faster than in PVWC geometry. This can result in a deterioration of the beam quality. Consequently, the choice of a suitable interaction geometry always depends on the parameter regime of the OPA. A good comparison between different scenarios is given in [108].

2.2.3. Optical Parametric Chirped Pulse Amplification

As the name suggests, OPCPA adds the concept of chirped-pulse amplification (CPA) [96] to the parametric amplification process. Prior to entering the nonlinear medium, the seed pulses are stretched in time to a significant fraction of the pump in order to increase conversion efficiency and avoid unwanted nonlinearities. The choice of a proper pulse length has to be performed with great care. A seed pulse that is too long will suffer from insufficient amplification of the spectral wings which results in a loss of bandwidth. On the other hand, a very short pulse will be amplified with only low efficiency, causing rise of

parametric superfluorescence (PSF) in the non-overlapping parts of the pump-pulse window.
Another challenge is the recompression of the amplified signal, which requires compensation of the accumulated phase in the OPCPA chain. This is not an easy task, as especially higher-order parametric phase components introduced by a phase mismatch in the OPA process can significantly distort the compressed pulse shape [21]. Eventually, this can only be compensated by adaptive phase-shaping devices.

Throughout this thesis, the terms OPA and OPCPA are used equivalently to describe the parametric amplification process.

2.3. Higher Order Processes

The polarization of a material described by equation 2.1 also contains components of third order,

$$P^3(t) = \epsilon_0 \chi^{(3)} E^3(t). \tag{2.17}$$

In the general case of a non-monochromatic electric field, this expression becomes very complicated, but reveals a variety of interesting higher-order effects caused by the third-order suceptibility $\chi^{(3)}$. Those processes can be referred to as four-wave mixing (FWM) effects, since four waves (that may be degenerate) are involved in the interaction. Unlike in second-order processes, where some kind of anisotropy in the medium is required for $\chi^{(2)} \neq 0$, third order processes occur in virtually all media, including air. Some of the most interesting effects are described in the following.

2.3.1. Optical Kerr Effect

When an optical field with intensity $I(t)$ propagates through a medium with $\chi^{(3)} \neq 0$, the generated third-order nonlinear polarization induces a modification of the refractive index according to

$$n = n_0 + n_2 I(t), \tag{2.18}$$

where n_0 represents the common weak-field refractive index and

$$n_2 = \frac{3}{4 n_0^2 \epsilon_0 c} \chi^{(3)} \tag{2.19}$$

defines the second-order nonlinear index of refraction. This time- and frequency-dependent change of n gives rise to effects like SPM or Kerr lensing.

Self-Phase Modulation

SPM describes the time-dependent phase shift $\Phi_{\mathrm{NL}}(t)$ of an intense optical pulse with frequency ω_0 during propagation in a medium of length L,

$$\Phi_{\mathrm{NL}}(t) = -n_2 I(t) \omega_0 \frac{L}{c}. \tag{2.20}$$

This leads to a modification of the spectrum, usually in the form of spectral broadening (an increase in optical bandwidth). The leading edge of the pulse is shifted towards lower

frequencies while the trailing edge is shifted to higher frequencies. In the central part of the pulse, this corresponds to a linear chirp, while in the outer regions, new frequency components arise. Since the phase is modulated according to the temporal pulse shape, a non-ideal pulse eventually experiences undesired higher-order phase distortions, which often can not be compensated.

In the case of ultrashort pulses, SPM is the main driving mechanism for supercontinuum generation (also known as white-light generation (WLG)), i.e. the generation of pulses with very broad, often octave-spanning spectral bandwidths.

Kerr Lensing

In the spatial domain, the optical Kerr effect leads to a larger refractive index on the intense beam axis than in the peripheral regions. If $n_2 > 0$ is assumed, the material thus acts as a positive lens, causing the beam to converge and come to focus. This effect is known as Kerr lensing. Diffraction effects counteract the beam contraction, which implies that an equilibrium state exists, where the beam propagates with constant beam waist. This (highly unstable) state is called self-trapping and can occur only if the optical power exactly equals the critical power

$$P_{\mathrm{cr}} = \frac{\pi(0.61)^2\lambda_0^2}{8n_0n_2}. \tag{2.21}$$

At powers $P > P_{\mathrm{cr}}$, the beam is focused after a characteristic self-focusing distance z_f, while at $P < P_{\mathrm{cr}}$, no focus is reached. However, the general effect of a self-converging beam is observable already well below P_{cr}. A more detailed analysis is provided in chapter 6.3.

Kerr lensing can significantly increase the optical intensity and consequently lead to catastrophic damage of optical elements. Since there is no method known to increase the threshold for its onset, Kerr lensing has to be taken into consideration in the system design if it cannot be avoided.

2.3.2. B-Integral

A common measure to describe the accumulated nonlinearities of a pulse with intensity I as it propagates through a medium of length L with the nonlinear refractive index n_2 is the B-integral [70], which is defined as

$$B = \frac{2\pi}{\lambda}\int_0^L n_2(z)I(z)\,\mathrm{d}z. \tag{2.22}$$

In general, B should be kept low to avoid detrimental nonlinear effects. In praxis, the acceptable value of B depends on the application. For example, in a fiber-based CPA amplifier system, a B-Integral as high as 7 can be tolerated [80]. In a regenerative amplifier on the other hand, the value should be kept below 3 [3, 57], while in the context of this thesis, significant nonlinear effects are observed already at $B \leq 1$.

2.4. Ultrashort Pulses

Pulses with durations below a few picoseconds are commonly referred to as ultrashort pulses. Shorter pulses imply a broader spectral bandwidth and thus demand a more precise control of the dispersion in order to obtain a clean, transform-limited pulse. As pulse durations approach the few-cycle limit, a defined CEP becomes increasingly important for most applications.

2.4.1. Dispersion

Dispersion describes the phenomenon that the phase velocity of a wave depends on its optical frequency. In addition, the presence of absorptive resonances in all optical media results in a difference between phase and group velocity, called group-velocity dispersion (GVD). The effect is, that a short pulse changes its pulse shape during propagation - it is chirped.
The phase evolution of a propagating pulse in a dispersive medium is defined via the Taylor expansion of the wavenumber k as a function of the angular frequency ω around the central frequency ω_0:

$$k(\omega) = k_0 + \frac{\partial k}{\partial \omega}(\omega - \omega_0) + \frac{1}{2}\frac{\partial^2 k}{\partial \omega^2}(\omega - \omega_0)^2 + \frac{1}{6}\frac{\partial^3 k}{\partial \omega^3}(\omega - \omega_0)^3 + \dots \tag{2.23}$$

$$= k_0 + \mathrm{GD}(\omega - \omega_0) + \frac{1}{2}\mathrm{GDD}(\omega - \omega_0)^2 + \frac{1}{6}\mathrm{TOD}(\omega - \omega_0)^3 + \dots \tag{2.24}$$

The zero order term k_0 describes a common phase shift and the group delay (GD) a shift of the whole pulse shape in time. More interesting in this context are the group-delay dispersion (GDD), which gives rise to a linear chirp, and the higher-order dispersion terms such as the third-order dispersion (TOD). For very broadband spectra, higher-order terms play a significant role for the pulse compression and can no longer be neglected.

A variety of schemes exist to adjust the dispersion of a pulse. Geometrical setups like grating or prism compressor schemes offer high efficiencies and can introduce a large GDD. Chirped mirrors (Bragg-type dispersive mirrors with a spatial variation of the Bragg wavelength) are compact and convenient to use when only small GDD compensation is required. However, all aforementioned schemes lack the ability to adjust dispersion terms of different order separately and are thus only suitable for a specific design. More flexibility can be achieved by using adaptive pulse shapers [113,124], but only at the expense of transmission efficiency and system cost.

2.4.2. Carrier-Envelope Phase

The field of an optical pulse can be described in the time domain as a carrier wave multiplied with an envelope function $A(t)$:

$$E(t) = A(t)e^{i(\omega t + \varphi_{\mathrm{CEO}})}. \tag{2.25}$$

The constant phase term φ_{CEO} determines the offset of the field oscillations with respect to the pulse peak, referred to as the carrier-envelope offset phase (most often simply ab-

breviated to CEP). In relatively narrowband pulses which contain multiple optical cycles, a changing CEP has no measurable consequence. However, if the pulse comprises only a few oscillations of the electromagnetic field, a change in the CEP significantly changes the maximum electrical field strength. This is depicted schematically in figure 2.3 (a). It becomes intuitively clear, that the stabilization and control of the CEP of a few-cycle pulse is a critical precondition for any field-dependent application.
In the frequency domain, the modes of a periodic pulse train are represented by a comb of lines , equally spaced by the repetition frequency f_{rep}. The offset of the extrapolated frequency comb to the zero frequency is defined as the carrier-envelope offset frequency f_{CEO}, visualized in figure 2.3 (b). Thus, the absolute frequency of the mth comb line can be determined by

$$f_m = f_{\mathrm{CEO}} + m f_{\mathrm{rep}}. \tag{2.26}$$

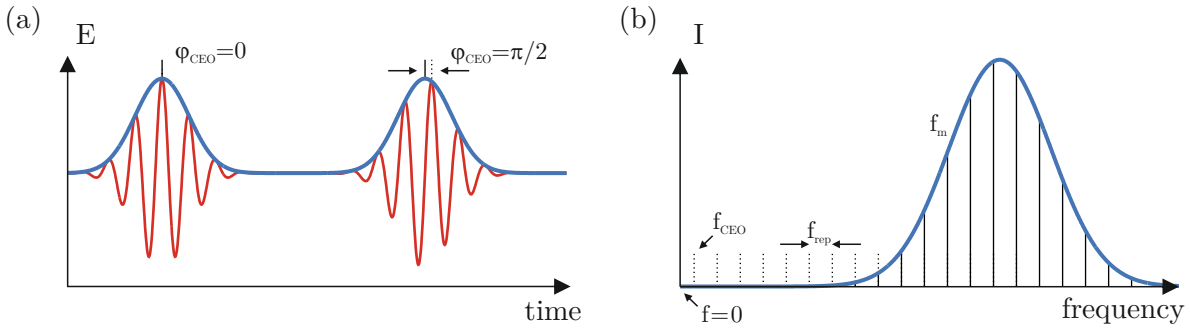

Figure 2.3.: Representation of the CEP in (a) the time domain and (b) the frequency domain.

In the case of a stabilized frequency comb with $f_{\mathrm{CEO}} = 0$, the CEP of every consecutive pulse is the same. The absolute value is usually not of interest, since the CEP changes as a result of GVD and thus oscillates during propagation anyway. It is then adjusted to the experiment through the insertion of a thin optical medium.

Detection of φ_{CEO} is accomplished via an interferometric f-to-$2f$ self-referencing scheme, in which the higher frequency end of the comb is beaten with the frequency-doubled lower-frequency end. This requires an octave spanning spectrum that usually has to be generated first by spectral broadening techniques such as WLG. A feedback loop to the pulse source then allows to lock the carrier-envelope offset to a specific value by adjusting the intracavity dispersion.

2.5. High Harmonic Generation

In contrast to the generation of low-order harmonics, which relies on the nonlinear polarization response of a medium, the generation of high harmonics can not be understood within this perturbative decription. The basis of HHG are extreme nonlinear processes that are likely to occur when the electrical field strength of the laser approaches the field strength binding the electron to the atom. The main features of this process are usually described by the semi-classical three-step model proposed by Corkum [18].

2.5.1. The Three-Step Model

Figure 2.4 illustrates the course of HHG according to the three-step model. If a linearly polarized strong laser field with an electric field strength on the order of the atomic field strength interacts with an atom, it distorts the atomic potential (step 1). Now that the potential barrier is lowered, there is a nonzero chance for tunnel ionization of the bound valence electron. If the electron is released into the continuum, it is at first accelerated by the laser field away from the ionic core until the electric field changes sign and the electron is driven back (step 2). When it reaches the ion again, there is a small chance of recombination at which the energy gained during acceleration in the laser field can be released in the form of a high energetic photon (step 3).

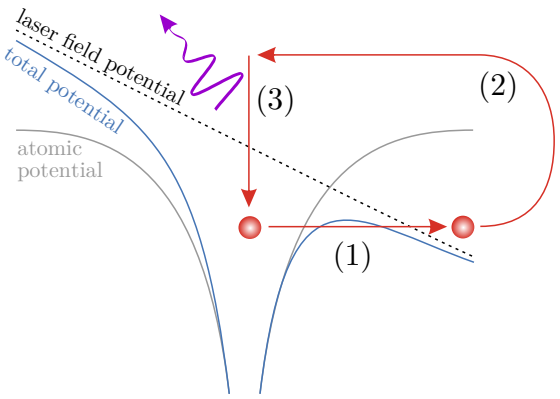

Figure 2.4.: The three-step model of high harmonic generation. The external laser field potential distorts the atomic potential and enables tunnel ionization of an electron (1). The electron is accelerated by the oscillating electric field and gains kinetic energy (2). Once the laser field changes sign, the electron is accelerated back to the ion and recombines under emission of a photon (3). Adapted from [111].

Depending on the momentum of the released electron, it returns to the ion either before or after the next zero crossing of the laser field. In the first case, it follows a *short trajectory* and in the latter case a *long trajectory*, named according to the excursion time of the electron in vacuum. For the short trajectories, the kinetic energy increases with the return time, which means that the emitted pulse is positively chirped. For the long trajectories, the energy decreases with time as a result of the inverted laser field, hence the pulse is negatively chirped. The maximum achievable photon energy at the so-called cut-off depends on the ionization potential of the atom I_p and the ponderomotive energy of the laser field $U_p = (e^2 E_0^2)/(4m\omega^2)$, where e is the electron charge, E_0 the electric field amplitude, m the electron mass and ω the angular frequency of the laser. The cut-off energy E_c is calculates according to

$$E_c = I_p + 3.2U_p. \tag{2.27}$$

Until the cut-off, all energies are generated with almost equal probability, resulting in a long plateau of peaks with similar amplitude, separated by twice the laser frequency. This is explained by the fact that an electron can tunnel out each time the electric field is close to a maximum, no matter if it is positive or negative (as long as the medium is isotropic, as for example a gas). Hence, the HHG process occurs at a frequency 2ω, and only odd harmonics are observed instead of a continous spectrum [111].

Following the three-step model, it becomes apparent that the direct generation of isolated

attosecond pulses from a few-cycle driving pulse is not possible. Instead, a train of attosecond pulses separated in time by half the laser field period is produced. To obtain an isolated attosecond pulse, the emission of high harmonics in a certain spectral range needs to be somehow restricted to a single half-cycle. In practice, this is accomplished by various gating techniques. In temporal gating techniques, such as polarization gating [93] and generalized double-optical gating [55], two or more laser fields are superimposed such as that only a single half-cycle contributes to the HHG process. In spectral selection techniques such as amplitude gating [33] or ionization gating [47], only the attosecond pulse originating from the most intense half-cycle, which produces the cut-off spectral components of highest energy, is selected.

3. Seed Source

To identify a suitable seed source for the OPCPA system with a central wavelength around 800 nm, the following considerations are made:

- The seed spectrum has to cover the whole spectral amplification bandwidth. For optical synchronization between the seed and the ytterbium (Yb)-based pump source, the spectrum additionally has to cover the wavelength around 1030 nm with enough energy for subsequent amplification.
- A higher seed pulse energy leads to gain quenching of parametric superfluorescence and is beneficial for the final temporal contrast.
- Low pulse-to-pulse fluctuations guarantee stable amplification conditions.
- The pulses must be free of higher order dispersion in order to compress them close to the Fourier-transform limit (FTL) using standard optics.
- A stable CEP is required.

Modern Ti:Sa-oscillators fulfill all the aforementioned criteria and are available as industrial products with high reliability. Based on the specified system parameters, the venteon dual CEP laser system (venteon Laser Technologies GmbH) is chosen as the seed source for the OPCPA system presented in this thesis.

3.1. venteon dual CEP

The venteon dual CEP is an octave spanning Ti:Sa-oscillator with integrated CEP stabilization and two outputs designated to seed an OPCPA and an Yb-based amplifier. The schematic setup of the system is depicted in figure 3.1.

Pumped by a continuous wave diode-pumped solid state laser (Laser Quantum Finesse) with up to 5.0 W at 532 nm, the oscillator delivers up to 200 mW output power at a repetition rate of 80 MHz, yielding pulse energies of 2.5 nJ per pulse. The spectral bandwidth exceeds 380 nm, measured at -10 dB, and supports a FTL pulse duration below 5 fs.

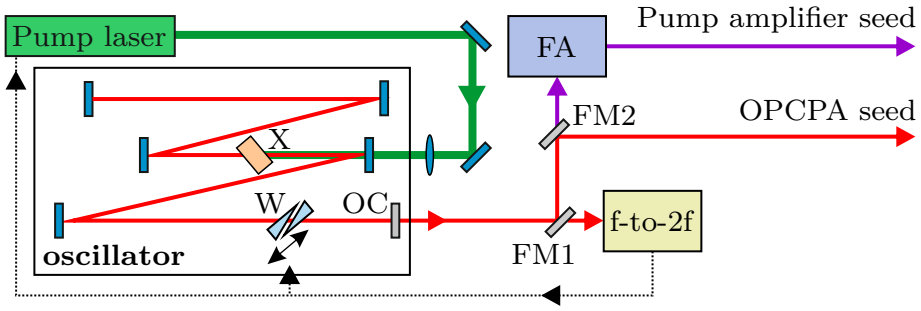

Figure 3.1.: Schematic layout of the venteon dual. X: Ti:Sa crystal, W: motorized wedges for dispersion control, OC: outcoupling mirror, FM1: dichroic filter mirror for f-to-2f signal generation, FM2: filter mirror for pump amplifier seed generation.

In order to measure and stabilize the CEP, the spectral wings of the spectrum around 570 nm and 1040 nm are filtered at the output by the dicroic filter mirror FM1 and beaten in an f-to-2f interferometer. The beat signal is detected by an avalanche photodiode in the frequency domain and locked to a quarter of the repetition rate (20 MHz). Hence every 4^{th} pulse carries the same CEP. An active feedback directly to the pump laser power compensates for fast phase drifts, whereas slow drifts are compensated by moving the intracavity wedges to alter the dispersion. This allows long-term CEP stabilization with a residual phase noise below 70 mrad, measured in a bandwidth between 3 Hz and 1 MHz, as shown in figure 3.2.

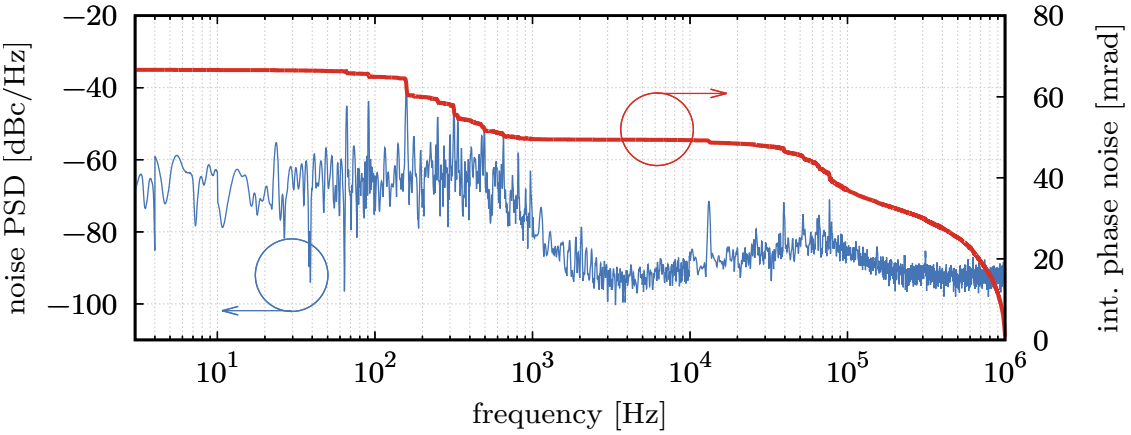

Figure 3.2.: CEP noise analysis of the seed source. The power spectral density of the stabilized CEP (blue) is shown together with the integrated phase noise (red). Data provided by venteon Laser Technologies GmbH.

After signal derivation for the f-to-2f interferometer, the spectral components around 1030 nm with a full-width-at-half-maximum (FWHM) of ∼20 nm are transmitted at the filter mirror FM2, prefiltered by an interference filter and coupled into a fiber amplifier (venteon pre-amp, venteon Laser Technologies GmbH) in order to generate the seed for the pump regenerative amplifier. The fiber amplifier boosts the energy from about 30 pJ to the nJ-level. A detailed description of the fiber amplifier setup is given in chapter 4.

The derivation of pump and seed pulses directly from the Ti:Sa-oscillator ensures that

temporal drifts of the front end equally affect pump and seed pulses of the OPCPA, leading to all-optical synchronization [42].

Figure 3.3 (a) shows the broadband output spectrum of the oscillator after filtering as it is used to seed the OPCPA. The dip around 1030 nm originates from the derivation of the pump amplifier seed. A compressed output pulse duration of 6.0 fs, measured with SPIDER (venteon Laser Technologies GmbH) and presented in figure 3.3 (b), proves the compressibility of the seed source close to the FTL.

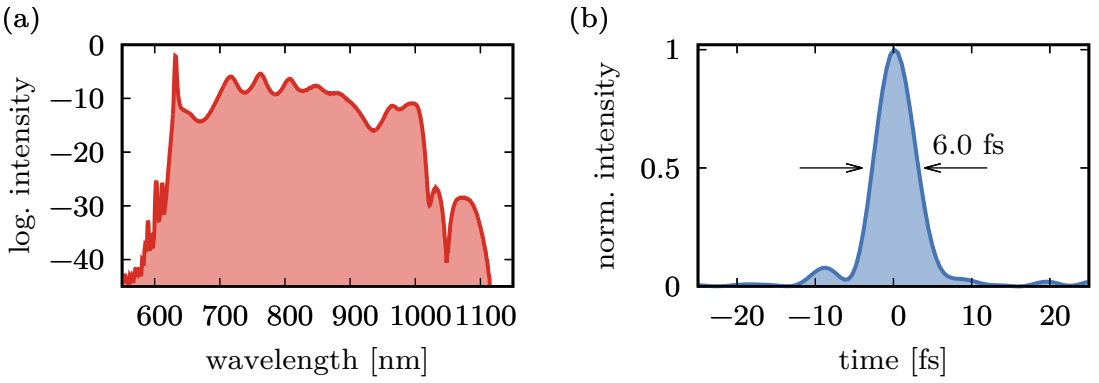

Figure 3.3.: (a) Output spectrum of the seed source, measured with Ando AQ 6315B and (b) compressed output pulse, measured with SPIDER. Data provided by venteon Laser Technologies GmbH.

4. Thin-Disk Regenerative Amplifier

This chapter presents design, implementation and characterization of the thin-disk-based regenerative amplifier that has been developed to pump the OPCPA system. Seeded by the Ti:Sa-oscillator introduced in chapter 3, it is designated to amplify picosecond-pulses to the multi-mJ level with near-diffraction limited beam quality and low pulse-to-pulse fluctuation. A repetition rate of 6 kHz has been chosen to achieve both, high pulse energies and high average power.

4.1. Short-Pulsed Picosecond Pumping

Pumping OPCPAs with ultrashort pulses in the ps-range provides a series of advantages:

- *Reduced stretcher and compressor complexity*
  Efficient energy conversion requires stretching of the seed pulses to a significant fraction of the pump pulses [61]. Extensive stretching to several tens of picoseconds requires highly dispersive elements such as prisms or gratings, and subsequently demands for a sophisticated dispersion management to achieve proper recompression [103]. With shorter pump pulses, utilization of chirped mirrors in combination with bulk material becomes possible, greatly simplifying dispersion management and additionally enhancing the signal compression efficiency.

- *Enhanced temporal pulse contrast*
  Due to optical parametric generation, a PSF background is generated in the time window of the pump pulse duration [104]. Especially when the output is focused to high intensities, a long preceeding pedestal can alter the physical properties of the target before it is reached by the main pulse [4]. Short pump pulses reduce the extent of the PSF-background, thus providing a higher pulse contrast on a picosecond timescale. In addition, the amplification of parasitic pre- or postpulses is prevented.

- *Increased amplification bandwidth*
  For pulses with $\tau < 20\,\mathrm{ps}$, the damage threshold of nonlinear crystals no longer scales

with $\tau^{1/2}$, but at a significantly lower rate [97]. Thus, OPCPAs can be pumped at higher intensities to achieve a higher parametric gain. Consequently, shorter nonlinear crystals can be employed which support a larger amplification bandwidth thanks to the relaxed phase matching conditions [16, 112].

At shorter pulse durations in the femtosecond regime, the temporal walk-off between pump and signal limits the conversion efficiency of the OPCPA process [16,36,84]. A pump pulse duration around 1 ps is therefore considered to be the optimum in the context of OPCPA.

A fundamental limitation to this approach is given by the onset of nonlinear effects, in particular Kerr lensing, in the propagation medium. This is evaluated in detail in section 6.3.

4.2. Yb-based Thin-Disk Laser Head

In recent years, Ytterbium-doped crystals such as Yb:YAG have become popular laser gain media for the cost-efficient generation and amplification of ps-pulses. A broad absorption and emission bandwidth, combined with a long fluorescence lifetime in the ms-range [48], allows for efficient direct diode pumping and high energy storage. Pumping directly into the zero-phonon line at 969 nm using wavelength-locked diodes [115] results in a low quantum defect of only ∼3 % and prevents excessive fractional heating. A higher laser efficiency can therefore be attained as compared to conventional pumping at 940 nm thanks to reduced diffraction losses from thermally-induced phase distortions [118]. High thermal conductivity of the gain medium enables effective cooling and permits operation at high power with near-diffraction limited beam quality [26]. Emission takes place around a central wavelength of 1030 nm in a bandwidth of ∼9 nm, supporting pulse durations of a few hundred femtoseconds [67].

Those features are perfectly combined in the thin-disk laser concept, which has been first demonstrated in 1993 by Giesen et al [30]. The basic concept of the disk-laser head is depicted in figure 4.1.

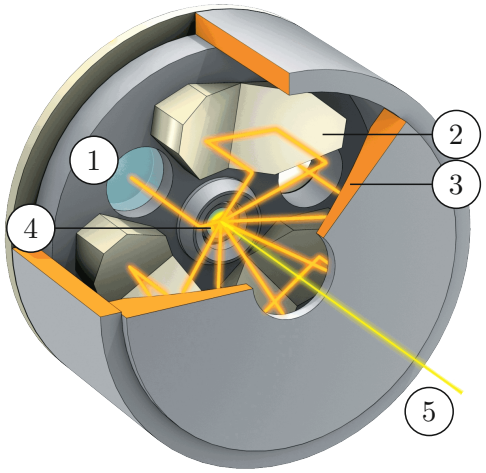

Figure 4.1.: Basic concept of the disk-laser head. (1) Collimated pump light incoupling, (2) retro-reflecting mirror pair, (3) parabolic mirror, (4) thin disk, mounted on a heat sink, (5) amplified laser beam. Reproduced from [57].

At the heart of the laser head is the Yb-doped disk, which is typically 100 µm to 300 µm thick, with a diameter of a few millimeters. It is attached to a cooling substrate made of copper or diamond, which is directly water-cooled from the backside and provides a homogeneous heat transfer in the axial direction of the crystal. The front side is usually anti-reflection (AR)-coated for the pump- and signal wavelength, while the backside exhibits a highly reflective (HR)-coating. The disk can therefore be used as an active mirror in the amplifier cavity.
Because the gain medium is a quasi-three-level system, high pump power densities of more than 1.5 kW/cm^2 are required to achieve population inversion at room temperature and >10 kW/cm^2 for efficient operation [30]. The usually low absorption of the disk can be compensated by a multipass configuration of the pump light over the active medium. After traversing the collimating optics, a parabolic mirror images the pump beam on the disk, where it is partly absorbed. The remaining fraction is reflected, recollimated and redirected by a pair of retro-reflecting mirrors to another part of the parabolic mirror, refocusing it again on the disk. This process is repeated until the majority of the pump light is absorbed.

The advantages of the thin-disk laser concept are manifold. Efficient, longitudinal heat removal creates the possibility to utilize high pump densities while keeping thermally induced distortions, e.g. thermal lensing and thermally induced birefringence, at a minimum. This enables a near diffraction limited beam quality, even in multi-pass arrangements. Scalability towards higher average powers and energies can be realized by simply increasing the disk diameter and using a larger pump spot. Thanks to the small longitudinal extension of the crystal, even short pulses with high peak power can be amplified without significant accumulation of nonlinearities, which eliminates the need for expensive large-area gratings in a CPA concept. The major disadvantage, a small single-pass gain, can be easily compensated by multiple passes through the crystal.

The herein developed regenerative amplifier is based on a thin-disk laser head of the TruMicro 5000 series by TRUMPF Laser GmbH + Co. KG, shown in figure 4.2.

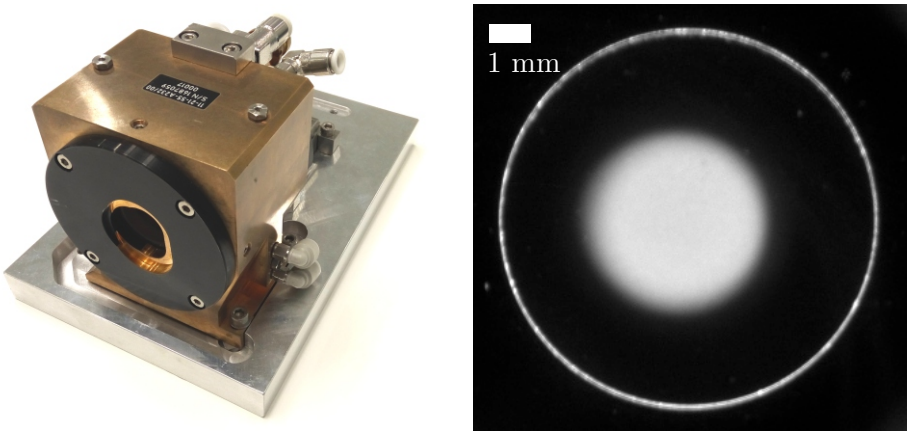

Figure 4.2.: Left: Thin-disk laser head of the TruMicro 5000 series, by TRUMPF Laser GmbH + Co. KG. Right: pump spot (center) on the disk (outer circle).

The pump light from the laser diodes is fiber coupled to the laser head, making it possible to place the diodes at a remote location and saving space in the disk-head setup. Up to 400 W of pump power are supplied at a wavelength of 969 nm through a fiber with a core diameter of 0.6 mm. After a three-lens collimation optic, a pump spot size of ∼4.2 mm is obtained (figure 4.2 (b)). The laser head is arranged for a total of 18 passes over the gain medium, resulting in almost complete pump-light absorption. A ∼1/10 mm-thin Yb-doped disk with a diameter of 9 mm and a nominal radius of curvature (ROC) of 2 m is directly soldered to a diamond heat sink which is water-cooled from the backside for efficient heat removal. To avoid an etalon effect, the disk is slightly wedged.

4.3. Regenerative Amplifier

At present, the generation of ultrashort pulses with high peak powers directly by mode-locked oscillators is limited to the µJ-level, caused by emerging nonlinearities which lead to a destabilization of mode-locked operation [69, 79]. At a pulse duration around 1 ps, a maximum pulse energy of 80 µJ has been demonstrated so far from a thin-disk oscillator operated in vacuum [86].
In order to further increase peak power and pulse energies, amplifier systems are necessary. Regenerative amplifiers are commonly used to amplify ultrashort low-energy pulses from an oscillator up to the multi-mJ level. Figure 4.3 demonstrates the basic concept at the example of two possible resonator geometries, the linear (a) and the ring (b) resonator. In both cases, an individual pulse is selected by an optical switch, e.g. a Pockels cell (PC) and a waveplate in combination with a thin-film polarizer (TFP), and trapped inside the resonator cavity, where it repeatedly passes an active gain medium. Once the desired gain is achieved, the amplified pulse is ejected again by the optical switch. The switching rate of the PC determines the frequency of the amplified pulse train.

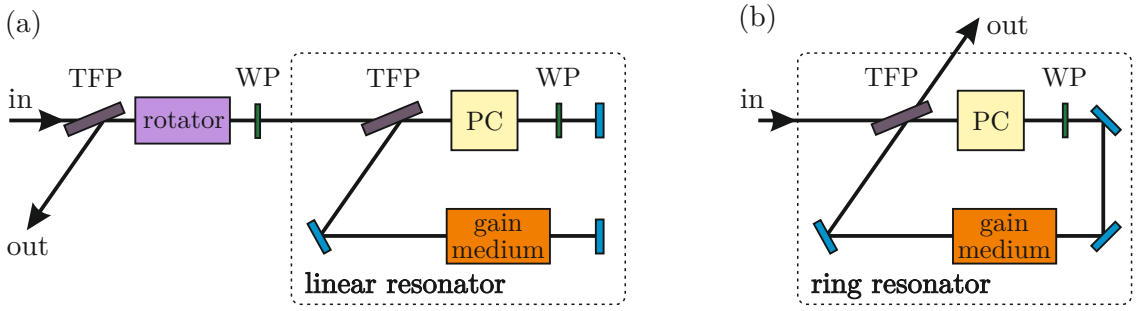

Figure 4.3.: Basic concept of a regenerative amplifier with (a) a linear resonator and (b) a ring resonator. TFP: thin-film polarizer, WP: waveplate, PC: Pockels cell.

In a linear resonator, the pulse passes gain medium and PC twice per roundtrip, leading to an enhanced gain.Because the output beam propagates towards the input, it has to be separated via a Faraday rotator, a quarter-waveplate and an additional TFP. The availability of rotators with a large aperture which are able to withstand high powers and the associated thermal lensing effects are current limitations of this resonator geometry. No such restrictions exist in case of a ring resonator, where the output is physically separated

from the input, saving the additional costs of the rotator and avoiding nonlinearities introduced by the rotator material. The drawback of this geometry is the lack of the natural double pass through gain medium and PC. The PC therefore has to rotate the polarization twice as much and the roundtrip gain is halved.

Apart from the resonator geometry, the following aspects have to be taken into consideration in the design process of a regenerative amplifier:

- *Gain narrowing*
  High gain and the limited bandwidth of the gain medium may result in gain narrowing, increasing the intital pulse length due to a reduction of the spectral bandwidth [74].
- *Cavity losses and etalon effect*
  The efficiency and the overall gain of the amplifier is limited by cavity losses, which hence should be minimized. Reflections from parallel surfaces of transmissive elements need to be avoided, as they may lead to an etalon effect, resulting in amplitude modulations, pulse break-up or gain narrowing [20, 63].
- *Dispersion and nonlinear phase accumulation*
  Transmissive intracavity elements, such as PC, waveplates or the gain medium, introduce dispersion which has to be accounted for to achieve a FTL pulse duration. At increasing peak powers, nonlinear effects can lead to pulse distortions caused by SPM or even optical damages, caused by Kerr lensing [14]. CPA [96] and an intelligent cavity design can minimize the accumulated nonlinearities.
- *Pulse amplification dynamics*
  At repetition rates close to the inverse fluorescence lifetime of the gain medium, special amplification dynamics occur, leading e.g. to period doubling or deterministic chaos in the amplified pulse train [23,58]. This behavior depends on the small signal gain, the seed energy and the ejection frequency of the amplifier and requires careful parameter design to acquire a stable amplified pulse train.

Keeping those aspects in mind, a regenerative amplifier cavity has been designed, presented in the following.

4.4. Cavity Design and CPA

The cavity design is subject to some boundary conditions, given by the physical properties of the utilized optical elements and general applicable rules. The first constraint is the pump spot size, which defines the beam diameter on the disk. An appropriate beam diameter is around 80 % of the pump spot. This constitutes a good overlap for effcient energy extraction while avoiding the outer pumped area, where beam distortions might occur due to the phase step between the pumped and unpumped area [12,31]. Secondly, in the PC, a collimated beam with a large beam diameter is desired to ensure clean switching and smallest nonlinearities. The ROC of the disk has to be considered and in general, a sufficiently large spot size on all optics is necessary to avoid optical damages. At the same

time, the cavity length should be as short as possible in order to increase the mechanical stability.

Figure 4.4 outlines the cavity scheme, designed on the basis of the previous considerations. A ring resonator has been chosen to avoid the additional rotator and to create a clear separation between the in- and output. To compensate for the lower gain, the disk is passed twice per roundtrip inside the cavity via $2f$-imaging. The main elements are integrated in the plot at their respective positions in the layout. Table 4.1 lists the corresponding distances and components.

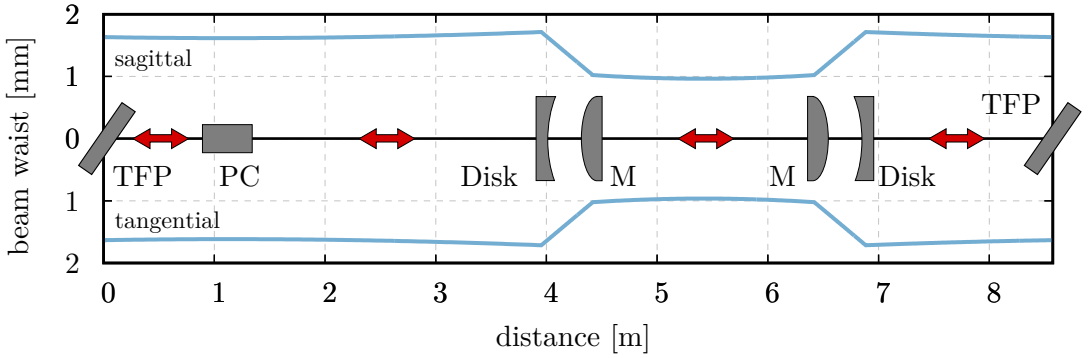

Figure 4.4.: Ring cavity design of the regenerative amplifier. TFP: Thin-film polarizer, PC: Pockels cell, M: plane-convex mirror.

Table 4.1.: Distances and optical elements used in the regenerative amplifier cavity. The thermal lens of the disk is already accounted for in the ROC.

cavity element	ROC / distance [mm]
TFP	∞
distance	1000
PC	∞
distance	2950
disk, 1st pass	2190
distance	465
mirror	-1500
distance	2000
mirror	-1500
distance	465
disk, 2nd pass	2190
distance	1700
TFP	∞

At the in- and outcoupling TFP, the designated $1/e^2$-beam diameter of the resonator mode is 3.2 mm. After 1 m propagation, at the position of the beam waist, the PC is placed. The thin-disk is passed for the first time after additional ∼3 m and focuses the beam according to its ROC. The ROC of the disk is influenced by the thermal lens towards longer focal lengths, which can be accounted for by either equally adjusting the distance between the disk and the subsequent convex mirrors or the intermediate distance between the latter ones. Experimentally, the focal length of the thermal lens at full pump power

in laser operation was estimated to be $f_{tl} \approx -11.5\,\mathrm{m}$, altering the effective ROC of the disk to 2190 mm. This is already accounted for in the cavity design. At the disk-position, a beam diameter of 3.64 mm is expected, resembling ∼78 % of the pump spot diameter and thus supporting only TEM_{00}-mode operation. The beam is recollimated by a second convex mirror and reaches its minimum diameter of 1.9 mm at half the distance before it is expanded by a second convex mirror. The second pass on the disk recollimates the beam and it is sent back to the initial TFP, where it starts another roundtrip or is ejected from the cavity.

At the given pump power of 400 W, around 180 W average output power from the regenerative amplifier is expected, corresponding to 30 mJ at the designated repetition rate of 6 kHz. Assuming a Gaussian shaped pulse with 1 ps pulse duration results in peak intensities of >28 GW, which will inevitably lead to strong nonlinearities during amplification. Therefore, a CPA concept has to be integrated in the amplifier design.
The accumulated nonlinearities are described by the B-Integral as defined in section 2.3.2. In general, values of $B \leq 3$ are accepted in the design of high power amplifiers and usually mark a regime without serious nonlinearities. However, noticeable spectral distortions may set in already at $B \leq 1$. The amplified pulses have thus to be carefully characterized in order to exclude detrimental influence of SPM or Kerr lensing.
Figure 4.5 presents the estimated B-integral for a total of 130 roundtrips in the designed cavity, using a chirped pulse with $\tau = 600\,\mathrm{ps}$. A constant roundtrip gain is assumed in the

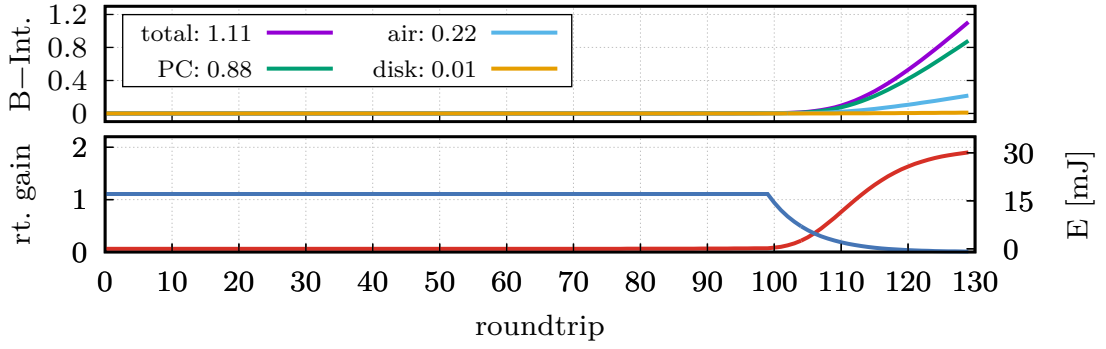

Figure 4.5.: B-Integral calculated for amplification of a chirped pulse with a pulse duration of 600 ps to 30 mJ, in the cavity of figure 4.4. Details are given in the text.

first 100 roundtrips, while afterwards the gain is reduced by 15 % in every pass to account for gain saturation, reproducing the typical energy build-up in a regenerative amplifier. Those parameters are chosen in order to amplify a seed energy of 7 nJ to 30 mJ within 130 roundtrips. A PC of 40 mm length is assumed, with BBO as the electro-optic material. A moderate total B-Integral of 1.11 is estimated for the amplification process of the stretched pulse. The majority is accumulated in the PC, while the nonlinearities stemming from the gain medium are negligible. Propagation in air constitutes already 20 % of the accumulated nonlinearities. Without CPA and $\tau = 1\,\mathrm{ps}$, the same calculation results in a B-Integral > 600, rendering a CPA-free approach doomed to fail.

4.5. Experimental Setup

A schematic overview of the herein realized regenerative amplifier setup is given in figure 4.6 and will be explained in the following.

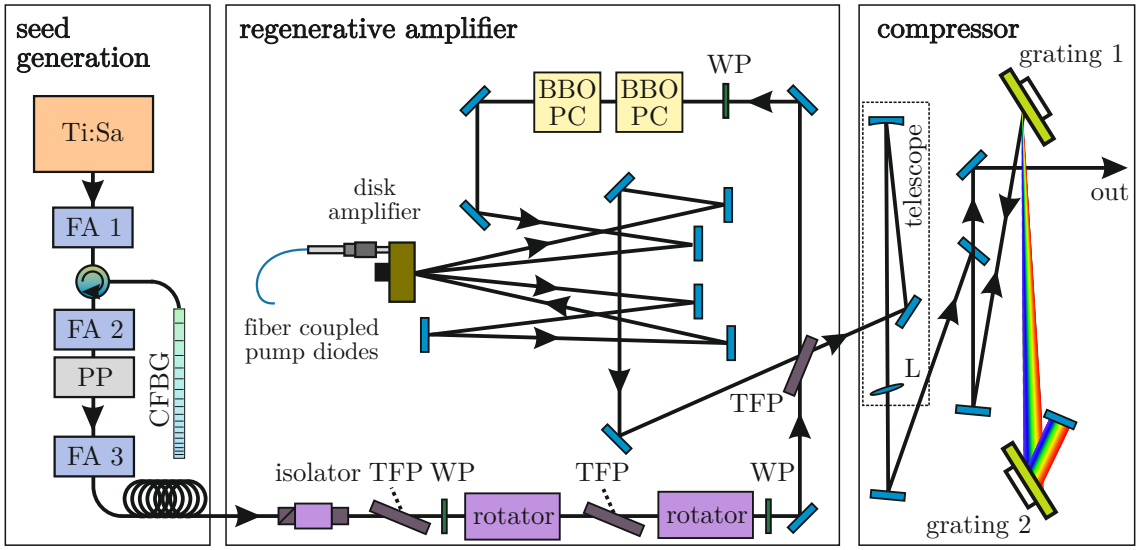

Figure 4.6.: Schematic layout of the regenerative amplifier. Ti:Sa: Titanium-sappphire oscillator, FA: fiber amplifier, CFBG: chirped fiber Bragg grating, PP: pulse-picker, TFP: thin-film polarizer, WP: waveplate, BBO PC: BBO Pockels cell, L: telescope lens.

The seed pulses are derived directly from the Ti:Sa-oscillator, described in chapter 3. Because only ∼40 pJ are available at the filtered oscillator output, a three-stage fiber-amplification chain (venteon pre-amp, venteon Laser Technologies GmbH) is implemented to increase the available seed pulse energy. After the first fiber amplifier (FA), where the pulses are amplified to ∼560 pJ, a chirped fiber Bragg grating (CFBG) (TeraXion, Inc.) is placed in conjunction with a circulator to stretch the seed with a dispersion of −384 ps/nm. Around the central wavelength of 1030 nm, a −3 dB-bandwidth of ∼5 nm is supported. A CFBG is a convenient, space-saving and alignment-free alternative to a large grating stretcher, as long as the dispersion can be exactly matched to the designated compressor. The stretched pulse can now be further amplified in the second FA to >4 nJ without introducing significant nonlinearities. FA 2 is followed by a pulse-picker, where the repetition rate of 80 MHz, given by the oscillator, is reduced to 1 MHz by means of an acousto-optic modulator. Finally, the third FA delivers a pulse energy up to 100 nJ, theoretically available to seed the regenerative amplifier. However, amplification in FA 3 is limited to 25 nJ by the onset of SPM, which diminishes the pulse contrast and transfers energy into the spectral wings. This is investigated in detail in section 4.8. The seed spectrum after the FA-chain is shown in figure 4.7 (a).

Before the seed enters the amplifier cavity, it passes an optical isolation chain to prevent back-reflections from the amplifier to the front-end. A fiber isolator, a bulk isolator and two high-power Faraday rotators (Electro-Optics Technology, Inc.) in combination with TFPs and quarter-waveplates, arranged according to figure 4.6, provide a total isolation

of >100 dB in reverse direction. Although such a high attenuation is not required for a ring cavity, it is implemented in this system to allow for a fast rearrangement of the setup towards a linear cavity. By the time the seed pulses enter the cavity, the pulse energy is reduced by >70 % to 7 nJ, caused by coupling losses of the fiber components after FA 3 and transmission losses in the isolation chain.
The cavity is set up as a ring, with the TFP marking its beginning and end. A pulse is selected by two PC, each containing a z-cut 20 mm-short BBO-crystal with an aperture of 12 mm and a transversely applied electric field. Both PC are connected in parallel to a high-voltage switch (Bergmann Messgeräte Entwicklung KG). The advantage of using two PC instead of a single one with a 40 mm-crystal is the reduced quarter-wave voltage, being 16 kV in this configuration. If no amplification is desired, a polarization change of $\lambda/2$ is introduced in every roundtrip and the pulse is ejected from the cavity after the second roundtrip. To start the amplification process, the PC voltage is switched and the polarization is maintained, trapping the currently s-polarized pulse in the cavity. Here it passes the disk twice in every roundtrip, until after 138 roundtrips, the target energy is achieved. Switching back the PC voltage rotates the polarization again and ejects the amplified pulse at the TFP. A pulse energy of 30.5 mJ is measured right after the amplifier, corresponding to 183.5 W of average output power and an optical efficiency >46 %. Gain narrowing reduces the FWHM of the amplified spectrum to 1.22 nm, as shown in figure 4.7 (b), supporting a FTL pulse duration of 1.04 ps. The spectral shape remains unchanged towards higher pulse energies without the occurrence of SPM-induced artifacts, which approves the adequacy of the implemented CPA-setup.

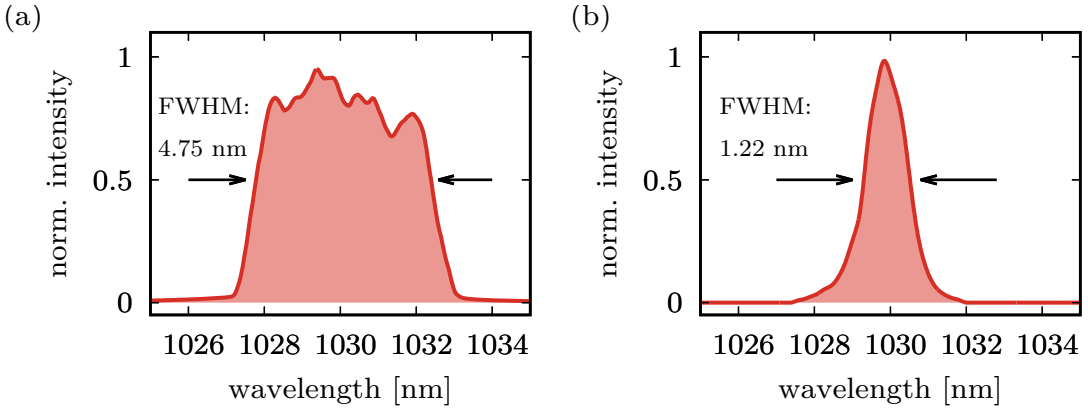

Figure 4.7.: (a) Seed spectrum of the regenerative amplifier after stretching, pulse-picking and amplification to $E = 25$ nJ in the FA-chain and (b) amplified spectrum, which is identical before and after compression.

After exiting the cavity, a telescope magnifies the beam by a factor of 2.6 to avoid nonlinearities in the subsequent pulse compression. A grating compressor in double-pass near-Littrow configuration is used under an incident angle of 62° to introduce a GDD of 2.1×10^8 fs^2, compensating the dispersion of the CFBG up to the 4$^{\text{th}}$ order. Both gratings (Plymouth Grating Laboratory, Inc.) have a line density of 1760 lines/mm and are optimized for reflection into the -1^{st} order. A normal separation of ∼900 mm results in the shortest pulse duration. In- and outcoming beam are separated by a slight vertical offset,

introduced by the folding mirror after grating 2. The final pulse duration is characterized with a second-order intensity autocorrelator (pulseCheck, APE GmbH). The measurement is presented in figure 4.8 (b). The spectrum after compression remains unchanged as compared to figure 4.7 (b) and reveals a form factor of $\Delta t_{AC}/\Delta t = 1.45$. Applied to the autocorrelation trace, a compressed pulse duration of 1.31 ps is acquired, which is close to the FTL of 1.04 ps, plotted as comparison in red. Only minor satellite pulses with low intensity are visible, testifying a well matched dispersion between stretcher and compressor. The final amplification characteristics after compression are presented in figure 4.8 (b). At the output of the regenerative amplifier, up to 173.8 W of compressed power and pulse energies of 28.9 mJ are available, corresponding to a compression efficiency of >94 %. A peak power >23 GW is reached. The overall optical efficiency is as high as 44.6 %, while the slope efficiency amounts to 60 %, obtained from the indicated linear fit of all values recorded above a pump power of 150 W.

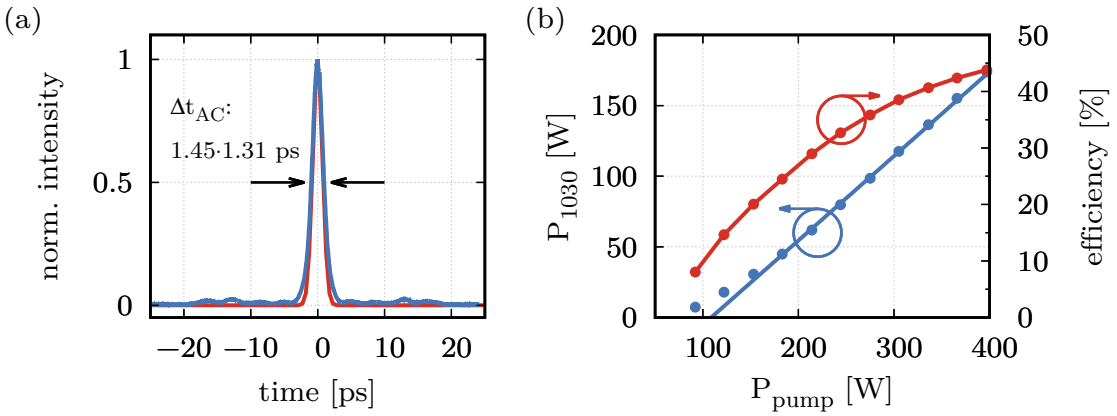

Figure 4.8.: (a) Autocorrelation trace of the compressed pulse. The autocorrelation trace of the transform-limited pulse is indicated in red as comparison. (b) Amplification characteristics after compression.

In the following sections, characterization and, if applicable, optimization of relevant system parameters for pumping an OPCPA is presented.

4.6. Pulse Amplification Dynamics

As mentioned at the beginning of this chapter, amplification at repetition rates close to the fluorescence lifetime of the gain medium exhibits special amplification dynamics. The reason behind is that under these circumstances, the gain of a specific pulse is strongly coupled to the amplification of the previous pulse. Assuming a pulse depletes the gain medium completely and the next pulse enters the cavity before the population inversion has fully recovered, the gain is less. If the third pulse now arrives at a time where the inversion is at its maximum again, it is amplified just as the first pulse. A stable regime results in which every second pulse is amplified, known as the *period doubling* or *bifurcation* regime. Its stability depends on the amplifier gain and the gain depletion, given by the pump power, the seed-pulse energy und the number of roundtrips. Different dynamics eventually lead to period tripling or chaotic amplification.

The amplification dynamics of the regenerative amplifier are characterized by the bifurcation diagram in figure 4.9. At every indicated pump power, the amplitude of 5000 consecutive pulses is measured with a GHz-oscilloscope (LeCroy waverunner 640zi) and a photodiode (Hamamatsu G8370-01). The PC is switched at 12 kHz repetition rate and the pulses are ejected after 138 roundtrips.

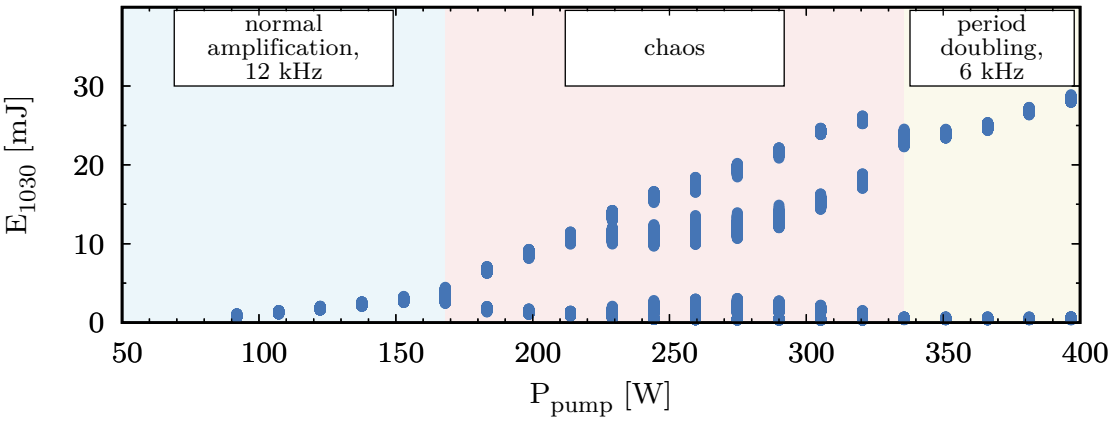

Figure 4.9.: Bifurcation diagram of the regenerative amplifier at a PC repetition rate of 12 kHz and 138 cavity roundtrips. Three amplification regimes are identified in dependence of the pump power.

Three regimes can be identified:

1. *Normal amplification*
   Up to a pump power of 170 W, every pulse is amplified at the fundamental repetition rate.

2. *Chaos*
   Above 170 W, interdependence between the pulses becomes visible and chaotic amplification to random pulse energies takes place. This regime is generally undesired.

3. *Period doubling*
   Pumping with more than 340 W results in period doubling, amplifying every second pulse at an effective repetition rate of 6 kHz. The intermediate pulses are suppressed to <1.5 % of the main pulse energy of 28.9 mJ.

At the maximum output power, the pulse-energy fluctuation has been measured over 100 000 consecutive pulses, using the same setup as before. A standard deviation below 0.65 % qualifies this parameter configuration as an excellent setpoint.

4.7. Beam Quality

The beam quality of a laser is commonly characterized by the M^2-factor, which is defined according to ISO standard 11146 [75] as

$$M^2 = \frac{\lambda}{\theta \pi w_0}, \tag{4.1}$$

where w_0 is the beam radius at the beam waist, λ the wavelength and θ the half-angle beam divergence. A diffraction-limited Gaussian beam has an M^2 factor of 1.
A home-build M^2-measurement setup, based on a camera (scA1300-32fm, Basler AG) and a motorized translation stage (RS3, Misumi GmbH) stage, is utilized to characterize the beam quality. The beam radius along the major and minor axis is evaluated at discrete positions and a second-order polynomial least-squares fit is applied, according to the description of the waist evolution $w(z)$ of a Gaussian beam during propagation along z,

$$w(z) = w_0 \sqrt{1 + \left(\frac{z - z_0}{z_R}\right)^2}, \tag{4.2}$$

$$z_R = M^2 \frac{\pi w_0^2}{\lambda}, \tag{4.3}$$

using the Rayleigh length z_R. Based on the fit parameters, the M^2 factor, the beam waist radius w_0 and the waist position z_0 are derived [39]. The data is evaluated according to ISO standard 11146 [75].

Figure 4.10 shows the measured caustic of the regenerative amplifier and selected beam profiles at different z-positions. Although a high beam quality in terms of M^2 is obtained, the beam exhibits a different beam waist radius in both axis. With $w_{0,x} > w_{0,y}$ and $M_x^2 < M_y^2$, the ellipticity of the beam increases with propagation and increasing beam size. In addition, a slight astigmatism is visible. Both effects are a result of the intracavity spherical optics, used under a deflection angle $\neq 0°$, which introduces a different effective focal length in each axis.

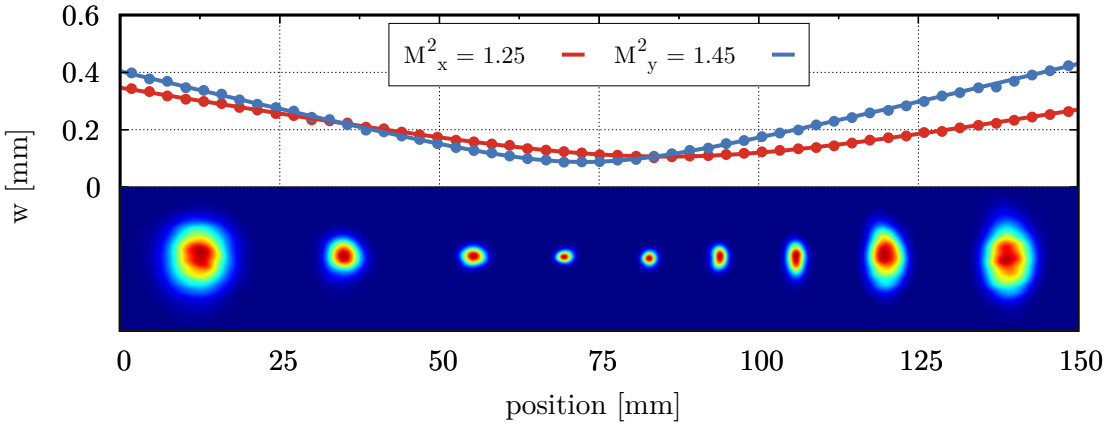

Figure 4.10.: M^2 measurement of the regenerative amplifier and selected beam profiles, identifying different w_0 in both axis and a slight astigmatism.

In order to reduce the ellipticity of the beam at the system output, a tilted collimation lens with a nominal focal length of $f = 1000\,\text{mm}$ is used in the telescope before the compressor (see figure 4.6). Tilting a thin lens by an angle ϕ around the x-axis results in a change of the effective focal length f' according to $f'_T = f \cos\phi$ in the transversal plane and $f'_S = f/\cos\phi$ in the sagittal plane [39]. However, since the beam has a different M^2 in both axis, a round beam in all z-positions can not be obtained. The aim is therefore

to match the horizontal and vertical waist radii to achieve a low ellipticity over a long propagation length. This is accomplished by an angular lens tilt of $\phi = 7°$, producing a less elliptic beam after the focal plane at the cost of an increased astigmatism. Because a round beam is preferred in the OPCPA to match the seed beam profile and achieve homogeneous and efficient amplification, this trade-off is accepted. The resulting optimized beam caustic is presented in figure 4.11.

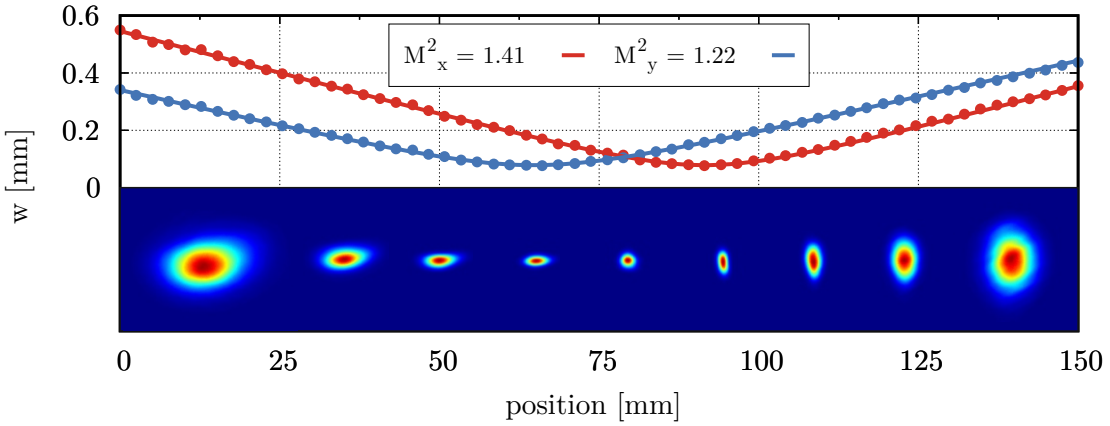

Figure 4.11.: M^2 measurement of the regenerative amplifier and selected beam profiles after optimization with a tilted lens, resulting in a less elliptic beam after the focal plane and equal beam waist radii.

After optimization, M^2 values of 1.41 and 1.22 are measured in the horizontal and vertical axis respectively, testifying a superb beam quality. At the output of the regenerative amplifier, an ellipticity of 0.9 is measured, with a major and minor beam diameter of 10.5 mm and 8.5 mm, respectively, which is shown in figure 4.12. In addition to the beam profile, the smoothed cross-sections through the centroid are imprinted. The small modulations along the horizontal axis are caused by irregularities in the compression gratings period and will be eliminated in the future by employing gratings with better quality. Occasional fringes and spots are visible due to particles on the utilized filters or the camera chip itself and are not part of the beam.

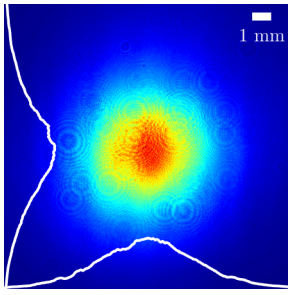

Figure 4.12.: Beam profile at the regenerative amplifier output. The smoothed cross-sections throughout the centroid are imprinted in white.

4.8. Temporal Pulse Contrast

Another important parameter of a pulsed high power laser is the temporal pulse contrast, defined as the ratio of the main-pulse peak intensity to the strongest pre- or post-pulse. A high pulse contrast is desirable because all energy contained in the side pulses or in a

pulse pedestal is not available in the main pulse and thus, lost. In a regenerative amplifier with CPA, two mechanisms determine the pulse contrast on different timescales:

- *Cavity leakage*
  If the polarization of the cavity beam is not strictly linear, a fraction of the beam leaks out of the cavity every time the outcoupling TFP is passed, generating a pre-pulse train in the form of the pulse build-up. On the other hand, if the polarization is not perfectly rotated in the final roundtrip, a fraction of the outcoupled beam remains in the cavity, leaving it only after another roundtrip and thus generating one or more post-pulses. All pulses are separated by the roundtrip time, in this case being ∼30 ns. Cavity leakage can be minimized by a proper alignment of the optical switch, i.e. PC and waveplate, but never be avoided completely due to the residual transmission of the TFP on the order of <0.1 %.

- *Residual dispersion*
  A higher order dispersion mismatch between pulse-stretcher and compressor results in a distorted temporal pulse shape, exhibiting e.g. a temporal pedestal and satellite pulses in a narrow timeframe around the main pulse. Nonlinear effects such as SPM may increase the residual dispersion and thus decrease the pulse contrast, even if stretcher and compressor are perfectly matched.

Cavity leakage in this system is minimized by iteratively adjusting the waveplate rotation, PC voltage and crystal angle while the pulse contrast is measured with a photodiode. Figure 4.13 shows the oscilloscope trace of the zoomed-in time segment around the main pulse, revealing a pre-pulse train and two post-pulses. At the optimum, the post-pulse contrast is < 1.65 % and the pre-pulse contrast < 0.06 %, limited by the TFP extinction ratio. Minimizing the pre-pulses simultaneously reduces the cavity roundtrip losses and is therefore prioritized. As comparison, the red trace in figure 4.13 visualizes the decrease in pulse contrast induced by a PC voltage change of only 5 %, which leads to a more than tenfold increase of the pre-pulse energy.

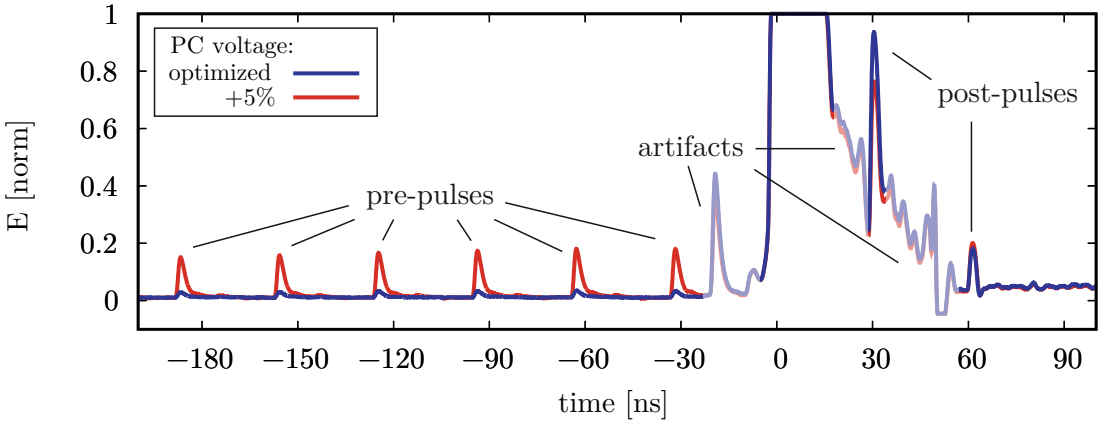

Figure 4.13.: Cavity leakage around the main pulse with optimized PC settings and at a 5 % reduced voltage. Artifacts are induced to the measurement by the PC voltage transition and are paled out for clarification.

The next optimization step is the identification and suppression of residual dispersion effects. As mentioned in section 4.5, the FA-chain is able to deliver seed pulse energies up to 100 nJ. This configuration has been used in the beginning to reach the stable period doubling regime already at lower pump powers and less roundtrips. However, a SHG-efficiency not exceeding 53 % indicated room for improvement. Excluding spectral and spatial distortions as well as cavity leakage, the obvious remaining factor was a temporal pulse contrast degradation due to residual dispersion. The pulse contrast around the main pulse can be measured most easily with an autocorrelator, as already presented in figure 4.8 (a). The utilized second-order autocorrelator however is limited in contrast to $\sim 10^{-2}$ and is thus not suitable to characterize e.g. a broad pulse pedestal. Out of this reason, a home-build third-harmonic-generation autocorrelator (THG-AC) was employed, allowing for a measurement contrast up to $\sim 10^{-4}$. The device is described in detail in appendix B. Different pre-amplification configurations have been tested, boosted by the regenerative amplifier to a few 100 µJ to provide enough energy for the THG-AC. The results are presented in figure 4.14.

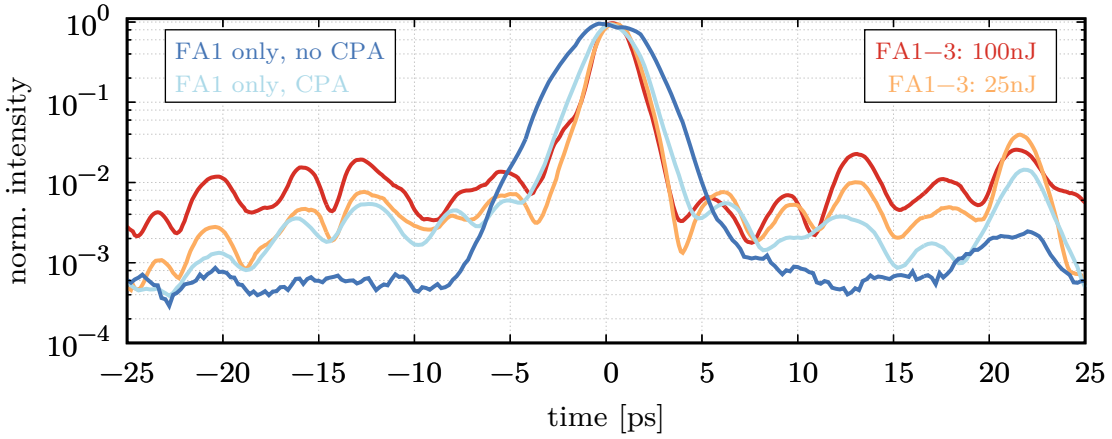

Figure 4.14.: THG-AC of the regenerative amplifier at low pump power, utilizing different pre-amplification configurations.

At the full FA-output of 100 nJ, a broad temporal pedestal at a normalized intensity level of 10^{-2} is visible. Decreasing the output to 25 nJ reduces its intensity by ∼50 %. Bypassing the last FA-stages and connecting the output of the CFBG directly to the regenerative amplifier decreases the pre-pulse contrast at a distance $t > 7$ ps but leaves the post-pulse intensity unchanged. Without CPA at all, the pulse contrast is significantly increased, exceeding the noise-level of the THG-AC.
The CFBG is therefore identified as the main source for residual dispersion, but which can not be prevented. The second contribution arises from amplification in the final FA. At higher output energies, the temporal background is disproportionately amplified, resulting in a redistribution of energy from the main pulse into the wings. To diminish this effect but still have enough seed energy available to reach the period doubling regime at a reasonable number of roundtrips, the pre-amplification output energy is set to 25 nJ. In this configuration, the improved pulse contrast enhances the SHG-efficiency by 10 % up to 63 %. Further details regarding SHG follow in section 4.10.

4.9. Long-term Performance

A stable daily performance is an important criteria for the usability of a laser system. At the beginning of this work, the regenerative amplifier was only realized as a laboratory setup, placed on a simple optical breadboard, using a variety of different optical mounts and covered by only one large housing. Although the characteristics of output power and energy were initially the same, the stability of the system, precisely beam pointing, pulse-to-pulse fluctuations and power fluctuations, was significantly worse. After the final OPCPA concept was fixed, the system was therefore converted to a new platform to enhance the mechanical stability. In order to create an isolated environment for the amplifier, a massive, water-cooled aluminum-board with sealed, dedicated inner housings is set up. Where possible, rigid mirror mounts with flexure bearings are used. Resonator alignment can be performed remotely by means of motorized mirrors without opening the housing, which would give rise to air turbulences that disturb the beam path. An impression of the system before and after the conversion is given in figure 4.15.

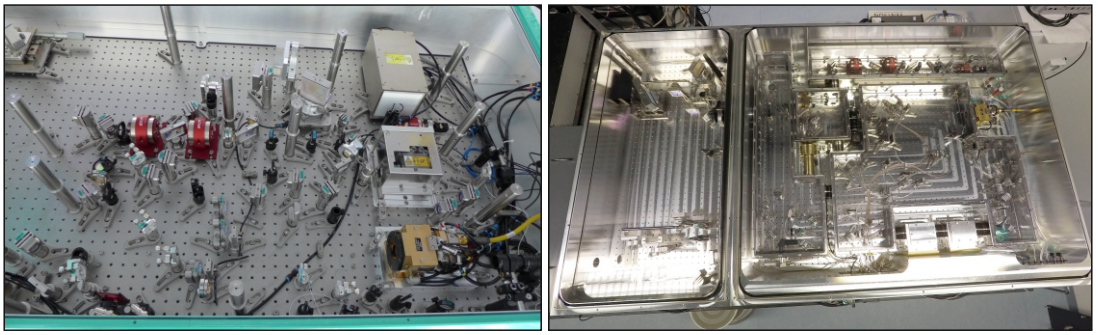

Figure 4.15.: Impression of the regenerative amplifier, realized as laboratory setup (left) and in its new platform (right), significantly improving the stability.

In the new platform, a constant output power over hours is achieved, which is shown in figure 4.16. After a start-up period of ∼1 h with occasional realignment, a stable setting is found at a slightly decreased output power of 165.3 W. The root-mean-square (rms) power fluctuation at this setpoint is below <0.33 %, using no additional means of electronic stabilization.

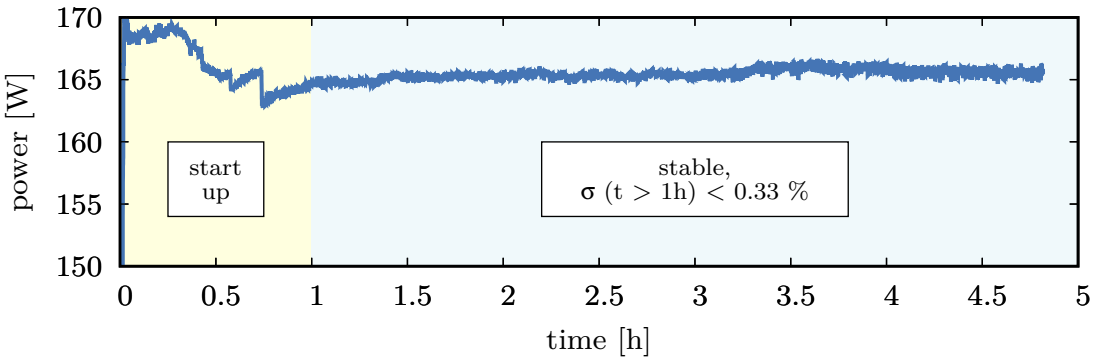

Figure 4.16.: Typical output power over time of the regenerative amplifier. A constant output power is reached after a warm-up time of ∼2 h.

In addition to a stable output power, low beam pointing is a desired feature. The beam pointing of the regenerative amplifier is characterized by a beam profiler (SP620U, Ophir Photonics) in the focal plane of a lens with $f = 1000\,\text{mm}$. In parallel, the temperature evolution inside the inner housing covering the resonator is measured with a temperature logger (174H, Testo). Figure 4.17 depicts the results. As soon as the pump diodes are switched on shortly after $t = 0$, the ambient temperature starts rising. The pointing measurement starts about 30 min later and reveals a vertical drift $>80\,\mu\text{rad}$ during the warm-up phase. After that, the vertical pointing is inverted and a slow drift, corresponding to the slope of the resonator temperature, is observed. In the horizontal, only minor drifts during the warm-up phase occur. After the last resonator alignment at $t \approx 1.9\,\text{h}$, no more significant drifts are visible. Only after 8 h, the resonator temperature settles and also the vertical drifts stop. The reason for the lengthy drift phase is the large volume of the resonator which prevents a faster thermalization of the environment. Minimizing the heat input from the disk via amplified spontaneous emission (ASE) by a special heat-sink or actively controlling the resonator temperature could speed up this process in the future. After settlement of the slow drifts, outstanding beam pointing values of $\sigma_h = 3.24\,\mu\text{rad}$ and $\sigma_v = 3.92\,\mu\text{rad}$ in the horizontal and vertical axis are measured over 30 minutes at $t > 8.5\,\text{h}$.

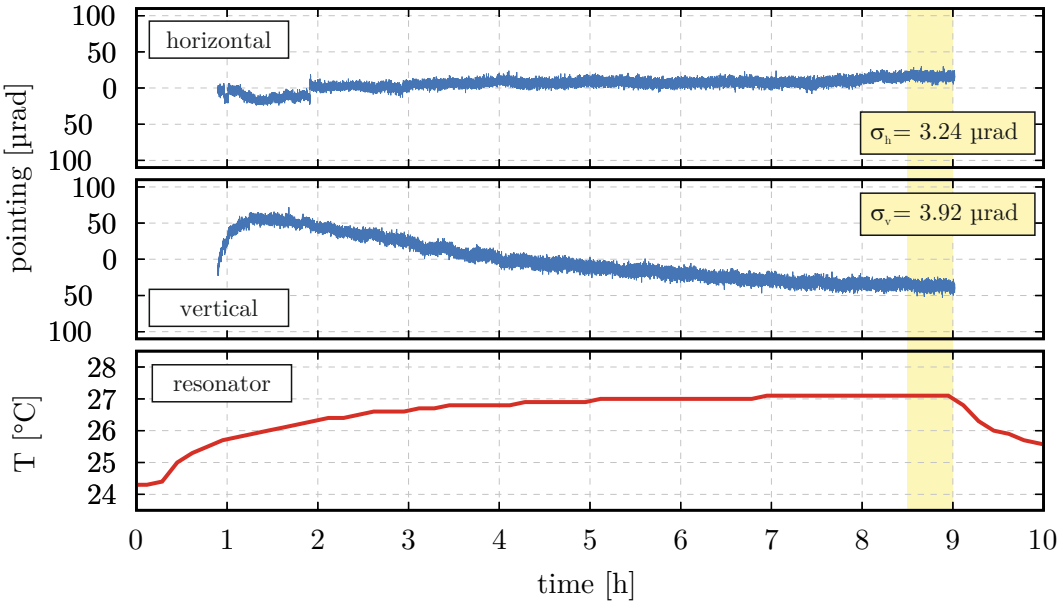

Figure 4.17.: Beam pointing and resonator temperature over time of the regenerative amplifier. After thermal drifts have settled, beam pointing values of $\sigma_h = 3.24\,\mu\text{rad}$ and $\sigma_v = 3.92\,\mu\text{rad}$ in the horizontal and vertical axis are measured.

4.10. Second Harmonic Generation

Broadband amplification around 800 nm in an OPA requires frequency doubling of the infrared pump source to satisfy energy conservation and phase matching condition. During the evolution of the OPCPA setup, different SHG configurations are utilized, which are explained in detail in chapter 6. All the employed stages are operated under comparable

conditions in a similar regime. A representative configuration is described in this section, while in the remaining part of this thesis, only the differing and relevant parameters will be given at the respective positions in the text.

In a straightforward approach, a single SHG stage is set up right after the regenerative amplifier output to convert the beam to 515 nm. A 2 mm-short lithium triborate, LiB_3O_5 (LBO) crystal with an aperture of $15 \times 15\,mm^2$ is used, cut at $\theta = 90°$ and $\varphi = 12.9°$ with an AR-coating for 1030 nm and 515 nm on both sides. The crystal is mounted in a temperature-controlled copper holder, stabilized to 40 °C to ensure long-term phase matching. The fundamental beam size is adjusted by a telescope to obtain an intensity of $\sim 120\,GW/cm^2$ at 165 W (27.5 mJ). Output power and efficiency of the SHG stage are depicted in figure 4.18 (a). 104.0 W in the green are obtained, corresponding to 63 % conversion efficiency and 17.3 mJ pulse energy. The pulse duration is measured with a SHG-autocorrelator (pulseCheck, APE GmbH) at maximum output power. Figure 4.18 (b) presents the acquired autocorrelation trace. The pulse duration equals that of the fundamental pulse as a result of the saturated conversion process. The minor satellite pulses, visible in the autocorrelation of figure 4.8 (a), are supressed by the quadratic intensity dependence of the SHG process, leading to a clean temporal pulse shape. At a pulse-to-pulse energy fluctuation of 1 % at 1030 nm, measured prior to the platform conversion of the system, the frequency doubled pulse energy varies by 1.35 % rms only.

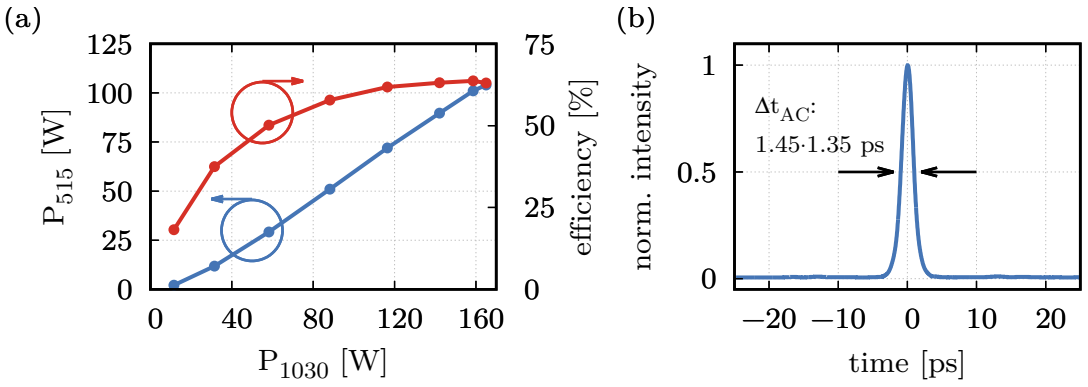

Figure 4.18.: (a) Conversion characteristics and (b) autocorrelation trace of a single SHG stage, employed after the regenerative amplifier.

4.11. Summary

Development and characterization of a regenerative amplifier has been presented in this section. The system delivers pulse energies of 28.9 mJ at a repetition rate of 6 kHz, corresponding to an average power of more than 173 W and an optical efficiency of 44.6 %. Derivation of the seed pulses directly from the Ti:Sa-oscillator provides optical synchronization between the amplified pulses and the oscillator output. A CPA concept utilizing a CFBG stretcher and a grating compressor minimizes the B-Integral and results in a pulse duration of 1.31 ps, ideally suited to pump an OPCPA system. The amplifier is operated in a stable period-doubling regime, exhibiting a pulse-to-pulse fluctuation below 0.65 %. A tilted lens is used to equalize the beam waist diameter in horizontal and vertical axis

and to reduce the beam ellipticity at the system output. M^2 values of 1.41 and 1.22 in horizontal and vertical direction are obtained, indicating an excellent beam quality. By reducing the output of the pre-amplification chain to 25 nJ, residual dispersion effects originating from nonlinearities in the final FA are decreased. With a higher amount of energy comprised in the main pulse, the efficiency of a SHG stage is increased by 10 % to a total of 63 %. Beam pointing values below 4 µrad are measured after thermal stabilization of the system. However, a long warm-up time up to 8 h is identified, which leads to slow vertical drifts with an amplitude >80 µrad. A drift compensation by means of an external beam stabilization is thus planned. The output power is not affected by the marginal thermal drifts after a start-up phase of 1 h and stays constant over hours with a rms fluctuation <0.33 %. The achieved parameters render the regenerative amplifier a well suited pump source for an OPCPA.

5. Pump-Seed Synchronization

5.1. Motivation

Due to the instantaneous nature of the OPA process, precise timing between the involved pulses is neccessary for stable operation. Timing fluctuations lead to [34, 56, 120]

- power and energy fluctuation,
- spectral shift,
- changing pulse duration,
- carrier-envelope phase instabilities,
- reduced efficiency.

A detailed investigation of those effects in a comparable system was carried out e.g. by Hädrich et al. [34]. Caused by a pump-seed timing offset of 20 % relative to the pump pulse duration τ_p, they measured a central wavelength shift of 5 nm, accompanied by a CEP-shift of 0.8 rad. Taking those values as a basis and aiming for a CEP stability comparable to the seed oscillator (70 mrad rms), a tolerable rms timing jitter is below $1.75\,\% \times \tau_p$. Beneath this threshold value, the wavelength shift reduces to < 0.5 nm rms.
Despite the implementation of all optical synchronization between pump and seed source as described in chapter 3, the pulses slip away in time. This is caused by the different beam paths in the optical setup: while the seed pulses are sent directly to the OPA over a typical distance of a few meters, the pump pulses need to be amplified first. During amplification, the propagation length can easily reach a thousand meters and more. A long beam path is more susceptible to disturbances such as vibrations and airflow or temperature changes, which induce fast or slow alterations of the pulse arrival times.
Figure 5.1 exemplarily shows the delay evolution between pump and seed pulses $\Delta t_{p,s}$ over time, measured in a high-power µJ-OPCPA system [72]. In (a), a slow temperature-induced long-term drift over two hours is shown. After this timespan, the difference of the pulse arrival times is as large as 5 ps. Considering a pump pulse duration around 1 ps,

the temporal overlap in the OPA stages would be completely lost. On a short timescale of 10 seconds, presented in figure 5.1 (b), a timing jitter with peak deviations up to 200 fs is visible. This is already more than 15 % of the pump pulse duration and thus not tolerable, as it results in the timing-dependent instabilities mentioned at the beginning.

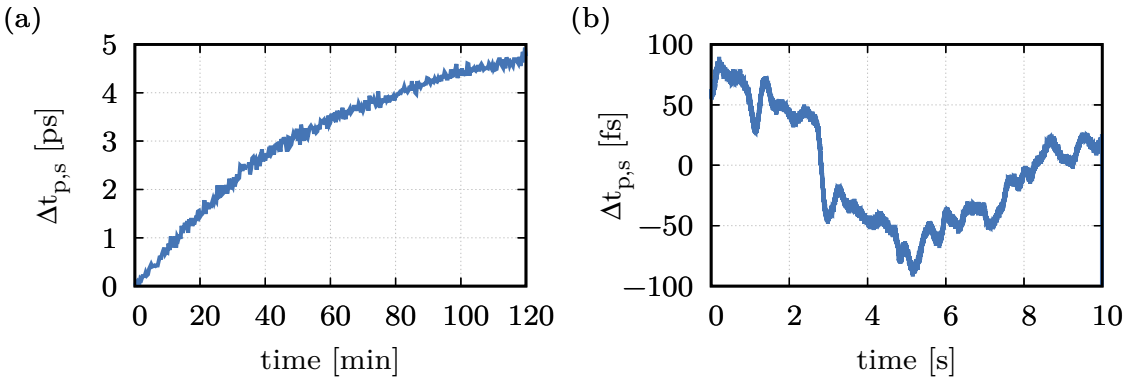

Figure 5.1.: Exemplary evolution of the relative timing delay between pump and seed pulse without active synchronization. (a) Long-term drift and (b) fast fluctuations.

As a result, pump and seed pulses have to be actively locked in time to ensure long-term stability of the OPCPA. The designated synchronization system must be capable of handling both, fast and slow timing fluctuations. In order to lock the timing offset, the current pump-seed delay must first be measured with high precision and can subsequently be compensated by adjusting the optical path length via an integrated delay line. In the following, the most common delay measurement techniques with their advantages and disadvantages are addressed briefly, followed by the presentation of the herein developed pump-seed synchronization (PSS).

5.2. Pulse Delay Measurement

In order to synchronize two pulses in time, their relative delay has to be measured first. This is not a straightforward task, since a precision in the fs-range is required. Conventional electronics, e.g. photodiodes, are not capable of such a resolution due to their limited response time. This problem can be circumvented by measuring the output of a nonlinear process that is highly dependent on the timing delay and thus provides an indirect access to the current pulse delay. The most common measurement techniques of this kind are presented hereafter.

5.2.1. Intensity Cross-Correlation

The simplest approach to measure the relative delay between two pulses is optical intensity cross-correlation, practically realized by a SFG or DFG process. The output signal is the convolution of the two input signals and directly dependent on the temporal overlap. A photodiode measures the signal intensity I which is locked to a specific value, e.g. $I(t_1)$, to stabilize the relative pulse delay. The concept is presented in figure 5.2.

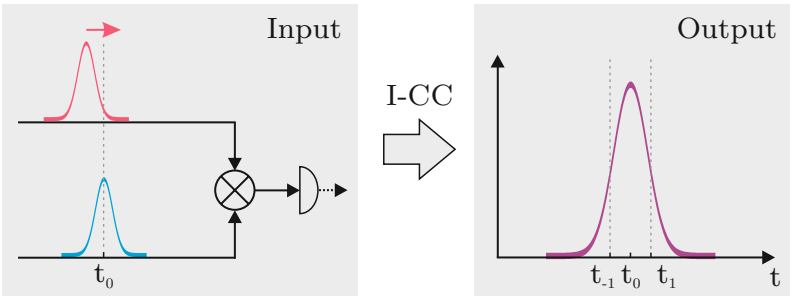

Figure 5.2.: Concept of intensity cross-correlation.

Advantages and disadvantages:

+ Easy implementation

– Limited measurement range

– Signal ambiguity of positive and negative relative delay ($I(t_{-1}) = I(t_1)$)

– Pulse intensity fluctuations are interpreted as timing shifts.

5.2.2. Balanced Optical Cross-Correlation

A balanced optical cross-correlator consists of two nearly identical optical intensity cross-correlators. In one arm, a defined pulse delay between both pulses is introduced which influences the output of the respective cross-correlation process. The ouput of each arm is now measured by a photodiode and their differential signal is locked to zero. Various balanced optical cross-correlation setups exist today. A typical setup is shown in figure 5.3, adapted from [87]. So far, the synchronization of two different OPA outputs, seeded by the same source, was demonstrated with only 30 as rms remaining timing jitter [54]. In a scenario similar to the herein presented setup, reduction of the timing jitter to 17 fs rms has been achieved between a Ti:Sa-oscillator and an optically synchronized high-power amplifier [9].

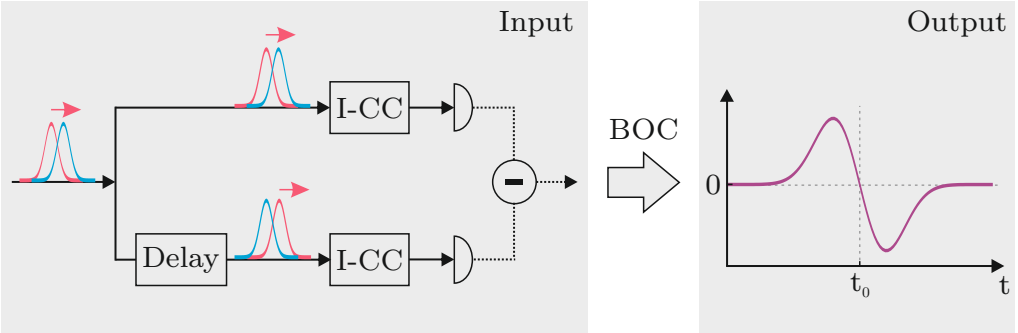

Figure 5.3.: Concept of balanced optical cross-correlation.

Advantages and disadvantages:

+ Differential signal is intensity independent in the ideal case

+ Measurement with as-precision possible
– Complex optical setup
– Limited measurement range
– Signal ambiguity when not in the vicinity of the zero crossing

5.2.3. Spectrally Resolved Cross-Correlation

In spectrally resolved cross-correlation, a broadband seed pulse is stretched in time by a dispersive medium to a multiple of the pump pulse duration. Pump and seed are overlapped in a nonlinear medium, generating a signal with the central wavelength dependent on the relative delay between the pulses. In the easiest case, the output is detected by a spectrometer and fed back to the delay line which locks the central wavelength. Figure 5.4 shows the basic concept. This technique was developed in 2000 by Miura et al. [59], utilizing SFG in the detection scheme and reducing the timing jitter between a Ti:Sa-oscillator and a Ti:Sa-amplifier from 5 fs to 0.6 fs rms. Schwarz et al. used the same scheme in 2012 in an OPCPA to stabilize the jitter between a Ti:Sa-oscillator and an optically synchronized high-power amplifier to 24 fs rms [91].

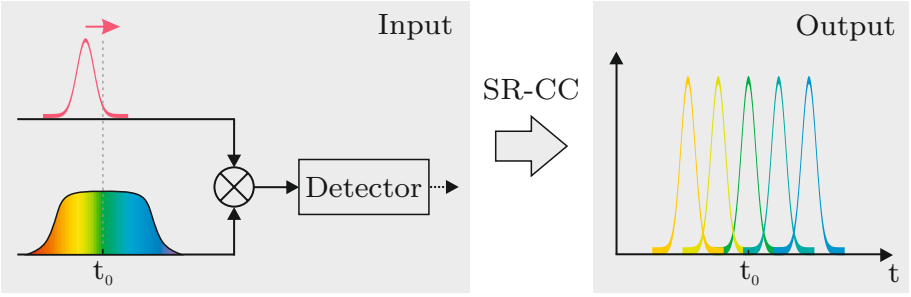

Figure 5.4.: Concept of spectrally resolved cross-correlation.

Advantages and disadvantages:

+ Intensity independent delay measurement
+ No signal ambiguity
+ High precision and large measurement range possible
– Requires a broadband pulse and a nonlinear process with broadband phase matching.

From all the measurement techniques presented, spectrally resolved cross-correlation is the only one which potentially allows a large measurement range in combination with a high precision. Since the purpose of OPCPA is the amplification of a broadband seed pulse, it is straightforward to use this method to measure and stabilize the relative pump-seed delay.

In the next section, the experimental implementation of the complete system based on spectrally resolved cross-correlation is described in detail.

5.3. Experimental Implementation

In the context of this thesis, a total of three PSS systems have been set up and used in different OPCPA systems. The first PSS, referred to as PSS_α, is implemented in the µJ-OPCPA, which has been published in [72] and will be reviewed briefly in section 5.3.1.1. The second one, PSS_β is utilized in the herein developed high energy OPCPA, presented in chapter 6, while the third one, $PSS_{\beta,2}$, is used only temporary in addition to PSS_β for out-of-loop measurements. Although the underlying basic principle remains the same, the introduced systems differ in two main aspects:

- The length of the dispersive medium to stretch the seed pulse and
- the pump source and its parameters.

Unless otherwise stated, this section describes the PSS concept based on the experimental parameters of PSS_α. The differences between the systems are described at appropriate places in the text and are summarized in table 5.1.

5.3.1. Optical Setup

5.3.1.1. Error Signal Generation

The first step in the design of the PSS is the definition of the nonlinear interaction process that generates the delay-dependent error signal. Comparable systems [91] used SFG, requiring relatively high seed energies of 670 nJ to achieve a sufficient signal strength for detection. If DFG was used instead, the signal wavelength would be above 1.1 µm which restricts the use of silicon-based detection devices. Those disadvantages do not apply to the OPA process. Here, the signal covers the spectral range of the seed (∼700 nm to 1000 nm) and only low seed energies are required to generate a reliably detectable output. The spectrally-resolved optical parametric amplification (SR-OPA) stage can be setup in the same fashion as the main OPA stages to achieve broadband phase matching. A potential disadvantage is the lack of spectral and spatial separation between seed and signal, thus requiring background subtraction of the seed to achieve a high detection signal-to-noise ratio (SNR). Since the latter can be implemented in the signal readout electronics, an OPA process is chosen to generate the error signal.

Figure 5.5 presents the schematic setup of the PSS. As mentioned before, all parameters refer to the implementation of the system in the µJ-OPCPA, which is described briefly hereafter.
In this OPCPA system, the pump source delivers up to 200 W of average output power at $\lambda = 1030$ nm with a repetition rate of 300 kHz and a pulse duration of 1.3 ps. After frequency doubling in a 1.5 mm-short LBO crystal to $\lambda = 515$ nm, a final pump power of 140 W ($E_p = 467$ µJ) with a pulse duration of 1.2 ps is available. The Ti:Sa-oscillator presented in chapter 3 is used to seed a two-stage OPCPA chain, delivering 15 W, 50 µJ and sub-6 fs pulses after compression [72].

Right after the seed source, a delay line is placed in the beam path to adjust the arrival time of the seed pulses relative to the pump pulses. A piezo actuator with a travel range

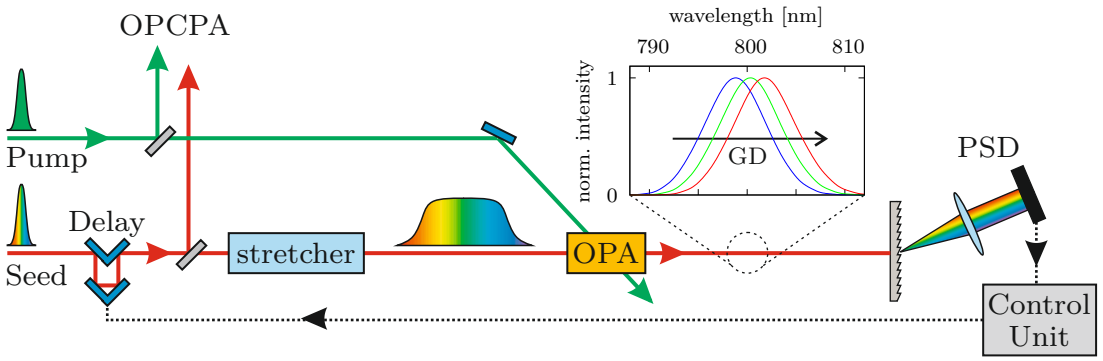

Figure 5.5.: Schematic setup of the PSS, based on SR-OPA. The inset shows the simulated spectral output at a relative delay $\Delta t_{p,s}$ of −100 fs, 0 fs and 100 fs. BS: beam splitter, VNDF: variable neutral density filter, G: transmission grating, L: projection lens, PSD: position sensitive detector.

of 100 µm (PX100, piezosystem Jena GmbH) is combined with a long-range motorized translation stage (M-404.42S, Physik Instrumente (PI) GmbH, 100 mm travel range) to compensate for fast and slow temporal drifts, respectively. To guide the beam, a leight-weight prism retroreflector with a total mass of 11 g is mounted on top of the piezo stage. Thanks to the low mass, the nominal resonance frequency of 790 Hz is only slightly reduced to 673 Hz. A high resonance frequency is of importance, because it is one factor that limits the bandwidth of the active feedback by disturbing the feedback gain [53].

To measure the relative pump-seed delay, a small fraction of seed and pump energy is split off before the main OPCPA and utilized in the PSS. A broadband beamsplitter with a fixed transmission ratio of 20 % is used in the seed arm, transmitting $E_s = 400$ pJ to the PSS, while a pump energy transmission ratio of 2% ($E_p = 10$ µJ) is set by a waveplate combined with a TFP. The detection setup is placed as close as possible to the first main OPCPA stage to avoid additional timing jitter accumulation after the beam splitting. In the PSS, the broadband seed pulses are stretched in time by a highly dispersive 100 mm-long SF57 bulk glass block to a duration of ∼25 ps. Subsequently, seed and pump beam are focused into a 5-mm short BBO crystal, cut at $\theta = 24°$ and aligned for broadband phase matching, under a noncollinear angle of $\alpha \approx 2.4°$. The focal spot size of the seed ($w_s = 100$ µm) is chosen to be slightly larger than the pump ($w_p = 70$ µm) to ensure spatial overlap inside the crystal and reduce the influence of beam pointing on the signal intensity. Because of the small spot sizes, PVWC geometrie is employed. Depending on the relative delay between the short pump and the stretched seed pulses, a specific spectral fraction of the seed spectrum is amplified in the OPA process. The inset in figure 5.5 shows the SR-OPA output spectra at relative delays $\Delta t_{p,s} = t_p - t_s$ of −100 fs, 0 fs and 100 fs, simulated with chi2D [50]. A negative $\Delta t_{p,s}$ indicates a delayed pump pulse with respect to the seed pulse. An increasing delay results in a spectral red-shift of the central wavelength in the amplified signal, with its magnitude only depending on the dispersion of the seed.

Minimum Pump Pulse Energy

The necessary pump pulse energy can be further decreased as long as the intensity in the OPA crystal is kept constant at $\sim$100 GW/cm^2 by adapting the focal spot size. A final limitation is set by the spatial walk-off between pump and seed which leads to a separation d of the two beams. Considering a 5 mm-short BBO crystal at $\theta = 24.3°$ and a noncollinear angle of 2.4°, the total walk-off amounts to $\sim$16.5 mrad. The resulting separation of the beam axes at the crystal entrance and exit thus calculates to

$$\frac{5\,\text{mm} \cdot 16.5\,\text{mrad}}{2} \approx 40\,\mu\text{m}.$$

Under the assumption that pump and seed beam have the same beam diameter ($w_s = w_p$) and a complete separation of both beams at the crystal exit is tolerated ($d \leq 2w_p$, neglecting divergence), the beam separation equals the minimum focal spot size and results in a minimal pump energy of $\sim$3.4 µJ.

Minimum Seed Pulse Energy

In order to determine the minimum seed energy for signal generation, a variable neutral density filter is implemented in the seed arm. The transmitted seed energy is monitored with a calibrated photodiode. At a constant pump pulse energy of $E_p = 10\,\mu$J and an intensity of 100 GW/cm^2, the amplified signal energy at different seed levels is measured. The results are depicted in figure 5.6. A seed energy as low as 4 pJ marks the threshold for a usable signal in this configuration. Below, the signal energy drops beneath the detection limit of $\sim$200 pJ and the pulse contrast $E_{\text{signal}}/E_{\text{seed}}$ decreases rapidly. Up to this point, the pulse contrast is even improved by a lower seed level and enhances the measurement fidelity.

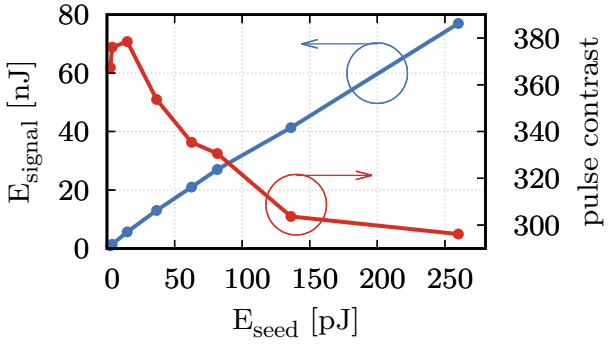

Figure 5.6.: Determination of the minimum seed pulse energy for the error signal generation. A signal energy above 200 pJ is required by the detection system. A higher signal pulse contrast enhances the measurement fidelity.

5.3.1.2. Error Signal Characterization

Spectral System Behaviour

The spectral system behavior of PSS$_\alpha$ is characterized by measuring the output spectra of the SR-OPA with a spectrometer (USB2000, Ocean Optics, Inc.). The relative delay $\Delta t_{p,s}$ is scanned by moving the employed linear stage. In the bottom part of figure 5.7 the delay dependent normalized SR-OPA spectra in a range between -12 ps and 7.5 ps are

presented. The upper part gives an example of the spectral shape at different delays and hence, different central wavelengths. All spectra exhibit a well defined central wavelength. No ambiguities that could disturb the feedback control are detected throughout the whole measurement range.

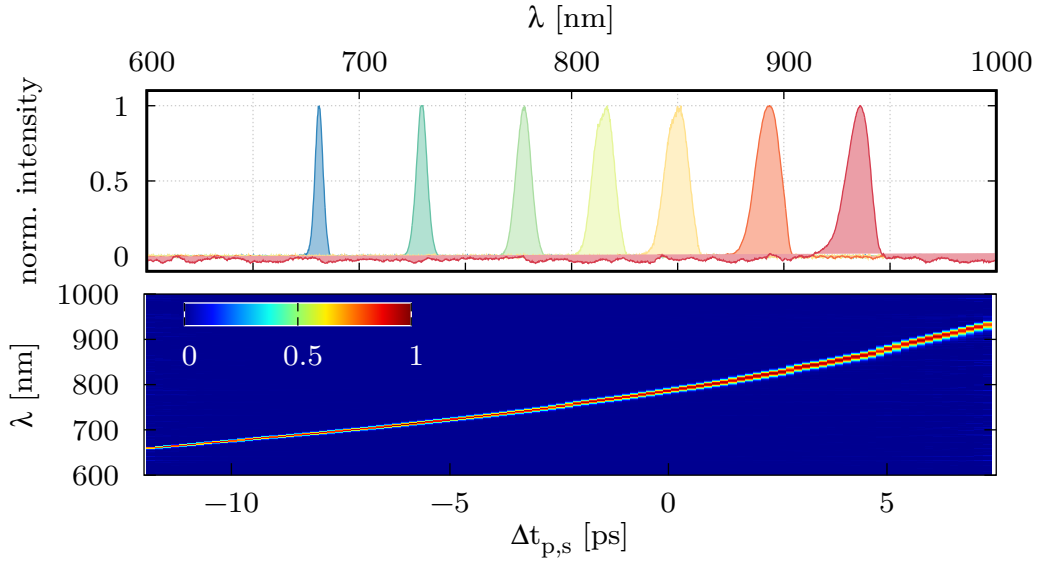

Figure 5.7.: Measured spectral system behavior of PSS_α.

The setpoint $\Delta t_{p,s} = 0\,\text{ps}$ is adjusted to a central wavelength of 820 nm, where the maximum parametric gain is achieved and minimum pulse-energy fluctuations below 3 % rms are measurable. This is accomplished in the experimental setup by the horizontal adjustment of a deflection mirror in front of the grating, which changes the relative signal position on the detector.

5.3.1.3. Error Signal Measurement

As implemented in the previous section, the obvious way to measure the SR-OPA signal is to use a spectrometer. However, most spectroscopic devices suffer from long integration and data processing times, usually in the ms-range, which limits the acquisition bandwidth and prevents the detection of fast jitter contributions. Therefore, a blazed transmission grating with 300 lines/mm (GT13-03, Thorlabs GmbH) is used to diffract the signal at a wavelength-dependent angle through a projection lens ($f = 50\,\text{mm}$) onto a position-sensitive detector (PSD) (1L5, Sitek Electro Optics AB), where the position of the centroid is detected. Consequently, the centroid is directly correlated to the relative timing delay between the pump and seed pulses and can be used as the error signal for the control loop.

The signal position x_{PSD} on the PSD in dependence of the relative timing delay $\Delta t_{p,s}$ between the pulses in such an optical system can be calculated by the following steps:

1. Calculate the wavelength shift $\Delta\lambda = \lambda - \lambda_0$ from the reference wavelength λ_0 at $\Delta t_{p,s} = 0$ in dependence of $\Delta t_{p,s} = t_p - t_s$. Assuming an initially unchirped seed pulse, the instantaneous wavelength distribution after transmission of the stretcher material with length L is defined by the introduced dispersion as derived from the

Sellmeier equation. Hence, the delay between two instantaneous wavelengths is given by the resulting difference in the GD,

$$\Delta t = \mathrm{GD}(\lambda) - \mathrm{GD}(\lambda_0) = \Delta\mathrm{GD}(\Delta\lambda). \tag{5.1}$$

Vice versa, the wavelength shift caused by $\Delta t_{p,s}$ can be calculated from a known GD distribution

$$\Delta\lambda = \mathrm{GD}^{-1}(t_p) - \mathrm{GD}^{-1}(t_s) = \Delta\mathrm{GD}^{-1}(\Delta t_{p,s}) \tag{5.2}$$

which allows the calculation of the corresponding new central wavelength λ_{centr} according to

$$\lambda_{\mathrm{centr}} = \lambda_0 + \Delta\lambda = \lambda_0 + \Delta\mathrm{GD}^{-1}(\Delta t_{p,s}). \tag{5.3}$$

2. Calculate the grating diffraction angle β in dependence of the central signal wavelength λ_{centr}. This is accomplished by using the grating equation:

$$Nm\lambda = \sin(\alpha) - \sin(\beta), \tag{5.4}$$

with the grating constant N, the diffraction order m and the incident angle α. Here, α is set to 0° and the diffraction order $m = -1$ is used, yielding

$$\beta = \arcsin(N\lambda_{\mathrm{centr}}) \tag{5.5}$$

3. Calculate the the projected PSD position x_{PSD} in dependence of the grating diffraction angle β. With grating and PSD positioned in the focal plane f of the projection lens, geometrical analysis yields for thin lenses

$$x_{\mathrm{PSD}} = f \cdot \tan(\beta). \tag{5.6}$$

4. Substituting β in equation 5.6 with 5.5 and utilizing 5.3 finally results in

$$x_{\mathrm{PSD}} = f \cdot \tan\Big(\arcsin\Big(-N[\lambda_0 + \Delta\mathrm{GD}^{-1}(\Delta t_{p,s})]\Big)\Big). \tag{5.7}$$

Figure 5.8 shows the calculated system behavior of PSS_α and closely resembles the measurement presented in figure 5.7. A perfect pulse overlap, $\Delta t_{p,s} = 0$, is assumed at the previously defined reference wavelength $\lambda_0 = 820\,\mathrm{nnm}$. By definition, this corresponds to the signal being at the center of the PSD, $x_{\mathrm{PSD}} = 0\,\mathrm{mm}$. The optical components of the setup were chosen to fit the majority of the signal spectrum onto the detector, taking into account the lateral PSD size of 5 mm (marked with horizontal dashed lines). In theory, this configuration allows the measurement of a relative timing delay between $-14\,\mathrm{ps}$ and 7 ps, indicated as a green area in the graph. In practice, the measurement range is limited by the signal bandwidth, which is determined by the phase matching. The wide detection range makes the system intrinsically stable, even in case of strong transient events, and allows an easy recovery of the temporal overlap in daily operation.

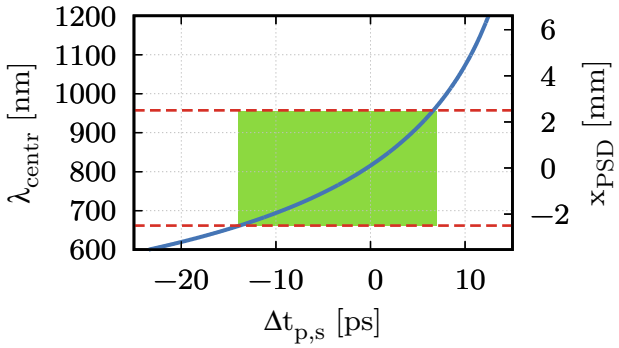

Figure 5.8.: Calculated system behavior of PSS_α, using 100 mm SF57 as stretcher, a transmission grating with $N = 300$ lines/mm and a projection lens with $f = 50$ mm. The dashed lines indicate the size of the PSD which determines the theoretical measurement range (green area).

In the context of size and cost reduction for the final PSS product, the length of the 100 mm-long SF57 stretcher used in PSS_α has been halved to 50 mm in PSS_β and $PSS_{\beta,2}$. The calculated system behavior in this case is depicted in figure 5.9. With only half the GDD applied to the seed, the measurement range is reduced to relative delays between −7 ps and 3.25 ps. Simultaneously, the wavelength resolution is increased thanks to the larger delay-dependent central wavelength shift $\partial\lambda_{\text{centr}}/\partial\Delta t_{p,s}$.

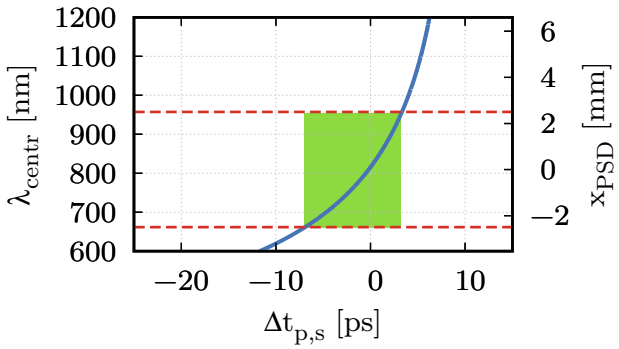

Figure 5.9.: Calculated system behavior of PSS_β and $PSS_{\beta,2}$, using 50 mm SF57 as stretcher, a transmission grating with $N = 300$ lines/mm and a projection lens with $f = 50$ mm. The dashed lines indicate the size of the PSD which determines the theoretical measurement range (green area).

5.3.2. Electronics

The performance of the synchronization is not only dependent on the quality of the optical error signal, but also on its detection and compensation. The detection speed and its resolution are determined by the detector and the processing electronics, which ultimately limits the feedback bandwidth and the dynamic range. Compared to segmented components as e.g. diode arrays, PSDs provide a continuous measurement and thus feature a high spatial resolution at high speed.

As mentioned before, the SR-OPA signal at 300 kHz is superimposed by the broadband seed pulses at 80 MHz. If not taken into account, the unamplified seed pulses generate a constant offset voltage inside the PSD readout electronics which results in an intensity dependent centroid detection of the signal and distorts the accuracy of the measurement. On that account, an analog readout was designed that detects the offset in the time interval between two SR-OPA pulses and subtracts it from the acquired PSD signal. This approach yields a clean detected pulse with high position fidelity and no intensity dependence, which is demonstrated later on. The analog position signal is detected by a sample-and-hold circuit, converted into a digital signal and sent to the control unit. The control unit

processes all data directly in the integrated CPU, including the calculation of the feedback signal $y(t)$ according to

$$y(t) = K_p \cdot e(t) + K_i \cdot \int_0^t e(\tau)\,\mathrm{d}\tau, \tag{5.8}$$

which represents a proportional-integral (PI) controller with the proportional term K_p, the integral term K_i and the error signal $e(t)$, defined as the difference between the setpoint and the current position. It also features direct communication to the delay line hardware, minimizing the system response time and allowing real time operation as a standalone device.

To characterize linearity and SNR of the detection system, the output of the pump source is focused directly to the PSD by a lens with $f = 50\,\mathrm{mm}$, resulting in a focal spot size of $\sim$75 µm. The 1030 nm-pulses are attenuated to 500 pJ at 100 kHz and scanned over the detection area. The energy is chosen to be half the saturation energy of the PSD, resembling the envisaged setpoint. Figure 5.10 (a) shows the retrieved signal position x_{meas} and the corresponding SNR, which is calculated according to

$$\mathrm{SNR}\,[\mathrm{dB}] = 20 \cdot \log \frac{L_{\mathrm{PSD}}}{\sigma}, \tag{5.9}$$

where $L_{\mathrm{PSD}} = 5\,\mathrm{mm}$ is the lateral size of the detector and σ the standard deviation of x_{meas} in a timespan of 1 s. The best performance is measured in the center where the SNR is as high as 80 dB, corresponding to a noise limited spatial resolution of 0.5 µm. The position is retrieved reliably over the whole detection area with high linearity.

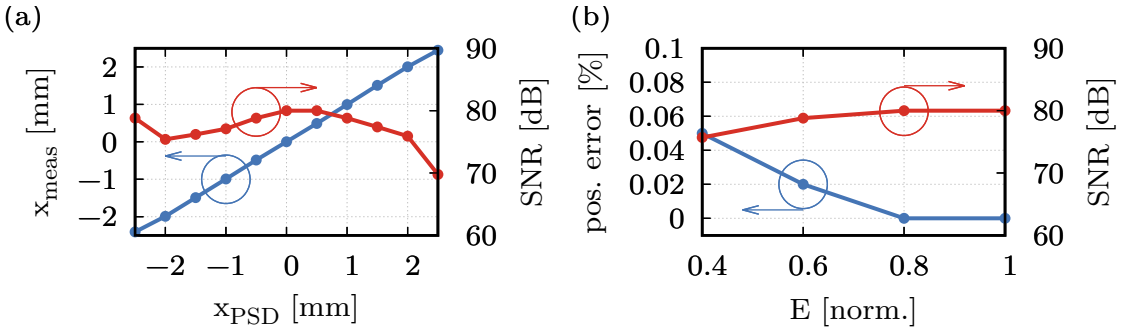

Figure 5.10.: Measured PSD characteristics: (a) measured signal position x_{meas} and SNR at different signal positions x_{PSD} on the detector and (b) position error and SNR at different relative signal energies E.

In order to test the influence of signal energy variations on the system, the SNR and the position error are measured in the center of the PSD. Figure 5.10 (b) shows a slight decrease of the SNR from 80 dB at $E = 500\,\mathrm{pJ}$ to 74 dB at a 60 % lesser energy of 200 pJ. Even at a 20 % decrease of the signal energy, the position is exactly retrieved and only a negligible position error of 0.05 % is apparent at 200 pJ. Since peak-to-peak energy fluctuations far below 20 % are expected from the SR-OPA, the detection is considered to be intensity independent.

In systems with high repetition rates f_{rep}, the SNR can be improved by averaging x_{meas} over multiple measurements. Assuming a Gaussian noise distribution, averaging over n measurements improves the SNR by a factor of $\sqrt{n}$. This technique can be utilized as long as the final sampling rate after averaging, $f_s = f_{\mathrm{rep}}/n$, is sufficiently high compared to the timing jitter bandwidth which is supposed to be compensated. In the case of PSS_α, f_{rep} equals 300 kHz, given by the pump source. Frequency analysis of the free-running delay drift in figure 5.1 (b) reveals that the timing jitter is located in a bandwidth below 10 Hz (presented later in figure 5.14). Thus, the position measurement is averaged over $n = 30$ consecutive pulses, performed directly in the detection electronics. A sample rate of $f_s = 10$ kHz is obtained, which is still three decades above 10 Hz. Furthermore, the influence of high frequency electronic noise is reduced by implementing a low-pass filter with a cut-off frequency of 1 kHz, well above the resonance frequency of the piezo actuator. By this means, the SNR in the center of the PSD is improved to 103 dB, enhancing the spatial resolution to 35 nm without reducing the feedback bandwidth.

In comparison to this, PSS_β and $\mathrm{PSS}_{\beta,2}$ are operated at lower repetition rates of 6 kHz. Hence, only low-pass filtering and no averaging is used, yielding an SNR of 82 dB in the center of the PSD.

5.3.3. Calibration

The purpose of the PSS is to lock $\Delta t_{p,s}$ to a specific setpoint, which is by definition $\Delta t_{p,s} = 0$. To fulfill this task, no calibration is required because only relative values are regarded by the active feedback loop. However, a calibration is necessary to calculate the remaining timing jitter of the stabilized system, an important parameter to determine the quality of the stabilization.

In general, the PSS can be calibrated by measuring the change of the signal position Δx_{meas} on the PSD while introducing a defined delay $\Delta t_{p,s}$ between pump and seed pulses. The linear calibration factor in the vicinity of the current position is then given by

$$K = \frac{\Delta t_{p,s}}{\Delta x_{\mathrm{meas}}}. \tag{5.10}$$

Because the system behavior is not linear throughout the complete measurement range, a calibration has to be performed for every value of x_{meas} where a precise measurement is required. In the stabilized case, only the timing jitter in the setpoint $x_{\mathrm{meas}} = 0$ mm is of interest.

K is sensitive to the alignment of the system and especially to the distances between the optical key elements, namely the nonlinear crystal, the grating, the projection lens and the PSD. For this reason, two PSS with an identical setup will likely have different calibration factors. The ongoing delay fluctuations between pump and seed pulses superimpose any artificially introduced pulse delay and represent a challenge to the procedure. In the following, two calibration techniques are presented which yield reproducible results even under these conditions.

Large Delay Calibration

The large delay calibration method uses large artificial delays compared to the fast timing jitter in the range of a few 100 fs in order to minimize the measurement error. It is best performed after pump and seed laser have reached a thermal equilibrium, where slow thermally induced drift effects as depicted in figure 5.1 (a) are minimal.

Figure 5.11 presents the calibration of PSS_α. A total delay range of about ±3 ps around $x_{\mathrm{meas}} = 0$ mm has been measured by moving the integrated translation stage of the delay line in steps of 100 µm, resulting in an artificial delay of $(2 \cdot 100\,\mu\mathrm{m})/c = 667.13$ fs per step. The corresponding position on the PSD is determined as the mean value from a sample of 10 000 consecutive samples. A second order polynomial least squares fit is applied to the measurement in order to match the calculated system behavior in figure 5.8 for large delays.

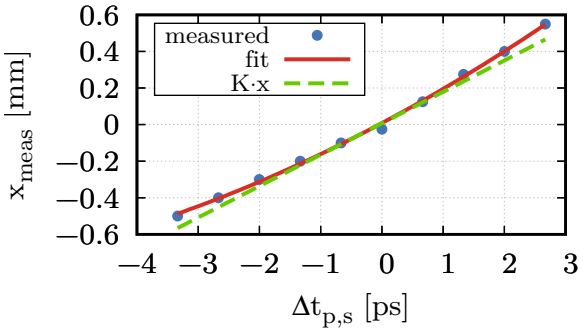

Figure 5.11.: PSS_α calibration results using the large delay method. A second order polynomial fit is applied to the measurement. The tangential slope at $x_{\mathrm{meas}} = 0$ mm yields the calibration factor K in the setpoint of the system.

Every acquired point of the calibration curve is subject to a measurement uncertainty in both dimensions. The reference delay $\Delta t_{p,s}$ is affected by the accuracy of the employed stage, indicated by the manufacturer with a standard error of <1.6 µm, corresponding to ±5.33 fs. The PSD position is affected by the short-term timing jitter, as shown in figure 5.1 (b), which introduces a standard error of 9.4 µm. Both errors are assumed to be constant for every measured sampling point over the full range. This is a valid assumption, as on the one hand the accuracy is a fixed mechanical property of the stage and on the other hand, the PSD position is retrieved with an approximately constant SNR throughout the calibration range (compare figure 5.10). Hence, no weighting is performed in the fit procedure.
To obtain the calibration factor K in the setpoint, the tangential slope of the fit at $x_{\mathrm{meas}} = 0$ mm is calculated. The uncertainty according to GUM [76] is given by the standard error of the fitted first order coefficient. This yields a calibration factor of

$$K_{\mathrm{PSS}_\alpha} = 5.8211 \pm 0.0860 \,\frac{\mathrm{ps}}{\mathrm{mm}}$$

with a relative error of 1.48 %. Since this calibration method covers a large fraction of the PSD it allows the derivation of a calibration factor for all positions x_{meas} within the calibration range directly from the polynomial fit.

The same calibration procedure has been conducted for PSS_β, with the calibration curve

depicted in figure 5.12. The calibration factor is calculated to be

$$K_{\mathrm{PSS}_\beta} = 2.1727 \pm 0.0025 \,\frac{\mathrm{ps}}{\mathrm{mm}}$$

with a relative error of 1.02 %. The reduction of the relative error is a result of the larger covered PSD range x_{meas}, caused by the increased delay-dependent central wavelength shift $\partial\lambda_{\mathrm{centr}}/\partial\Delta t_{p,s}$ in this system.

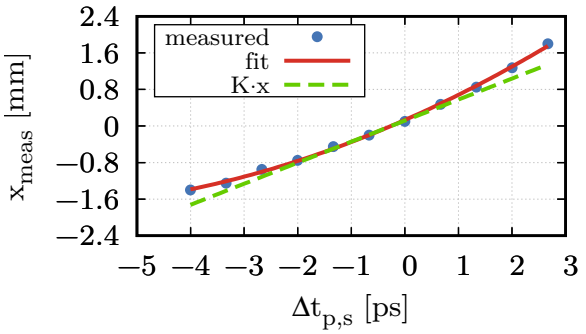

Figure 5.12.: PSS_β calibration results using the large delay method. A second order polynomial fit is applied to the measurement. The tangential slope at $x_{\mathrm{meas}} = 0\,\mathrm{mm}$ yields the calibration factor K in the set-point of the system.

Outlook: Carrier Frequency Calibration

In future systems, the integration of a carrier frequency calibration method is planned that potentially yields faster and more precise calibration results. In this method, the pump-seed delay is modulated by a continuous sinusoidal oscillation with a carrier frequency f_{sin} and a fixed amplitude of $\Delta t_{p,s}$ which needs to be large enough to be clearly distinguished from the overlaying timing jitter in the frequency domain. Determination of the signal amplitude at f_{sin} enables the measurement of the related displacement of x_{meas} and the calculation of the calibration factor K.

So far, the integration of this approach was hindered by the availability of suitable hardware. Specifically, a closed-loop piezo actuator with high bandwidth is required to introduce a sinusoidal oscillation of high frequency with a well known amplitude. Alternatively, the oscillation of the internal open-loop piezo actuator can be calibrated in the future by matching the introduced PSD centroid offset to the corresponding delay of the linear stage. This is less precise, but offers the advantage of using only preexisting components.

5.4. Results

This section presents the different conducted measurements which have been conducted to characterize the performance of the PSS. The focus is set on the results acquired with PSS_α. The out-of-loop performance is characterized with the systems PSS_β and $\mathrm{PSS}_{\beta,2}$. The most important parameter differences among the PSS systems, namely the acquisition frequency f_{acq}, the achievable SNR in the center of the PSD $\mathrm{SNR}_{\mathrm{cent}}$, the length of the SF57-stretcher L_{SF57}, the thereby given relative delay detection range DR and the calibration factor K, are summarized in table 5.1.

Table 5.1.: Differing parameters between the PSS systems.

	f_{acq}	$\mathrm{SNR}_{\mathrm{cent}}$	L_{SF57}	DR	K
PSS_{α}	300 kHz	103 dB	100 mm	21.0 ps	5.6794 ps mm^{-1}
PSS_{β}	6 kHz	82 dB	50 mm	10.25 ps	2.1727 ps mm^{-1}
$\mathrm{PSS}_{\beta,2}$	6 kHz	82 dB	50 mm	10.25 ps	3.0947 ps mm^{-1}

5.4.1. Synchronization

5.4.1.1. Short-term Timing Jitter

The short-term delay fluctuation between pump and seed pulses in the µJ-OPCPA is measured using PSS_{α} with an acquisition bandwidth of 10 kHz as described in section 5.3.2. A low-pass filter with 1 kHz is applied, since no significant contributions to the timing jitter are expected at higher frequencies. During the measurement, the pump source was running at full output power, where thermal effects are most pronounced.

Figure 5.13 (a) shows the timing jitter in the case of the free-running system, which has been already presented in the beginning of this chapter, compared to the case with active synchronization. Both measurements were performed in-loop over a period of 10 s 100 000 samples). In the unsynchronized case, peak-to-peak delay fluctuations of up to 200 fs are revealed. This corresponds to more than 15 % of the pump pulse duration and makes stable operation of the OPCPA impossible.
The situation is significantly improved with activated feedback from the PSS. The pulses are locked in time with a remaining relative timing jitter of $\sigma_{p,s} = 2.76 \pm 0.04$ fs rms in a bandwidth from 0.1 Hz to 1 kHz. This equals ∼0.23 % of the pump pulse duration, which is more than seven times below the targeted threshold value of 1.75 % rms defined in the beginning of this chapter. The system therefore guarantees a stable overlap of the pulses in the OPCPA stages.

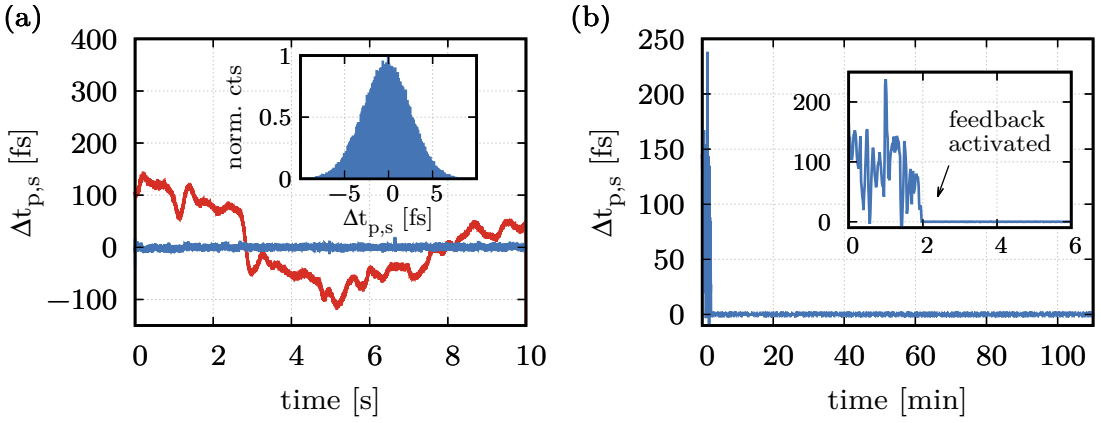

Figure 5.13.: (a) Short-term timing jitter $\Delta t_{p,s}$ without synchronization (red) and with activated synchronization (blue). The remaining relative timing jitter is reduced to $\sigma_{p,s} = 2.76 \pm 0.04$ fs. The inset shows a histogram of the measured values of $\Delta t_{p,s}$. (b) Long-term measurement of $\Delta t_{p,s}$, with activated feedback after 2 min (inset).

The reliability of the system and its long-term performance are presented in figure 5.13 (b). $\Delta t_{p,s}$ is measured over two hours at an acquisition rate of 10 Hz, recording the average of 1000 samples per data point. After 2 min, the feedback signal is activated (inset), instantly locking the pulse delay and canceling out all the long-term drifts of the system. The compensatable drift range is thereby only limited by the employed linear stage. In this setup, a travel range of 100 mm allows for a total drift compensation of 667 ps, potentially enabling days of stable synchronization.

5.4.1.2. Spectral Analysis

In order to investigate the origin of the timing jitter and to determine the feedback bandwidth of the PSS, a spectral analysis of the measurements presented in figure 5.13 (a) is performed. Figure 5.14 shows the calculated power spectral density (PwrSD) and the integrated timing jitter with respect to the frequency. The majority of the timing jitter in the free-running case arises in a bandwidth between 0.1 Hz to 7 Hz. With activated feedback, those frequency components are completely canceled out the down to the noise-floor. The congruent PwrSD above 7 Hz (zoomed in the inset) indicates no additional introduction of timing jitter by the activated feedback towards higher frequencies and thus a well chosen control parameter set.

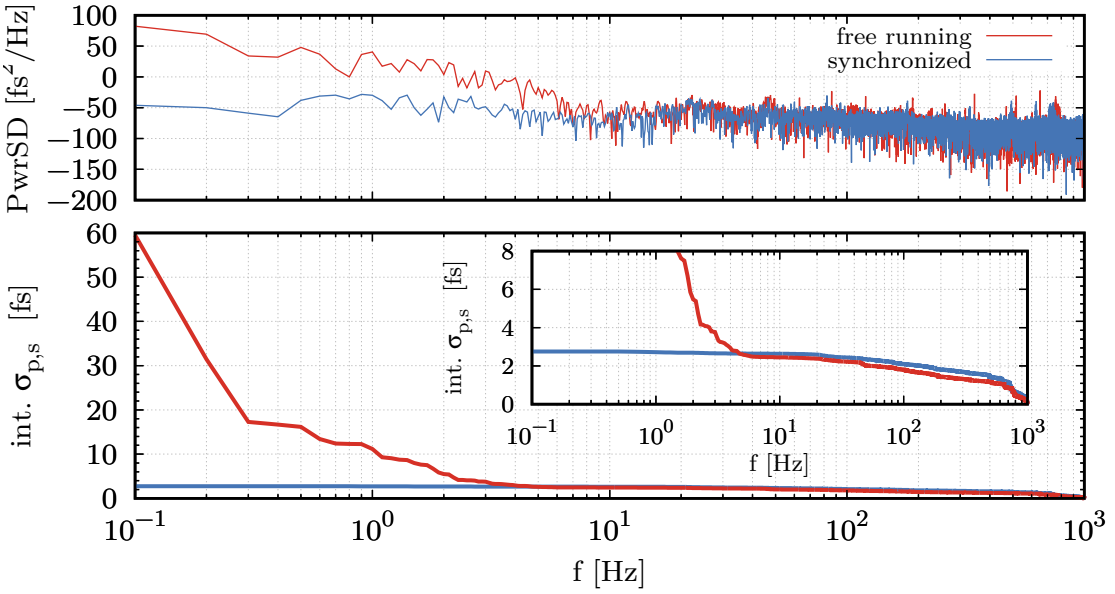

Figure 5.14.: Power spectral density and integrated timing jitter $\sigma_{p,s}$, measured in PSS_α in the free running and the synchronized case.

5.4.1.3. Out-of-loop Performance

The out-of-loop timing jitter is characterized in the context of the mJ-OPCPA, where PSS_β is used to measure and synchronize the relative pump-seed delay. At the position of the first OPA stage, which is about 2 m further away from PSS_β, $\mathrm{PSS}_{\beta,2}$ is implemented to determine the out-of-loop timing jitter. Both systems have been previously calibrated according to table 5.1. Figure 5.15 shows the in-loop (top, blue) and out-of-loop measurement (red, bottom) over 10 s (6000 samples) and the corresponding histogram of the

data. In-loop, the remaining timing jitter amounts to $\sigma_{p,s,IL} = 8.1 \pm 0.009\,\mathrm{fs}$ rms while out-of-loop, a minor increase to $\sigma_{p,s,OOL} = 9.0 \pm 0.01\,\mathrm{fs}$ rms is measured. Slight deviations of the mean value around the setpoint $\Delta t_{p,s} = 0$ are visible in the out-of-loop measurement, which are attributed to the influence of beam pointing, elucidated hereafter. The generally higher remaining timing jitter compared to PSS_α is a result of the lower SNR due to the smaller repetition rate and the decreased temporal resolution, caused by the smaller GDD of the seed (compare table 5.1). However, $\sigma_{p,s}$ is still less than 0.7 % of the pump pulse duration and sufficiently low to guarantee stable operation.

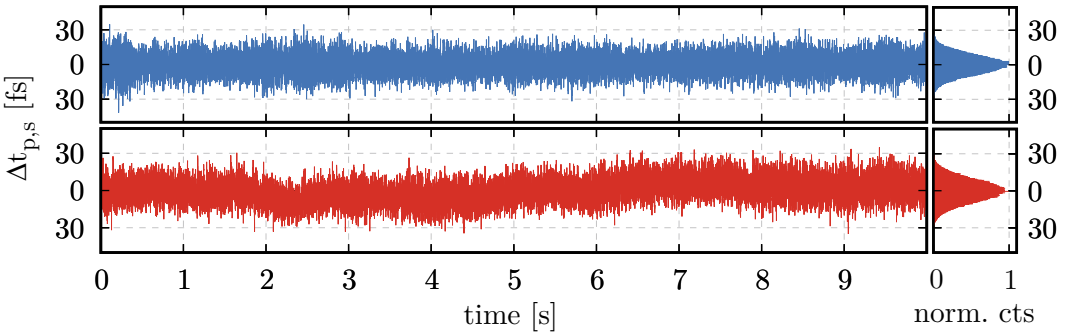

Figure 5.15.: Comparison between in-loop (top) and out-of-loop performance (bottom), measured with PSS_β and $\mathrm{PSS}_{\beta,2}$, respectively.

5.4.2. Beam Pointing Influence

It is obvious that any spatial fluctuation of the beam centroid in the horizontal plane on the PSD is interpreted as a delay shift of the system and therefore causes a measurement error. Such fluctuations are caused e.g. by beam pointing of the pump source, which alters the spatial origin of the signal and is subsequently translated to an offset in the PSD position. Because the focal spot size of the seed is ∼40 % larger than the pump in the SR-OPA (compare section 5.3.1), the pointing of the seed can be neglected here.
Figure 5.16 shows the beam pointing of the pump source in the SR-OPA crystal plane in case of PSS_β, measured over 1000 samples and before its conversion to the final platform (see section 4.9). Because the PSD is only sensitive to horizontal shifts, pointing in the vertical plane can be neglected as long as the beam still hits the detector. In the horizontal plane, the beam pointing amounts to $\sigma_h = 32.77\,\mu\mathrm{rad}$. Assuming the direct transfer of σ_h to the signal, the spatial error on the PSD due to beam pointing is estimated to be 1.64 µm, given by the focal length of the final lens of $f = 50\,\mathrm{mm}$. Because of the small angular change, the influence of the intermediate transmission grating is omitted. Multiplication of the spatial error with the calibration factor K results in a beam-pointing induced standard error of

$$1.64\,\mu\mathrm{m} \cdot K = 3.28\,\mathrm{fs}$$

which impairs the out-of-loop pump-seed delay. Since this value is far below the threshold of 1.75 % times the utilized pump pulse duration, it is irrelevant in this OPCPA system.

In cases where the beam pointing error becomes significant, its relative magnitude can be decreased by

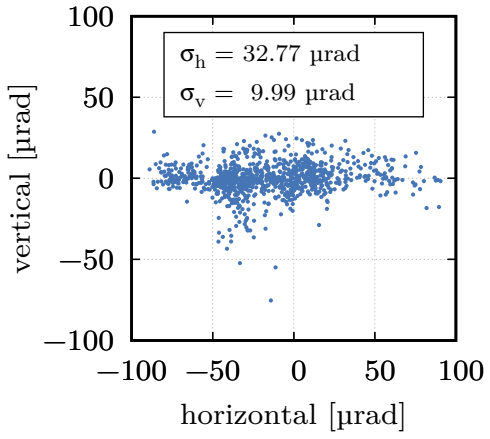

Figure 5.16.: Measured beam pointing of the pump source in the SR-OPA crystal plane at the time of the out-of-loop measurement.

1. focusing the pump with a shorter focal length, which decreases the absolute spatial offset in the SR-OPA crystal and consequently on the PSD,
2. utilizing a grating with a larger line density, which increases the sensitivity to the timing delay according to equation 5.7 while the beam pointing error remains constant,
3. further stretching of the seed pulses, which also increases the sensitivity to the timing delay at a constant beam pointing error.

5.5. Summary and Outlook

An active synchronization system has been developed which locks the relative delay between pump and seed pulses in an OPCPA with a remaining timing jitter of below 3 fs, measured in a bandwidth between 0.1 Hz and 1 kHz. Utilizing a 100 mm-long SF57 stretcher, a measurement range of ∼20 ps is realized at the same time. To the best of my knowledge, this represents the highest dynamic range in a pulse synchronization system today.

The exceptional performance is enabled by a sophisticated signal detection, based on a PSD with an SNR as high as 80 dB. Signal processing, i.e averaging and applying a 1 kHz-low-pass filter, enhances this value up to 103 dB and enables a spatial resolution limit of only 35 nm.
Because OPA is used to generate the optical error signal, a minimal seed pulse energy of only 4 pJ in combination with 10 µJ pump pulse energy is necessary. The latter can in theory be reduced below 4 µJ, as long as the intensities inside the nonlinear medium are kept constant. Therefore, an implementation in almost any OPCPA setup is possible without significantly sacrificing energy of the main amplifier, which has been a drawback of earlier systems. The system behavior can be adjusted to different demands, e.g. a higher resolution or an increased measurement range, by the adequate choice of stretcher, grating and projection lens. With an excellent long-term performance, thermal drifts are compensated over hundreds of picoseconds, enabling a stable OPCPA-performance over days.

Beam pointing has been identified to slightly impair the out-of-loop performance of the PSS and measures have been proposed to reduce its influence in a given setup. Although

not necessary here, this error can be eliminated completely by measuring the signal beam pointing in parallel with a second PSD.

A feedback bandwidth >7 Hz is determined, which is absolutely sufficient in the presented system. In general, the bandwidth is limited by the response time and mechanical resonances in the delay line. If necessary, it could therefore be further increased by using a faster piezo actuator with a resonance frequency in the kHz-regime and by additional implementation of electronic bandpass-filters to suppress occurring resonances. Adjusting the delay with help of an acousto-optic programmable dispersive filter represents another attractive option with high feedback bandwidth and the additional possibility to modulate the signal phase of the OPCPA at the same time.
To circumvent the need for electronic background rejection of the unamplified seed pulses, the direct detection of the angular dispersed idler is an attractive option in the future.

Outstanding performance paired with a high system design flexibility were the occasion to transfer the presented results into a complete product, which at this time is available at TRUMPF Scientific Lasers. The commercial PSS features a detection unit, a customizable delay line, a standalone control unit and the corresponding remote control software. An impression of the first two is given in figure 5.17.

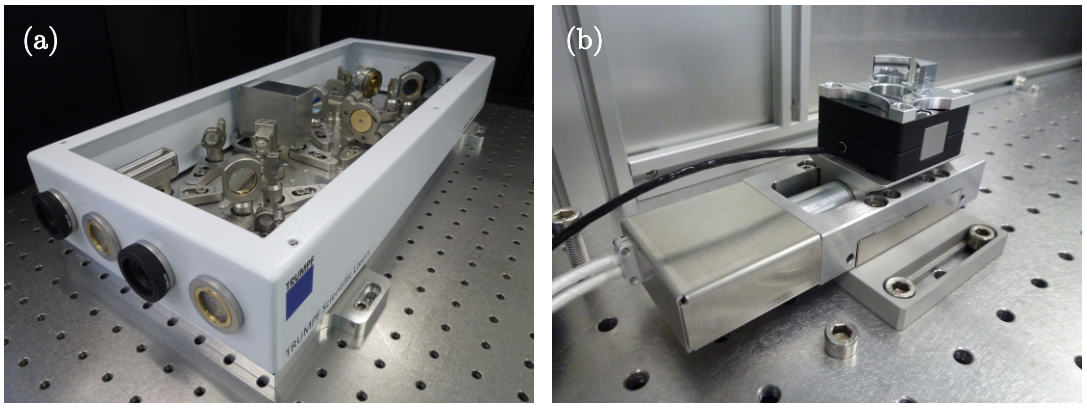

Figure 5.17.: Detection unit (a) and delay line (b) of the commercially available PSS.

6. Optical Parametric Chirped Pulse Amplifier

This chapter presents the design and implementation of a high-energy few-cycle OPCPA system, designated to drive HHG in future pump-probe experiments and to substitute the still predominant Ti:Sa-amplifiers. The paramount objective is the generation of multi-mJ pulse energies at multi-kHz repetition rates, paired with sub-3 cycle pulse duration (<8 fs at 800 nm) and a stable CEP. This parameter combination potentially enables the formation of isolated attosecond pulses with a high photon flux. The Ti:Sa-oscillator presented in chapter 3 and the Yb-based thin-disk regenerative amplifier developed in chapter 4 are utilized as seed and pump source, respectively. Pump and seed pulses are fixed in time by the PSS which has been introduced in the previous chapter 5.
As mentioned in section 4.9, the pump source was initially only realized as a laboratory setup without sealed inner housings, no temperature-stabilized breadboard and less rigid optical mounts. Although the characteristics of output power and energy were the same, the stability of the system, precisely beam pointing, pulse-to-pulse fluctuation and power fluctuation, was significantly worse. Only after the final OPCPA concept was fixed, the pump laser was converted to its ultimate platform. The stability of the early OPCPA concepts is therefore not comparable to the parameters obtained in the end and therefore omitted.

One major challenge to a stable operation is imposed by the high peak power of the pump, which is investigated in the context of this work and results in an adapted design of the parametric amplifier. The evolution towards the final setup is described in detail in the following.

6.1. General Design Considerations

6.1.1. Nonlinear Crystal Choice

The desired amplification bandwidth and the pump wavelength dictate the choice of the nonlinear crystals in question. Important material parameters to consider are the effective

nonlinear coefficient d_{eff}, the damage threshold and the GVM. In addition, the crystal needs to be transparent in the wavelength range of pump, seed and idler and manufacturable in the required dimensions. A detailed review of the most common nonlinear crystals is given in [17].

Popular OPA crystals used for amplification in the Ti:Sa-bandwidth are BBO and LBO. Both are highly transparent in the bandwidth between 515 nm (pump) and ∼2200 nm (idler) and feature broadband phase matching around 800 nm in noncollinear configuration, as shown exemplary in figure 6.1.

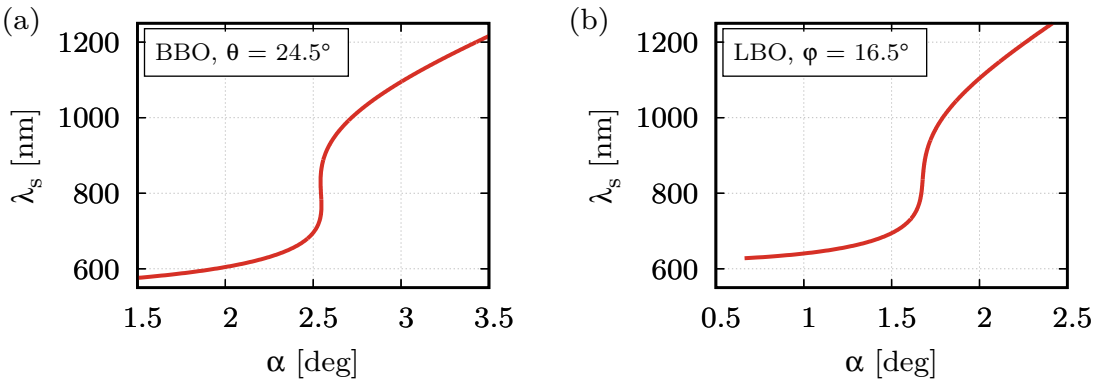

Figure 6.1.: Broadband phase matching curves of (a) BBO and (b) LBO, calculated for a pump wavelength of $\lambda_p = 515\,\text{nm}$.

While LBO exhibits a higher laser damage threshold, BBO has a broader thermal acceptance bandwidth and a more than two times higher d_{eff}. The latter results in shorter interaction lengths and thus, shorter crystals which in turn support a broader phase matching bandwidth. In addition, the larger noncollinear angle allows the separation of the involved beams after a shorter propagation distance. These are the reasons why BBO is chosen in all OPA stages throughout this work.

In case of SHG, on the other hand, LBO is favorable because of the higher damage threshold, a smaller GVD and a smaller walk-off angle. Besides, the calculated required dimensions of $15 \times 15 \times 2\,\text{mm}^3$ are easier to manufacture than those of BBO ($15 \times 15 \times 0.5\,\text{mm}^3$) and the material is less hygroscopic.

6.1.2. Dispersion Management

Efficient and broadband amplification can only take place if the ratio of pump and stretched seed pulse duration is well matched. If the seed pulse duration is short compared to the pump, the temporal overlap between the pulses is small which limits the maximum conversion efficiency. The non-overlapping part of the pump will amplify PSF and decrease the SNR. If the seed is too long, the spectral wings outside or at the edge of the pump window are not or only weakly amplified, which results in a reduction of the signal bandwidth and subsequently, in a longer pulse duration after amplification. Since efficiency and bandwidth can not be maximized at the same time, a trade off is always necessary. It depends on the application which property is prioritized.

The optimization of the temporal overlap has been adressed e.g. in [81,121]. In a detailed study presented by Moses et al. [61], the useful concept of a temporal region of significant gain t_g within the pump pulse is introduced. Because the gain G is time-dependent and follows the pump pulse intensity I_p according to $G(t) \sim \exp\left[\sqrt{I_p(t)}\right]$, t_g is defined as the time interval where $G(t) \geq G_0/e$, with peak gain G_0. For a Gaussian-shaped pump pulse with FWHM duration Δt_p, the authors find

$$t_g = \frac{\Delta t_p}{2\sqrt{\ln 2}} \sqrt{-2 \ln\left(1 - 1/\ln(4G_0)\right)}. \tag{6.1}$$

An important fact which results from this concept is the decrease of t_g with an increasing G_0. This means that in a preamplifier stage with $G_0 = 10^5$, a shorter seed pulse is required than in a power amplifier stage with $G_0 = 10^2$. Figure 6.2 (a) visualizes the situation of a Gaussian pump pulse and the corresponding region of significant gain for $G_0 = 10^2$ and a suitably stretched seed pulse. In (b), the relative width of t_g in dependence of the peak gain, according to equation 6.1 is presented. While the depicted trend is generally valid, the absolute values clearly depend on the parameter regime of the application. A chirped pulse e.g. decreases the region of significant gain due to a temporally varying wavevector-mismatch, whereas in a saturated amplifier, t_g is increased as soon as the gain saturates at the peak intensity and the wings are further amplified. For a specific OPCPA system, the optimum seed pulse duration Δt_s can thus be determined according to

$$\Delta t_s = a \cdot 2t_g, \tag{6.2}$$

where the correction factor a accounts for the experimental situation.

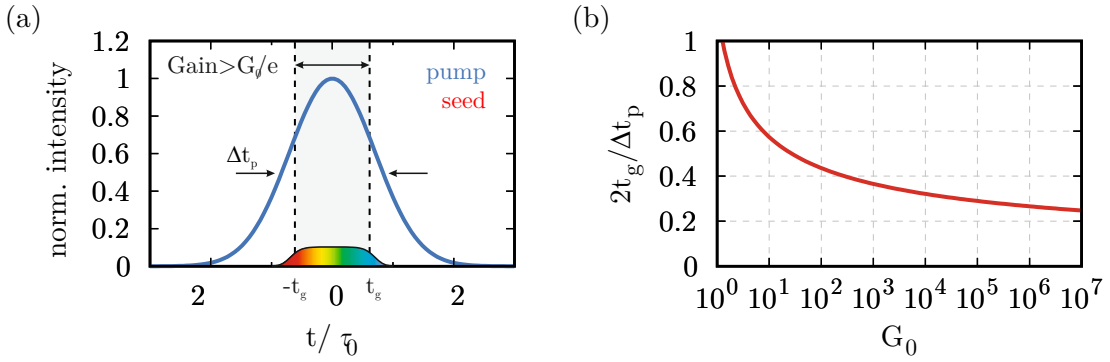

Figure 6.2.: (a) Normalized Gaussian pump pulse profile and corresponding region of significant gain for a peak gain $G_0 = 10^2$, together with a suitably stretched seed pulse. (b) Relative width of the temporal region of significant gain versus peak gain. Adapted from [61].

Based on this general rule, a positive dispersion concept has been chosen in the OPCPA design. A total of three amplification stages is envisaged, i.e. one preamplifier and two poweramplifiers, to efficiently convert the pump energy to the signal and simultaneously minimize the amount of parasitic PSF. In order to achieve a few-cycle pulse duration below 8 fs, the majority of the bandwidth needs to be preserved.
Initial seed pulse stretching is acquired in a 20 mm-long fused silica bulk in combination

with a CaF_2-wedge pair with an average material thickness of 2 mm, used for dispersion fine tuning. Those elements introduce a GDD of ∼720 fs^2 and ∼56 fs^2, respectively. The pulse is further chirped towards the poweramplification stages only by the material dispersion of the OPCPA crystals. Thus, the pulse length inherently follows the suggested trend of figure 6.2 (b). This approach prevents additional dispersion control between the amplifier stages, minimizing optical losses and system complexity.
Figure 6.3 visualizes the developed concept and the calculated seed pulse duration in the respective stages. The region of significant gain below the 1.3 ps-short pump pulse (blue) is indicated in grey for the estimated peak gain in every amplification stage. A correction factor of $a = 1.6$ is chosen to account for the experimental situation. This is justified by the simulations presented in section 6.2 and similar to [61] ($a = 1.7$). The transform-limited seed pulse is stretched by applying the spectrally dependent dispersion of the aforementioned materials, calculated by the Sellmeier equations using the software vChirp (v1.1.2.14, venteon Laser Technologies GmbH). Spectral changes during amplification are neglected. Utilizing BBO with a length of 3 mm (GDD ≈ 216 fs^2) and 2 mm (GDD ≈ 144 fs^2) in the first and the second stage respectively, the seed pulse matches well within the estimated gain region in every OPA without further efforts.
To compensate for the introduced dispersion after the amplification chain, signal recompression is intended by multiple bounces on double-chirped mirror (DCM)-pairs with negative chirp. The feasibility of this concept has now to be verified in the experiment.

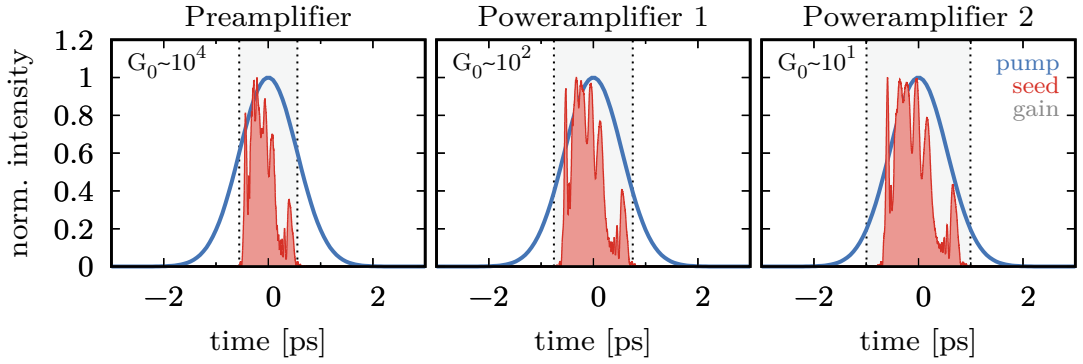

Figure 6.3.: Evolution of the temporal seed pulse shape (red) throughout the amplification stages by applying a positive dispersion concept. The pump pulse (blue) and the region of significant gain (grey) at the anticipated peak gain G_0 are indicated as comparison. The pulse is successively stretched in 20 mm fused silica, 3 mm BBO and 2 mm BBO and inherently matches the gain region in every stage.

6.2. Preamplification

The preamplification stage paves the way for the final OPCPA performance. Its purpose is to boost the sub-nJ seed pulses up to the µJ-level in order to enhance the efficiencies in the power amplifiers, which increases with a smaller ratio E_p/E_s [61], and to keep the total amount of PSF low. The generated signal bandwidth already predetermines the achievable pulse duration of the complete system and spectral features as well as parametric phase

components influence the output of all subsequent amplification stages. Generation of PSF potentially impairs the SNR of the amplified signal and should therefore be kept at a minimum. Thus, the parameters of the preamplification stage have to be chosen with great care.

6.2.1. Simulation

Prior to the experimental setup, the amplification behaviour is simulated with the Matlab-based toolbox chi2D (v8.6) [50] to identify suitable parameters for the process. The simulation parameters are adapted to the planned experimental conditions: A 3 mm-short BBO crystal at an angle $\theta = 24.39°$ is used as the interaction medium. The effective nonlinear index d_{eff} is set to $2\,\text{pm}\,\text{V}^{-1}$. The stretched seed pulse is defined as ordinary polarized with a $1/\text{e}^2$-beam radius of $w_s = 150\,\mu\text{m}$. Due to optical losses in the beam path, the energy is reduced to $E_{\text{seed}} = 0.5\,\text{nJ}$. The seed spectrum is extracted from the measurement presented in figure 3.3, while the spectral phase, induced by 20 mm fused silica and 2 mm CaF_2, is calculated with vChirp. An extraordinary polarized Gaussian-shaped pump pulse in space and time is assumed with a pulse duration $\tau_p = 1.3\,\text{ps}$ and a radius $w_p = 140\,\mu\text{m}$. Temporal and spatial overlap are optimized in terms of output energy and bandwidth at relative pump-seed offsets $\Delta t_{p,s} = 0\,\text{fs}$ and $\Delta x_{p,s} = 88\,\mu\text{m}$ with a noncollinear angle of $\alpha = 2.44°$. A small angular offset in θ and α from the *magic angle* is set throughout all OPA stages in this thesis to enhance the amplification bandwidth, taking into account a minor associated phase mismatch [81]. Because the beam diameters are small, PVWC geometry is chosen to increase the interaction length and obtain a less distorted beam profile [108]. Figure 6.4 shows the simulated results for different pump intensities I_p, set by varying the pump energy E_p.

Three amplification regimes can be distinguished from the simulation, indicated in the figure. In regime A, below $I_p = 50\,\text{GW/cm}^2$, an exponential increase of E_s, gain and efficiency η is observed. Simultaneously, the amplified bandwidth and consequently the FTL are decreased due the suppression of the spectral wings. In this regime, no pump depletion occurs and the process is not yet saturated. Between $50\,\text{GW/cm}^2$ and $100\,\text{GW/cm}^2$ (regime B), the conversion starts to saturate in the peak gain region, where backconversion starts to take effect. Parasitic SHG around 880 nm sets in and creates a characteristic dip in the spectrum. At the same time, the spectrum is broadened as the spectral wings are further amplified. E_s, gain and η increase linearly and the FTL decreases. At more than $100\,\text{GW/cm}^2$ (regime C), η and gain continue to grow only slowly and E_s approximately follows E_p. Only a small remaining enhancement in bandwidth is observed with increasing I_p which contributes to the small growth of η. In the saturated part of the spectrum, forth- and backconversion between seed and pump are in equilibrium and cause significant GDD oscillations as well as intensity modulations in the spectrum. In regime A, the introduced GDD oscillations are still negligible, but as soon as backconversion effects set in, higher-order dispersion arises in particular in the regions of imperfect phase matching and around the parasitic SHG, which might spoil the pulse compression later on. This needs to be checked in each individual case.

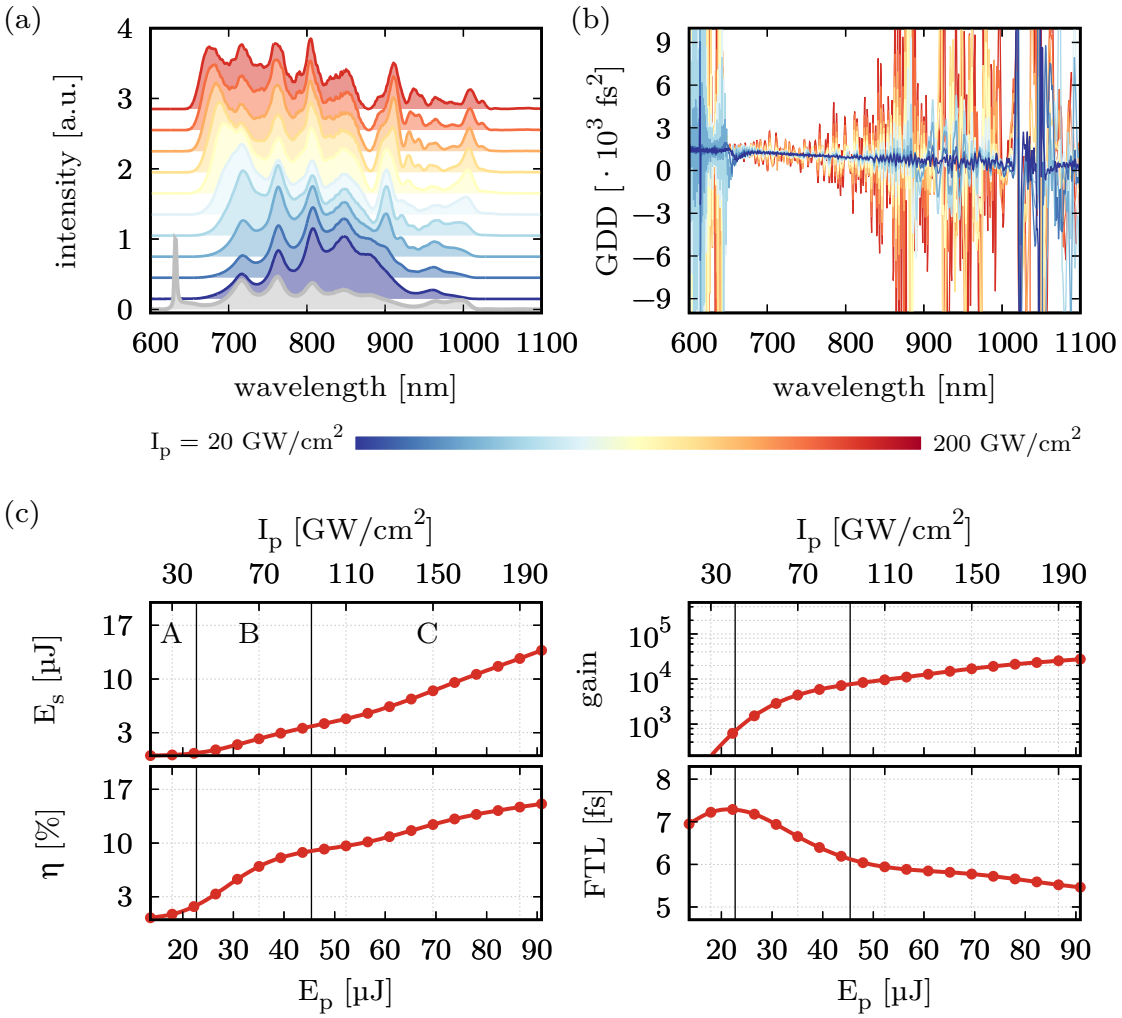

Figure 6.4.: Simulated preamplification dynamics with increasing pump intensity I_p. (a) Spectral evolution of the signal. The intensity is increased in steps of 20 GW/cm^2 between each displayed spectrum. (b) GDD introduced by the amplification process at different I_p. (c) Evolution of signal pulse energy E_s, gain, efficiency η and signal FTL.

6.2.1.1. Parametric Superfluorescence

Similar to ASE in conventional laser media, fluorescence photons, which are generated from vacuum fluctuations of the electromagnetic field, are further amplified by the pump beam in the gain medium and form the so-called PSF [40]. The amount of PSF at different pump intensities is estimated in the simulation by adding white noise with a random phase to each element in the space-time domain. Because the direct extraction of the PSF by simply comparing the amplified signal energy with and without noise is not possible due to the limited precision of the saved results, it is accessed via the intensity of the characteristic PSF-cone, similar to [99]. This cone is phase matched at positive and negative angles $\alpha \approx \pm 2.44°$ according to the phase matching curve and covers a wavelength range from about 600 nm to 930 nm, appearing as a red crescent moon in the experiment. As PVWC geometry is used, the energy of the cone is evaluated at $\alpha = -2.44°$, away from the signal. This approach allows an insight into the general behavior of the PSF, but no statement

about its absolute energy. All values have therefore been normalized for comparison. The simulation results are shown in figure 6.5.

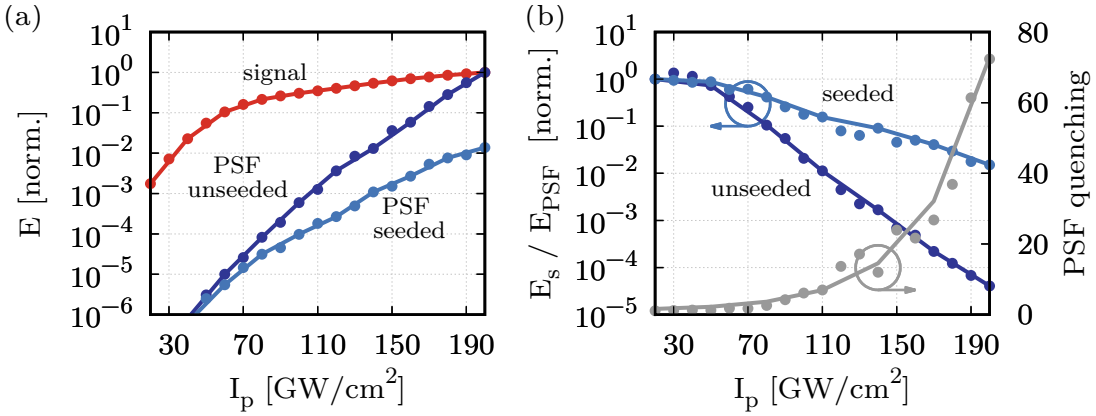

Figure 6.5.: (a) Normalized energy evolution of PSF at different pump intensities in the seeded and unseeded case. To identify the OPA operation regime, the signal energy E_s is plotted in addition. (b) Pulse contrast E_s/E_{PSF} in the presence of the seed compared to the unseeded case and PSF quenching.

In (a), the PSF evolution in presence and absence of the seed beam is depicted. The amplified signal is indicated as comparison. In the unseeded case, the PSF energy is only dependent on the small signal gain. An exponential increase towards higher I_p is observed, which resembles the situation in the previously defined OPA regime A. In the seeded case, the PSF build-up is significantly attenuated above $I_p = 70\,\mathrm{GW/cm^2}$, where the OPA process starts to saturate. Due to the increasingly depleted pump in this regime, the PSF gain is lowered towards higher pump intensities. Figure 6.5 (b) illustrates the associated PSF gain quenching factor $E_{\mathrm{PSF,unseeded}}/E_{\mathrm{PSF,seeded}}$, which increases exponentially with I_p. In addition, the influence of PSF on the pulse contrast E_s/E_{PSF} is shown. At low I_p, both signal and PSF are amplified with equal gain and the pulse contrast is maintained. In the saturated regime, a more steeply rising PSF deteriorates the contrast as expected. Thanks to gain quenching, the presence of the seed significantly improves the situation and hampers the pulse contrast deterioration by up to multiple orders of magnitude. Based on the simulation, the PSF energy and the pulse contrast in the preamplification stage can now be estimated by blocking the seed, measuring the PSF energy in the unseeded case and applying the gain quenching factor at the respective setpoint.

A further reduction of the PSF can be potentially achieved by increasing the seed energy E_{seed}, which is shown in figure 6.6. In this simulation, the pump intensity is kept constant while E_{seed} is sweeped from 10 pJ to 1 µJ.
As depicted in (a), the PSF is decreased between one and three orders of magnitude at low and high I_p, respectively. A higher E_{seed} results in an earlier onset of pump depletion and saturation, as can be seen in (b), and consequently leads to higher PSF quenching (compare figure 6.5). At the same time, the signal pulse energy increases towards a higher seed level, which in total results in a significantly increased contrast.
This is the reason why the preamplification stage with its high gain and low seed level primarily defines the final pulse contrast. In order to keep the PSF small and the pulse

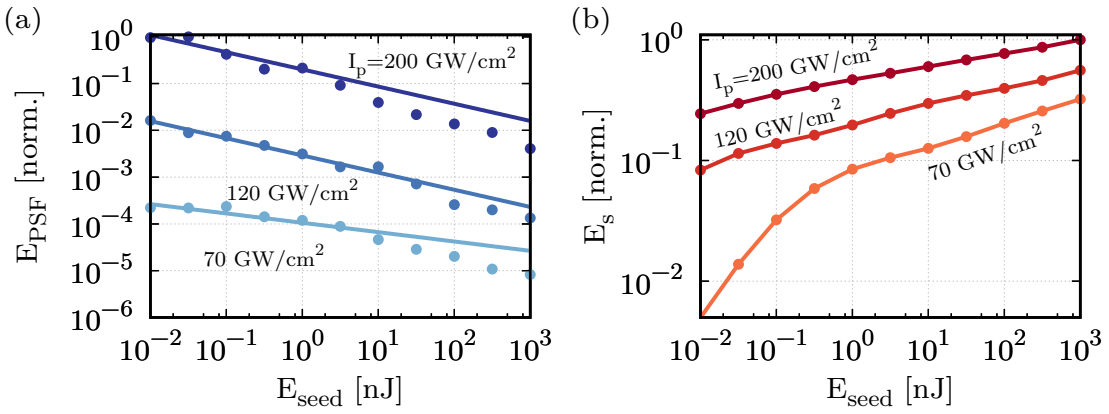

Figure 6.6.: (a) Simulated decrease of generated PSF with increasing seed energy E_{seed} at constant pump intensities of I_p = 70, 120 and 200 GW/cm^2 (31.8, 54.5 and 90.9 µJ), normalized to the latter one. The fitted line is a guide to the eye. (b) Simultaneous increase of the signal energy E_s, normalized to I_p = 200 GW/cm^2.

contrast high, heavy saturation should thus be avoided here. In the poweramplifiers on the other hand, the pulse contrast is much less affected due to a low gain and high PSF quenching in the presence of the strong seed.

Based on the simulated data, a appropriate pump intensity of I_p = 120 GW/cm^2 is identified for the preamplifier, which represents a good compromise between efficiency, signal energy and amplified bandwidth on the one hand and pulse contrast deterioration and GDD oscillations on the other hand. The simulated pulse compression at this setpoint is presented in figure 6.7. Using the designed GDD of the planned DCM-pairs and 3.7 mm of CaF_2 allows an adequate compensation of the dispersion, as demonstrated in (a). The pulse is compressed down to a FWHM of 6.4 fs (1.1×FTL, figure 6.7 (b)), which verifies the suitability of the chosen pump intensity.

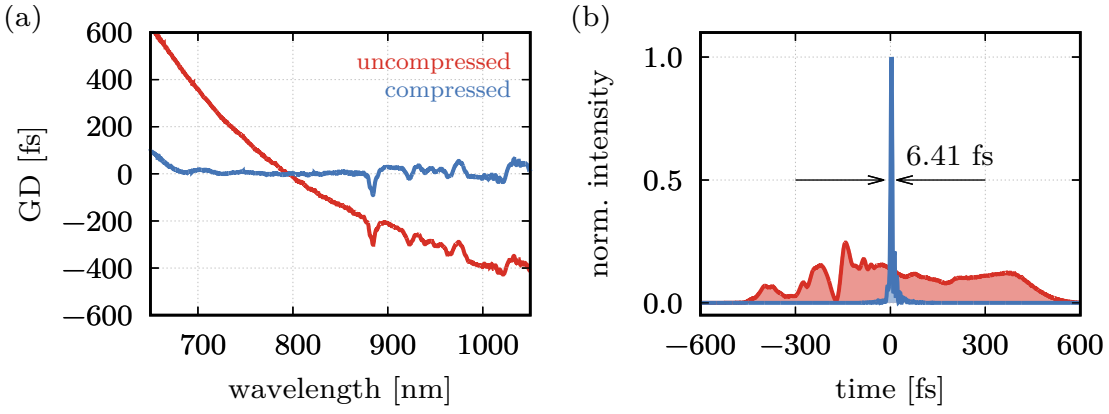

Figure 6.7.: Simulated compression of the preamplified pulse at I_p = 120 GW/cm^2. (a) GD before (red) and after compression (blue) and (b) temporal pulse shape before (red) and after compression (blue). The intensity of the uncompressed pulse is scaled by a factor of 10 for visibility.

6.2.1.2. Seed Chirp

In order to identify a proper seed chirp at $I_p = 120\,\mathrm{GW/cm^2}$, the simulation is repeated with seed GDD values between $300\,\mathrm{fs^2}$ to $1800\,\mathrm{fs^2}$. The evolution of signal pulse energy E_s, FTL and peak power $P_p = E_s/\mathrm{FTL}$ are depicted in figure 6.8.

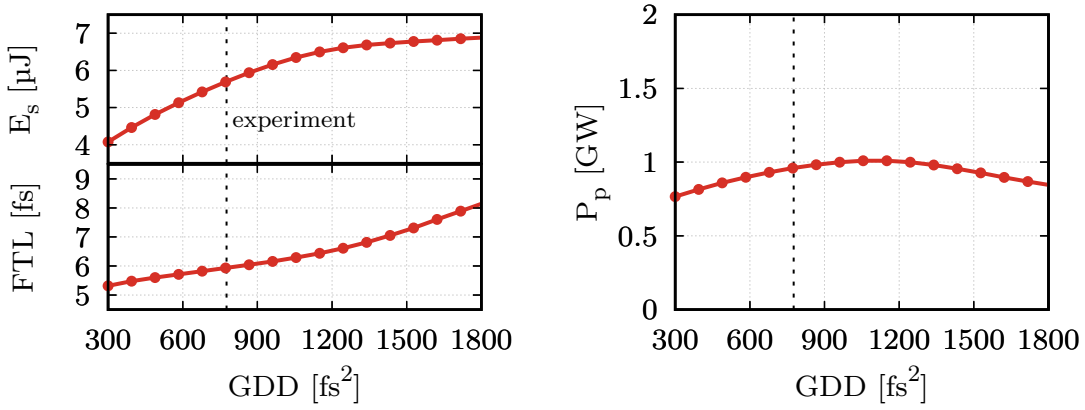

Figure 6.8.: Simulated signal energy E_s, FTL and peak power P_p after amplification of increasingly chirped seed pulses.

Longer seed pulses increase the conversion efficiency, but cause a loss of spectral bandwidth which leads to a reduction of the FTL. The highest peak power is achieved around $\sim$1100 $\mathrm{fs^2}$, which corresponds to the transmission of a $\sim$30 mm-long fused silica bulk. However, the focus in the preamplification stage is more on the FTL than on the signal energy, because the amplified bandwidth can be no further enhanced in the low-gain poweramplifiers, while the energy certainly can. With the hitherto chosen GDD of $\sim$776 $\mathrm{fs^2}$, indicated by the dashed line, a 10 %-shorter FTL below 6 fs is achieved by sacrificing $\sim$5 % in peak power as compared to the optimum. This compromise is justified by the goal of achieving sub-8 fs pulses after compression.

6.2.2. Experiment

To verify the simulation results, different pump intensities I_p are tested in the preamplification stage by increasing E_p at a constant w_p of 125 µm. The BBO crystal with $L = 3\,\mathrm{mm}$ and an aperture of $5 \times 5\,\mathrm{mm^2}$ is mounted in a temperature-controlled copper frame, stabilized to 40 °C to ensure long-term phase matching.
Figure 6.9 shows the spectral evolution of the signal towards higher I_p, along with the most important parameters. The simulated data is indicated in grey as comparison. The measured characteristics closely resemble those of the simulation up to $120\,\mathrm{GW/cm^2}$, which verifies the simulated results. Only the FTL is a bit higher in the experiment, but follows the same trend. At $170\,\mathrm{GW/cm^2}$, the simulation slightly overestimates the pulse energy, caused by the assumption of a fixed beam radius in the vertical dimensions instead of a dynamic one to speed up the calculations. The onset of saturation is visible at $70\,\mathrm{GW/cm^2}$, indicated by the spectral dip from the parasitic signal SHG around 880 nm. With increasing I_p, the spectral wings are enhanced and a higher efficiency as well as a shorter FTL is

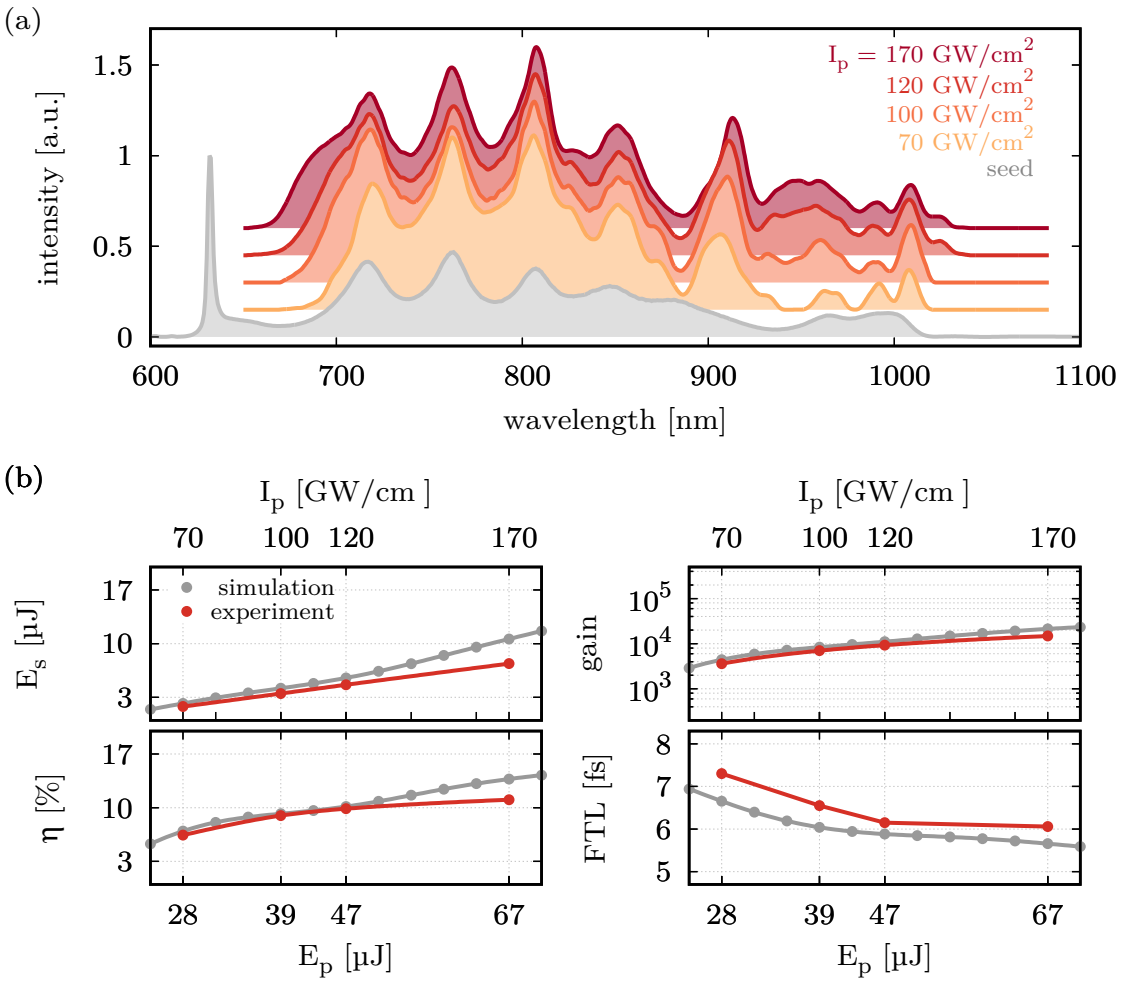

Figure 6.9.: Preamplification dynamics with increasing pump intensity I_p. (a) Spectral evolution of the signal. (b) Evolution of signal pulse energy E_s, gain, efficiency η and signal FTL. The simulated results are indicated as reference in grey.

obtained. At 170 GW/cm^2, a further increase of E_s is measured, but the process is heavily saturated and no more significant enhancement of the spectral bandwidth is observed. However, according to the simulation, pulse contrast and dispersion are further impaired and make this setpoint unattractive.

At $I_p = 120\,\mathrm{GW/cm^2}$, a signal pulse energy of $E_s = 4.6\,\mu\mathrm{J}$, a gain $>6 \times 10^3$, a conversion efficiency of 9.8 % and a FTL pulse duration of 6.15 fs are achieved. No measurable PSF is detected by the utilized powermeter (Gentec XLP12-3S-H2, Noise Equivalent Power (NEP) = 0.5 μW) when the seed is blocked, which prevents the estimation of PSF energy and pulse contrast according to section 6.2.1. A worst case limit is calculated in the following: Within a 5 % measurement uncertainty, the PSF energy in the unseeded case is below

$$\frac{\mathrm{NEP}}{0.05 \cdot f_{\mathrm{rep}}} = \frac{0.5\,\mu\mathrm{W}}{0.05 \cdot 6\,\mathrm{kHz}} = 1.67\,\mathrm{nJ}. \tag{6.3}$$

Taking into account a PSF gain quenching factor of 10 according to figure 6.5 (b), a pulse contrast E_s/E_{PSF} better than 2.7×10^4 is estimated.

With simulation and experiment in accordance, $I_p = 120\,\mathrm{GW/cm^2}$ is considered a well

suited operating point for the preamplification stage, which is used in all OPCPA concepts presented throughout this thesis.

6.3. Challenges at High Peak Powers

At the output of the regenerative amplifier, peak powers of $P_p > 20\,\mathrm{GW}$ are obtained. This is more than five times the critical peak power in air at $\lambda = 1030\,\mathrm{nm}$, $P_{\mathrm{cr,air}} \approx 4\,\mathrm{GW}$ (see section 2.3.1 and [14]). Consequently, the beam is subject to higher order nonlinear effects during propagation and runs the risk of a catastrophic collapse.

In order to assess the influence of the nonlinear effects, a numerical simulation is performed. The evolution of the linearly polarized electric field according to the nonlinear Schrödinger equation is numerically integrated along z in the presence of linear (dispersion and diffraction) and nonlinear effects (Kerr effect, Raman scattering, multiphoton ionization and defocusing) [98]. The material parameters for air are taken from [19]. A nonlinear refractive index of $n_{2,\mathrm{air}} = 4 \times 10^{-23}\,\mathrm{m^2/W}$ is assumed.
Figure 6.10 depicts the simulated propagation of a collimated Gaussian beam with a $1/e^2$-radius of $w = 3\,\mathrm{mm}$, $\tau = 1.3\,\mathrm{ps}$ and $E = 15\,\mathrm{mJ}$ at $\lambda = 1030\,\mathrm{nm}$, representing a peak power of $P_p \approx 2.8 \times P_{\mathrm{cr,air}}$. The parameters were chosen to resemble the experimental situation in the SHG 3 arm of the final OPCPA setup, presented in section 6.6.

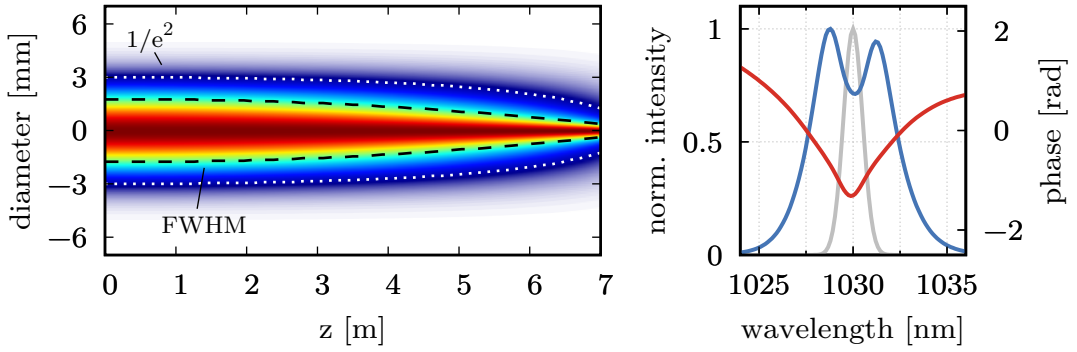

Figure 6.10.: Simulated beam propagation along z of a collimated beam with $w = 3\,\mathrm{mm}$, $\tau = 1.3\,\mathrm{ps}$ and $E = 15\,\mathrm{mJ}$ at $\lambda = 1030\,\mathrm{nm}$. Left: spatial evolution. Right: initial on-axis spectrum (grey) and on-axis spectrum and phase at $z = 7\,\mathrm{m}$ (blue and red). The spectra are normalized individually.

Kerr lensing causes the beam profile to narrow already after ∼2 m propagation. With increasing distance, the on-axis intensity rises and again reinforces the Kerr effect, leading to a self-enhancing process. After 7 m, the beam is close to a catastrophic collapse and the on-axis intensity is increased by almost five times. The inevitable consequence of this scenario are severe damages to optical elements in the beam path. The effect is accompanied by SPM, which is evident from the comparison of the spectra before and after propagation in the right part of figure 6.10. Compared to the initial spectrum (grey), the bandwidth is increased by a factor of four (blue), with a corresponding spectral phase imprinted on the pulse. For the given parameters, the onset of nonlinear effects is observed already at pulse energies of $E < 2\,\mathrm{mJ}$, or at peak powers $P_p < 0.4 \times P_{\mathrm{cr,air}}$, far below the critical peak power in air.

A small attenuation of the Kerr effect can be achieved by changing the beam polarization from linear to circular [88]. This theoretically reduces the B-integral by 1/3. However, at least two quarter-waveplates are necessary to rotate the polarization forth and back again. The waveplates introduce a Kerr effect themselves, which is about three orders of magnitude higher than in air due to the higher n_2 of the substrates. Even with sub-mm substrate thickness, the advantage of this approach is thus voided.
The ultimate option to lower the nonlinear effects is a change of the atmosphere towards lower n_2, e.g. replacing air with Helium or even with vacuum. Apart from the great mechanical effort and additional costs, this approach has two other significant drawbacks: First, the usability is considerably worse, because direct access to optical elements for maintenance and alignment is restricted by the enclosed housing. Once the housing is opened, it takes some time for the atmosphere to recover, in which system operation is prevented. Second, a poorer heat transfer from optical and optomechanical elements to the atmosphere increases thermal drifts and impairs the long-term stability.

As both options are undesired, the beam transport must be managed by taking the nonlinear effects into account. To that end, the propagation of a slightly divergent beam is investigated, intended to partially counteract the Kerr lens and prevent catastrophic beam collapse. The simulation results with a divergence of $\theta = 0.3\,\mathrm{mrad}$ and otherwise identical parameters as in the collimated case of figure 6.10 are presented in figure 6.11.

The spatial beam evolution on the left indicates that with a divergent beam, a beam collapse can be avoided over the given distance. Moreover, if the divergence is chosen appropriately, a quasi-collimated beam center develops and is maintained over a distance of several meters, which is indicated by the parallel course of the simulated beam FWHM to the FWHM of a collimated beam at low energy. In this regime, the divergence counterbalances the Kerr lens. The outer parts of the beam, which are less affected by the Kerr lens due to the lower local intensity, continue to diverge. In case of further propagation, the beam will continue to narrow down as in the collimated case and finally collapse after all. With increasing influence of the Kerr lens, the amount of energy contained in the intense FWHM area E_{FWHM} decreases along z and is virtually drained into the outer area. Nonlinear effects still influence the spatial, temporal and spectral properties of the beam, although much less than in the collimated case. This is illustrated on the right side of figure 6.11. The graphs are all normalized to the initial beam, indicated in grey. In the spatial domain, a slight narrowing of the beam profile is observed in the center, while the outer area is increased according to the divergence. Catastrophic rise of the on-axis intensity is prevented, the intensity is even decreased due to the larger beam size. The temporal pulse shape remains approximately constant, because the spectral broadening due to SPM, which theoretically decreases the FTL, is accompanied by a nonlinear phase which chirps the pulse. A decrease in intensity is noticed in both domains which is directly coupled to the decline of on-axis intensity in the spatial domain. Spectrally, the energy is additionally distributed over the broadened bandwidth, which lowers the peak intensity further.

In conclusion, introducing a divergence to the beam allows operating the nonlinear stages of

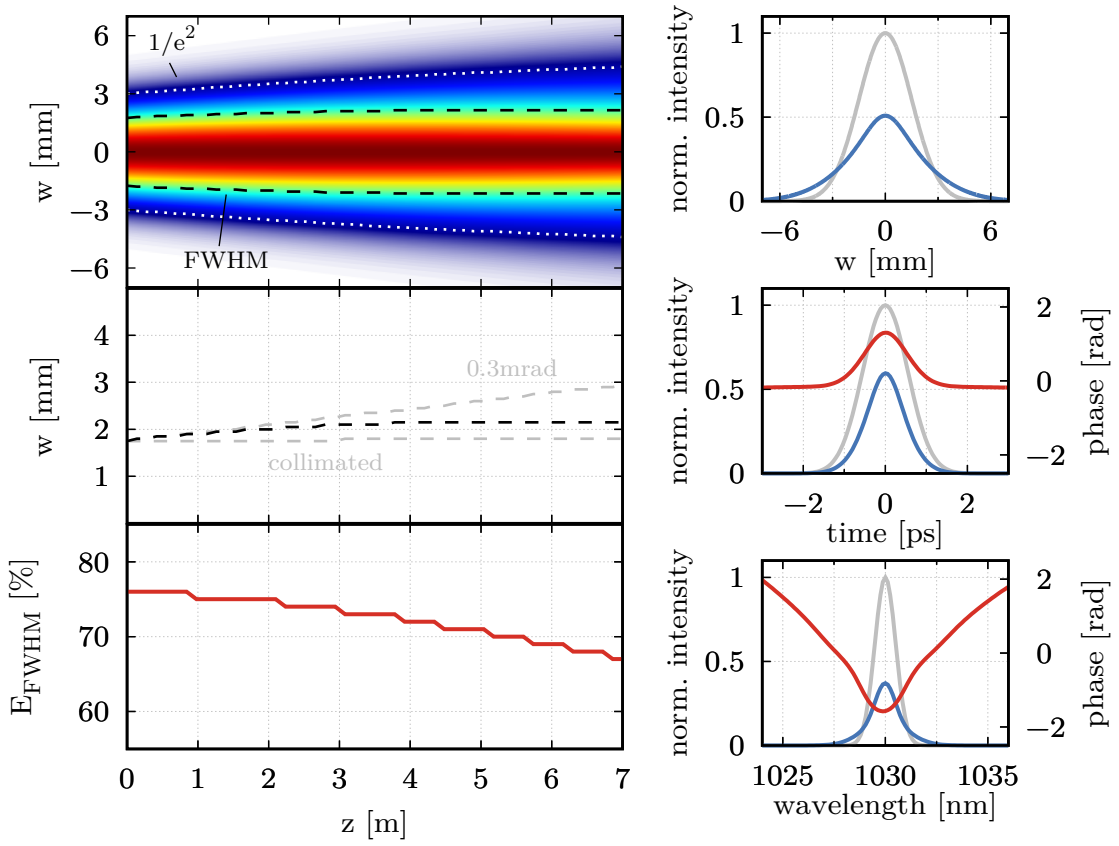

Figure 6.11.: Simulated beam propagation of a divergent beam with $\theta = 0.3\,\mathrm{mrad}$, $w = 3\,\mathrm{mm}$, $\tau = 1.3\,\mathrm{ps}$ and $E = 15\,\mathrm{mJ}$ at $\lambda = 1030\,\mathrm{nm}$. Left, top: spatial evolution. Left, center: spatial FWHM evolution (black) with the evolution of the collimated and divergent beam FWHM at low energy indicated as reference (grey). Left, bottom: Relative energy content E_{FWHM} in the FWHM area of the beam versus propagation distance. Right, top: initial spatial beam cross-section (grey) and at $z = 7\,\mathrm{m}$ (blue). Right, center: initial on-axis temporal pulse shape (grey) and on-axis temporal pulse shape and phase at $z = 7\,\mathrm{m}$ (blue and red). Right, bottom: initial on-axis spectrum (grey) and on-axis spectrum and phase at $z = 7\,\mathrm{m}$ (blue and red). The spectra are normalized to the initial ones.

the OPCPA safely, but a complete suppression of nonlinear effects can not be accomplished with this approach. It is thus expected that the energy drain from the intense center, paired with the onset of nonlinear beam distortions in the spatial, spectral and temporal domain, will impair the conversion efficiency. This is proven experimentally in section 6.6.2.

In the following sections, three different OPCPA concepts are presented, which have (at least partially) been implemented experimentally. The emerging drawbacks of each concept are identified and eluded in the next design iteration. Thus, the complete evolution towards the final system setup is depicted.

6.4. Concept A: Pump Recycling

This concept aims for a high pump-to-signal conversion efficiency by reusing the pump pulse after the second OPCPA stage for the final poweramplifier [27,89]. Because the high power beam propagates a rather long distance not only through air, but also through one nonlinear crystal, strong beam distortions due to nonlinear effects as investigated in the previous section 6.3 are expected. With pump recycling, ultrabroadband amplification of sub-10 fs pulses in three amplification stages utilizing BBO has been achieved with up to 25 % overall efficiency [27] in a setup similar to this concept.

6.4.1. Experimental Setup

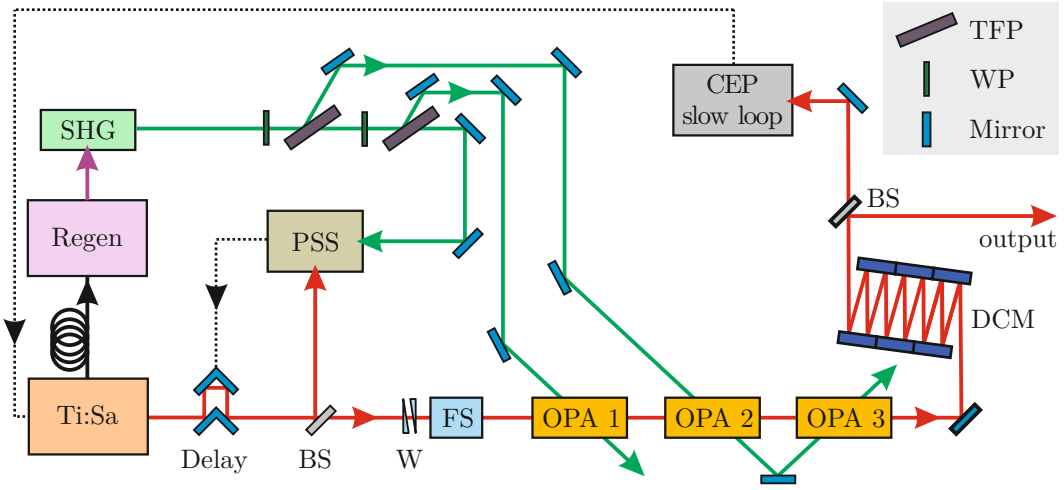

Figure 6.12.: Schematic setup of OPCPA concept B. Ti:Sa: Titanium-sappphire oscillator, Regen: regenerative amplifier, SHG: second-harmonic generation, PSS: pump-seed synchronization, BS: beam splitter, W: wedge pair, FS: fused silica stretcher, OPA: optical parametric amplifier, DCM: double-chirped mirror compressor, TFP: thin-film polarizer, WP: waveplate.

Figure 6.12 outlines the envisaged schematic setup of this concept. A single SHG stage is employed to convert the fundamental beam to 515 nm. A small fraction of the pump ($E \approx 60\,\mu J$) is separated from the main beam at the first TFP, designated to the preamplifier and the PSS. The remaining energy is reflected towards the first poweramplifier, OPA 2, and used a second time in the final poweramplifier, OPA 3.

The broadband seed pulses from the Ti:Sa-oscillator first pass the PSS delay line and the associated beam splitter (see chapter 5) and are subsequently stretched in a CaF_2-wedge pair and a 20 mm-short fused silica bulk. After amplification in the three OPA stages, pulse compression is planned in a DCM compressor. The majority of the compressed beam is directed to the output via a beam splitter with 99 % reflectivity. The transmitted 1 % of pulse energy is used in an f-to-2f interferometer to detect and stabilize slow CEP fluctuations via a feedback loop to the intracavity wedges of the oscillator.

6.4.2. Experimental Results

In accordance to section 4.10, a SHG conversion efficiency of 63 % results in 104 W converted output power, corresponding to 17.3 mJ pulse energy at 515 nm. After separating

fundamental and frequency-doubled beam by a a dichroic beamsplitter, the beam is magnified to $w \approx 4.5\,\mathrm{mm}$ in a detuned telescope, set up to induce a beam divergence of 0.18 mrad in order to counteract nonlinear effects during propagation in air. A larger beam size or increased divergence is hindered by beam clipping at the utilized optics having a diameter of 25.4 mm.

Strong Kerr lensing affecting the pump is visible already after short propagation distances in the high-energy arm of the setup. The central part of the beam profile at low energy and at $E_{515} = 10\,\mathrm{mJ}$ are shown in figure 6.13, measured at a distance $d = 2.6\,\mathrm{m}$ from the SHG stage. The beam is attenuated at the first TFP after the SHG stage. Beam clipping is already indicated by vertical fringes in the presented beam profile.

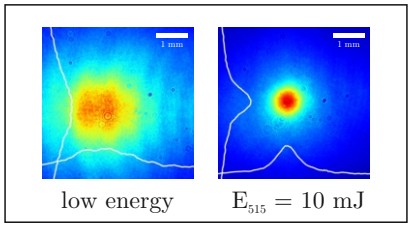

Figure 6.13.: Frequency doubled pump beam profile at (a) low energy and (b) 10 mJ (60 W), measured after 2.6 m propagation from the SHG stage.

Even at moderate energy levels, the Kerr lens leads to a contraction of the beam in the high-intense center by more than 90 %, measured at FWHM, which ultimately results in damages to the optical elements. A larger beam divergence could potentially improve the situation but requires larger optics which were not available at that time.

6.4.3. Summary

Pronounced nonlinear effects in air prevent the implementation of this concept. The usable pulse energy is limited to ∼10 mJ at 515 nm, while at higher energies, optical damages caused by a catastrophic beam collapse can not be avoided.

6.5. Concept B: Individual Pumping

6.5.1. Experimental Setup

To mitigate the influence of Kerr lensing, the pump recycling concept is rejected and the setup is changed according to figure 6.14.
A single SHG stage is maintained to keep the setup simple and the material input low. To compensate for slow beam drifts of the pump (compare section 4.9), a beam stabilization (Guide Star II, Newport Corporation, not indicated in the figure) is installed after the regenerative amplifier. After the SHG stage, the frequency-doubled beam is magnified to $w \approx 4.5\,\mathrm{mm}$ and immediately split up into four arms by a combination of half-waveplates and TFPs in order to reduce the peak power in every path. Additionally, the pump energy at 515 nm is restricted to 14 mJ by attenuating the fundamental energy to 23 mJ right after the cavity and before the compressor of the regenerative amplifier. Energies

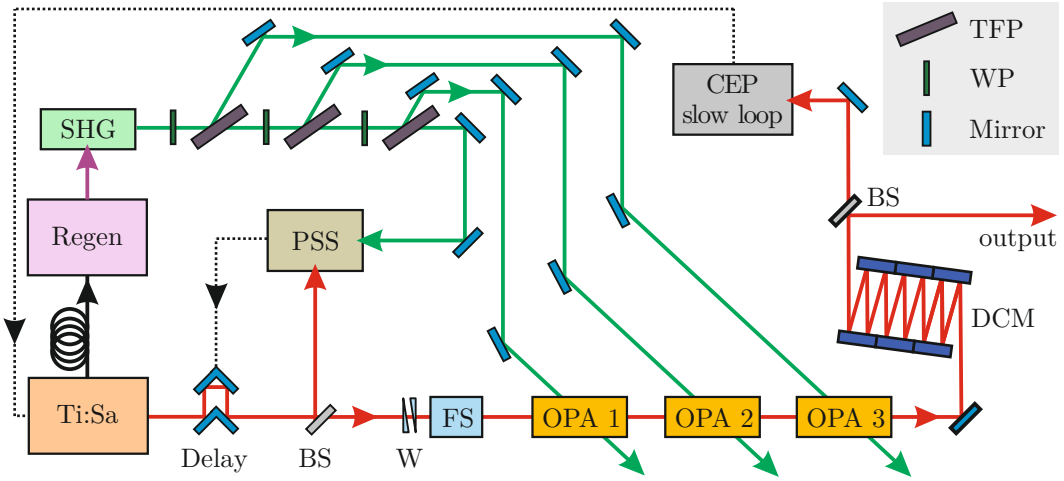

Figure 6.14.: Schematic setup of OPCPA concept B. Ti:Sa: Titanium-sappphire oscillator, Regen: regenerative amplifier, SHG: second-harmonic generation, PSS: pump-seed synchronization, BS: beam splitter, W: wedge pair, FS: fused silica stretcher, OPA: optical parametric amplifier, DCM: double-chirped mirror compressor, TFP: thin-film polarizer, WP: waveplate.

of 8.5 mJ, 5.5 mJ, 47 µJ and 10 µJ are directed towards the poweramplifiers OPA 3 and OPA 2, the preamplifier OPA 1 and the PSS, respectively. The split ratio between the poweramplifiers has been chosen to approximately balance the B-Integral in both arms. The seed beam path is set up similar as in the previous concept (section 6.4). After passing the PSS delay stage and beam splitter, the pulses are stretched and preamplified to 4.6 µJ in OPA 1 according to section 6.2. In every stage, the seed beam size is chosen to be about 10 % larger than the pump in order to optimize the spatial overlap of the interacting beams. Additionally, a manual delay stage is integrated in the seed arm in front of each OPA (not shown in figure 6.14) which allows a precise adjustment of the temporal overlap between the pulses.

6.5.2. Parametric Amplification

Table 6.1 summarizes the basic parameters of every OPA stage. To match the arrival times

Table 6.1.: Experimental parameters in the three OPA stages.

	E_{seed} [mJ]	E_{pump} [mJ]	E_{signal} [mJ]	η [%]	L [mm]	Geom.
OPA 1	5×10^{-7}	0.05	4.6×10^{-3}	9.8	3.0	PVWC
OPA 2	3.7×10^{-3}	5.5	0.6	10.9	3.0	PVWC
OPA 3	0.54	8.50	2.4	21.9	2.0	PVWC

between pump and seed pulses, the pump beams of OPA 2 and OPA 3 have to propagate ∼4 m and ∼6.5 m, respectively, to compensate for the previous seed beam path. A telescope in front of every stage reduces the beam size to obtain intensities of ∼50 GW/cm^2 in OPA 2 and ∼80 GW/cm^2 in OPA 3. To check the influence of Kerr lensing, the corresponding beam profiles at low and full energy according to table 6.1 are measured in the crystal plane. Figure 6.15 depicts the results.
The bulge in the horizontal plane is the result of a slight misalignment of the regenerative

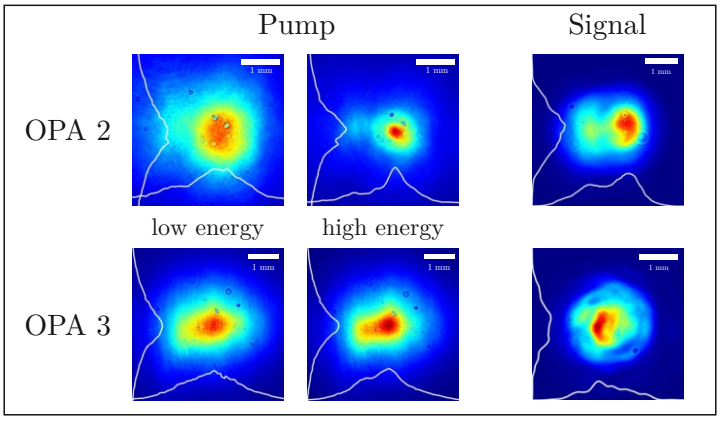

Figure 6.15.: Pump and signal beam profiles of the poweramplification stages. The pump beam profiles are measured in the crystal plane at low energy and full energy according to table 6.1. The signal beam profiles are measured ∼1 m after the respective amplifier.

amplifier cavity which occurred in the initially used laboratory setup over time. It was tolerated at that point because it yielded the most stable performance. Especially in the pump arm of OPA 2, the influence of the Kerr lens is still clearly visible at the corresponding peak power of >3.6 GW, but induces no optical damages. In contrast to this, only a small remaining Kerr lens effect is observed in the final stage, despite the higher pulse energy and propagation distance. The difference originates from the initial transmission through the ∼11 mm-thick TFP in the pump pulse split-up. The TFP substrate has a 10^3-times higher n_2 than air and significantly enhances the nonlinearities.

In OPA 2, a 3 mm-short BBO crystal with an aperture of $15 \times 15\,\mathrm{mm}^2$ is mounted in a temperature-stabilized copper holder, set to 40 °C to ensure long-term phase matching. The crystal is cut at $\theta = 24°$ and equipped with a protection coating on both surfaces. The slight offset between the cutting angle and the phase matching angle prevents parasitic backreflection towards the incoming beam and protects the front end. Pump and seed are arranged in PVWC-geometry similar to the preamplifier with a noncollinear angle of $\alpha \approx 2.44°$.
In this configuration, the signal is amplified to an intermediate energy of 0.6 mJ, corresponding to an optical efficiency of 10.9 % in OPA 2. The spectral evolution throughout the amplification stages is depicted in figure 6.16, while the corresponding signal beam profiles are shown in figure 6.15. With a spectral bandwidth of 295 nm at −10 dB, the spectrum after the first poweramplifier supports a FTL of 6.4 fs. Because the shape of the signal beam profile is determined by the pump, it exhibits the same characteristic bulge in the horizontal plane.

The final poweramplifier OPA 3 is set up similar to OPA 2, utilizing a 2 mm-short BBO crystal in PVWC-geometry with pump and seed incident under $\alpha \approx 2.44°$. The pump beam size is adjusted to $w_p \approx 2.0$ mm (2.2 mm) in the vertical (horizontal) plane at low power, corresponding to an intensity of $\sim 80\,\mathrm{GW/cm}^2$ to compensate for the shorter crystal length.
Due to optical losses in the beam path, the seed energy is reduced to 0.54 mJ at the

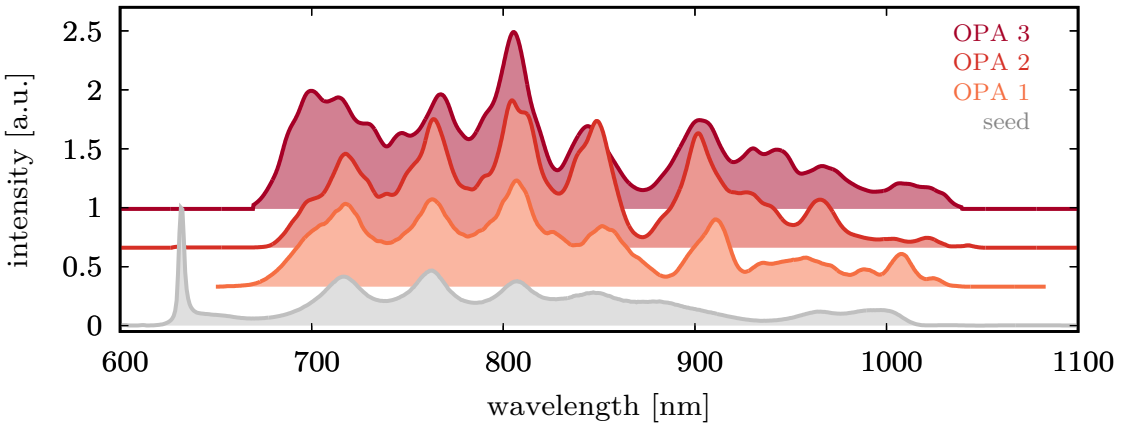

Figure 6.16.: Signal spectra after amplification in the three OPA stages. The seed spectrum is indicated as comparison. The spectra are individually scaled for visibility.

crystal. After amplification, pulse energies of 2.4 mJ are obtained at a conversion efficiency of 21.9 %. Because the amplification is saturated, the spectral −10 dB-bandwidth and the corresponding FTL approach the values obtained after the preamplifier again, being 350 nm and 6.1 fs, respectively. As a result of forth- and backconversion between signal, idler and pump, the signal beam profile is notably modulated (figure 6.15).

6.5.3. Pulse Compression

Pulse compression is performed in a DCM compressor, consisting of multiple commercially available mirror pairs (DCM11, venteon Laser Technologies GmbH). The DCMs are designed for operation in the wavelength range between 650 nm and 1050 nm and introduce a GDD of $-130\,\mathrm{fs}^2$ per pair. A total of 13 bounces suffices to compensate the dispersion introduced in the amplifier chain up to the second order. Dispersion fine tuning is performed via the CaF_2-wedge pair in front of OPA 1. A compressed pulse energy of 2.1 mJ is obtained, corresponding to 87.5 % compression efficiency.
The temporal pulse characteristics are measured with SPIDER [117] (venteon Laser Technologies GmbH). Figure 6.17 presents the shortest obtainable pulses after amplification in OPA 1 and OPA 2 (left) and after amplification in all three stages (right).

Amplification up to the first poweramplifier already induces a parametric phase of higher order, obvious in the GD of the measured pulse. The indicated second order polynomial fit reveals a small amount of TOD. Noteable side-pulses are visible in the reconstructed pulse shape which has a FWHM of 1.44 × FTL. Things get worse in the final poweramplifier, where the higher-order parametric phase components increase. This effect can be observed already at low pump pulse energies, before saturation sets in. It results in a distorted pulse shape, which is not further compressible by the employed chirped mirrors only. Integration of a programmable dispersive filter [109,119] or customized chirped mirrors would in theory allow for the compensation of most parasitic phase components. However, the former comes at the cost of additional optical losses while the latter one is a time-consuming approach, potentially requiring multiple iterations in the mirror design to properly match the dispersion. Beyond, both options are costly.

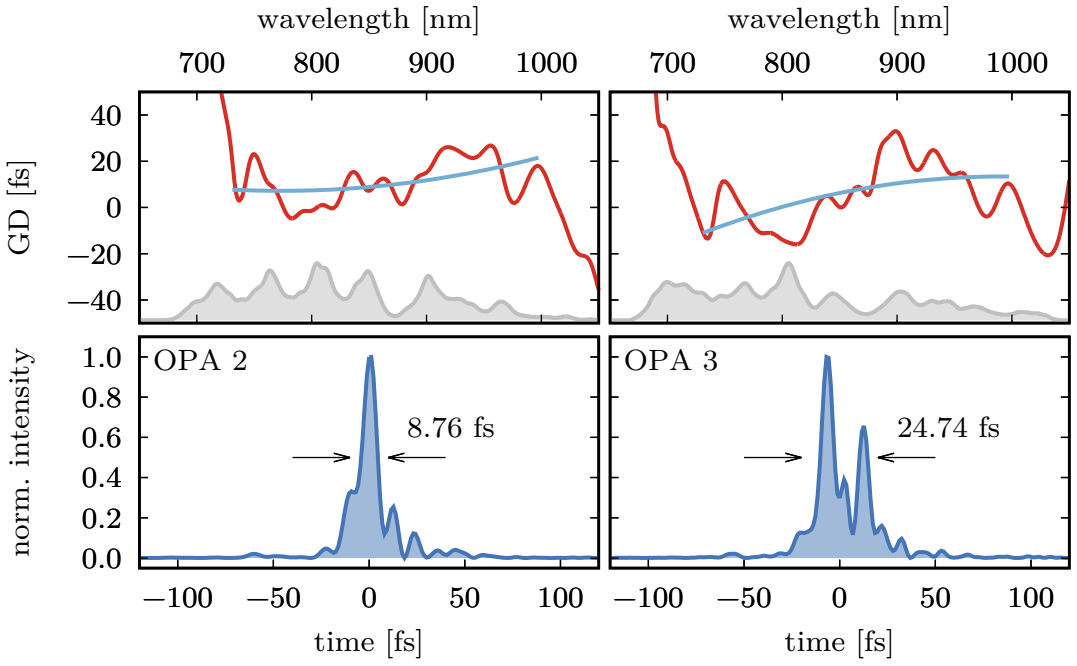

Figure 6.17.: Pulse characteristics after amplification in OPA 2 (left) and OPA 3 (right), measured with SPIDER. The upper graphs show the GD (red) and its second order polynomial fit (blue). As reference, the normalized signal spectrum is indicated in grey. The bottom depicts the reconstructed pulse shape.

Because the parametric phase in OPA 3 substantially distorts the pulse shape already at low intensities, a systematic phase mismatch is likely to be part of the problem. Several attempts were carried out to minimize the parametric phase in the given setup. Neither alteration of θ and α towards the magic angle [21] nor changing the geometry from PVWC to TPM could improve the temporal pulse shape. This suggests a fundamental problem that may well originate already in OPA 2, in which the pump beam is notably affected by Kerr lensing.

Kerr lensing is known to alter not only the spatial pulse shape, but also the spectral and temporal phase (compare section 6.3). This translates directly into the phase mismatch Δk between pump and signal, decreasing the parametric gain and enhancing the parametric phase contributions [81, 107]. Following this assumption, further alteration of the setup is necessary to improve the pulse compression with the given means.

6.5.4. Summary

Parametric amplification to pulse energies of 2.4 mJ is achieved in three OPA stages with a FTL pulse duration of 6.1 fs. Compression in a DCM compressor is not sufficient to achieve pulse durations below 8 fs, as higher-order parametric phase contributions distort the temporal pulse shape. Because the influence of Kerr lensing on the pump beam is still clearly visible in this configuration, an altered spectral and temporal phase is likely to increase the phase-mismatch and thus, the parametric phase contributions.

Further reduction of the nonlinearities is therefore of paramount importance to achieve pulse compression close to the FTL without the implementation of active phase-shaping

devices.

6.6. Concept C: Multiple SHG Stages

Like all the presented OPCPA concepts so far, this concept has first been implemented and qualified with the regenerative amplifier realized as a laboratory setup only. After initial successful tests, the pump laser was transferred to its final and more stable platform, described in section 4.9. All the results presented in this section were obtained after the platform transfer and represent the final system performance.

6.6.1. Experimental Setup

The final setup of the OPCPA system is designed to minimize the influence of Kerr lensing to the pump while still maintaining picosecond pump pulse duration as well as operation in air. Because the critical peak power $P_{mathrmcr}$ scales with λ^2 according to equation 2.21, higher nonlinearities are expected at lower wavelengths. On that account, the single SHG stage is replaced by three SHG stages, positioned as close to the OPAs as possible to minimize beam propagation at 515 nm. Additionally, the fundamental beam is split up right after passing the beam stabilization optics at the input of the OPCPA system to reduce the peak power in each arm. Figure 6.18 depicts the schematic layout of the setup.

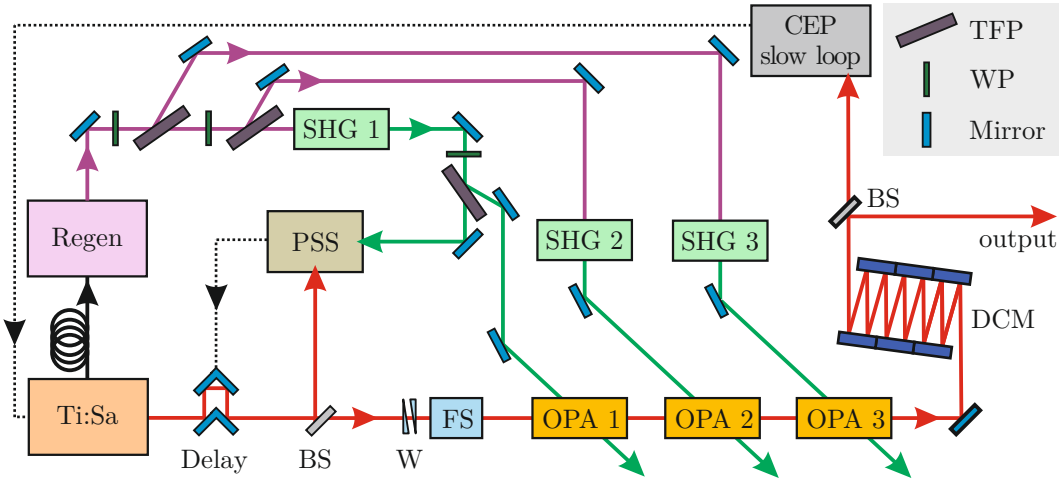

Figure 6.18.: Schematic setup of OPCPA concept C. Ti:Sa: Titanium-sappphire oscillator, Regen: regenerative amplifier, SHG: second-harmonic generation, PSS: pump-seed synchronization, BS: beam splitter, W: wedge pair, FS: fused silica stretcher, OPA: optical parametric amplifier, DCM: double-chirped mirror compressor, TFP: thin-film polarizer, WP: waveplate.

6.6.2. Second Harmonic Generation

The parameters used in each SHG stage are listed in table 6.2. A 2 mm-short LBO crystal is employed in every stage, temperature-stabilized to 40 °C. To compare the influence of the nonlinearities, the B-Integral of the fundamental beam, B_{1030}, is calculated for each

SHG stage. The calculation is initiated at the output of the last compressor grating, where the pulse duration is the shortest. The beam path to the first TFP in the OPCPA setup is around 3 m. From there on, the propagation distances to SHG 1, SHG 2 and SHG 3 are 2 m, 4 m and 5 m respectively. The effects of the TFPs were included, when necessary.

Table 6.2.: Experimental parameters for second harmonic generation in the three SHG stages.

	E_{1030} [mJ]	I [GW/cm^2]	E_{515} [mJ]	η [%]	B_{1030}
SHG 1	0.11	~ 100	0.066	60.0	0.50
SHG 2	10.54	~ 80	5.04	47.8	0.93
SHG 3	15.72	~ 80	8.20	52.2	0.72
Total	26.37	-	13.306	50.5	-

A total conversion efficiency slightly above 50 % is measured, resulting in 13.3 mJ at 515 nm with pulse-to-pulse fluctuations of ∼1 % rms, measured over 4000 consecutive pulses. Compared to $\eta = 63\,\%$ obtained in a single SHG stage employed close to the regenerative amplifier (compare section 4.10), the efficiency is >12 % lower in this configuration. A significant difference in η is furthermore observed among the successive stages that correlates with the B-Integral, obviously diminishing the conversion efficiency.

The theory of detrimental influence stemming from nonlinearities accumulated during beam propagation in air formulated in section 6.3 is now proven in a simple experiment, performed in SHG 3. An operating regime with reduced nonlinearities is constructed by attenuating the fundamental pulse energy right after the regenerative amplifier cavity to 15.7 mJ, while the remaining 13 mJ are dumped. The attenuated beam is sent through the compressor and reflected completely at the first TFP of the pulse-splitting setup towards the SHG crystal. Thanks to the lower energy in the beam path up to the TFP, less nonlinearities are accumulated during propagation. Consequently, this configuration reduces the B-Integral by ∼20 % to $B_{1030} = 0.58$.
Figure 6.19 displays the measured conversion characteristics of SHG 3 for different values of B_{1030}. Energy and efficiency follow the same trend in both cases, but the efficiency is up to 5 % higher when nonlinearities are reduced in comparison to the usual operation. Since the total B-integral in both cases is still relatively low, the reduced efficiencies are mainly attributed to the energy drain from the quasi-collimated center of high intensity, described in section 6.3. As conversion takes place predominantly in the intense part of the fundamental beam, there is effectively less energy available to pump the parametric process.

6.6.3. Parametric Amplification

Table 6.3 summarizes the experimental parameters in every OPA stage. Kerr lensing effects on the pump beams are greatly reduced, which is evident by comparing the pump beam profiles of OPA 2 and OPA 3 in the crystal plane in figure 6.20 at low and full energy. The pulses are locked in time by PSS$_\beta$ with a remaining timing jitter below 10 fs rms ($0.8\,\% \times \tau_p$), as evaluated in section 5.4.1.3.

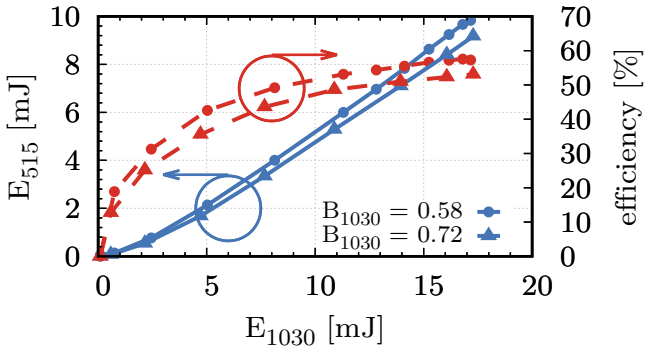

Figure 6.19.: Measured characteristics of SHG 3 under the influence of strong and weak nonlinear effects, characterized by the B-Integral B_{1030}.

Table 6.3.: Final experimental parameters in the three OPA stages.

	E_{seed} [mJ]	E_{pump} [mJ]	E_{signal} [mJ]	η [%]	L [mm]	Geom.
OPA 1	5.2×10^{-7}	0.06	5.7×10^{-3}	9.5	3.0	PVWC
OPA 2	4.6×10^{-3}	5.04	0.78	15.4	2.0	PVWC
OPA 3	0.67	8.20	2.02	16.7	3.0	TPM

Figure 6.21 indicates the amplified signal spectra. In the preamplification stage, an intensity of 120 GW/cm^2 is achieved at $E_p = 60\,\mu$J due to a slightly larger pump beam size of $w_p = 145\,\mu$m compared to the previous setups. The seed is boosted to 5.7 µJ with an efficiency of $\eta = 9.5\,\%$. As a result of PVWC geometry, a spectral dip around 870 nm is generated by parasitic SHG which is maintained throughout the whole amplification process.

After preamplification, the pulse energies are further boosted from the µJ- to the mJ-level in OPA 2 and 3. BBO crystals with an aperture of $15 \times 15\,$mm^2, cut at $\theta = 24°$ are implemented in each stage inside a temperature-stabilized copper holder. A noncollinear angle of ∼2.44° between pump and seed is chosen to match the amplification bandwidth of OPA 1. Experimentally, both stages are aligned to maximum conversion efficiency. The amplification characteristics of the poweramplifiers with increasing pump pulse energy E_p are depicted in figure 6.22. The rms pulse-to-pulse fluctuation E_{rms} is measured over 4000 consecutive pulses. The FTL is extracted from the measured spectra. Via 4-f imaging, the signal beam profile in the crystal plane is obtained.

In the first poweramplifier OPA 2, a pump intensity of ∼60 GW/cm^2 is set to drive the amplification process into saturation above $E_p > 2\,$mJ. Compared to the unsaturated

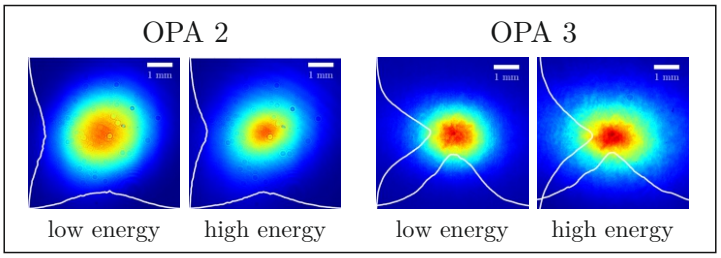

Figure 6.20.: Pump beam profiles in the poweramplification stages OPA 2 and OPA 3 at low and full energy, according to table 6.3. The influence of Kerr lensing is greatly reduced in this setup.

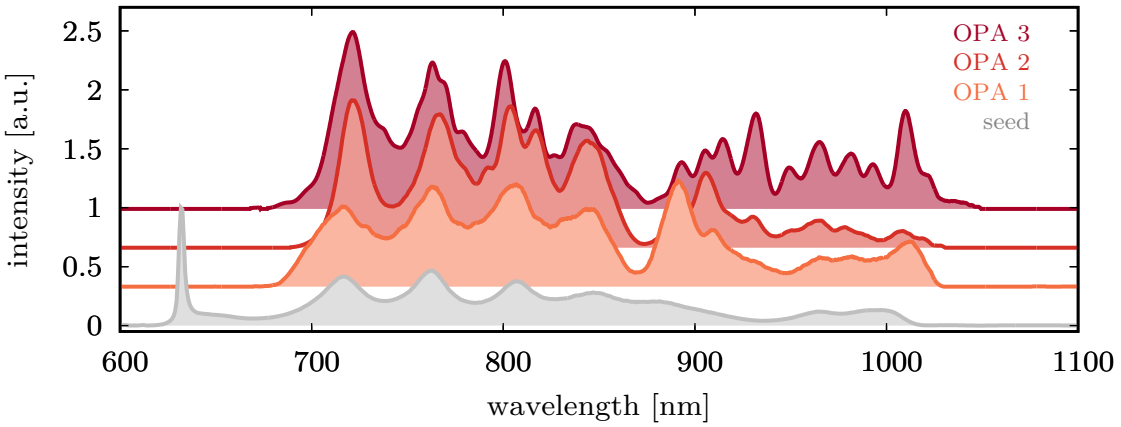

Figure 6.21.: Signal spectra after amplification in the three OPA stages. The seed spectrum is indicated as comparison. The spectra are individually scaled for visibility.

regime, pulse-to-pulse fluctuations are significantly decreased down to a standard deviation of ∼1 % rms. At low pump intensities, the spectral wings experience low gain in the amplification process which results in an increase of the FTL to above 9 fs. With increasing pump energy, the FTL is further reduced as a consequence of gain saturation in the central part of the spectrum, facilitating the amplification of the spectral wings. In the spatial domain, saturation results in forth- and backconversion between pump, signal and idler, which notably alters the signal beam profile. This is further investigated in section 6.8. A 2 mm-short BBO crystal in PVWC geometry allows for the best achievable pulse compression after the final poweramplifier, presented in the following section 6.6.4. Changing the geometry to TPM results in equal parameters after amplification, but does not increase the efficiency as may be expected thanks to the absence of the parasitic SHG [50]. The reason is that in the preamplifier, a spectral dip is already imprinted on the spectrum which hinders amplification in the affected part of the spectrum.

The final poweramplifier OPA 3 raises the signal pulse energy by another factor of 3 beyond 2 mJ. Due to the high seed energy, the process quickly saturates, reaching its peak efficiency of 19.3 % already at ∼15 GW/cm^2 in the 3 mm-short BBO crystal. With increasing gain, the FTL approaches 6 fs again, finally covering a spectral bandwidth of 329 nm at −10 dB, centered around $\lambda = 810.7$ nm at a pump intensity of ∼70 GW/cm^2. The pulse-to-pulse fluctuations remain at a constant low level around 1 % rms. After peaking, the efficiency drops again and settles around 17 %, representing a balance between forth- and backconversion. This causes visible modulations in the beam profile as well as in the amplified spectrum (figure 6.21). In this stage, the TPM geometry proves to be favorable in terms of final pulse compression, which could not be achieved in PVWC. Utilizing a 2 mm-short BBO crystal reduces the conversion efficiency by ∼2.5 % and was therefore reverted.

Operating the final poweramplification stage in heavy saturation has the benefit of broadband amplification, enhancing even the outer spectral wings which are usually supressed by the gain characteristics in an OPCPA [60, 61]. Thus, the FTL of 6.1 fs which is preset by the preamplifier can be preserved in this system throughout the poweramplifiers by

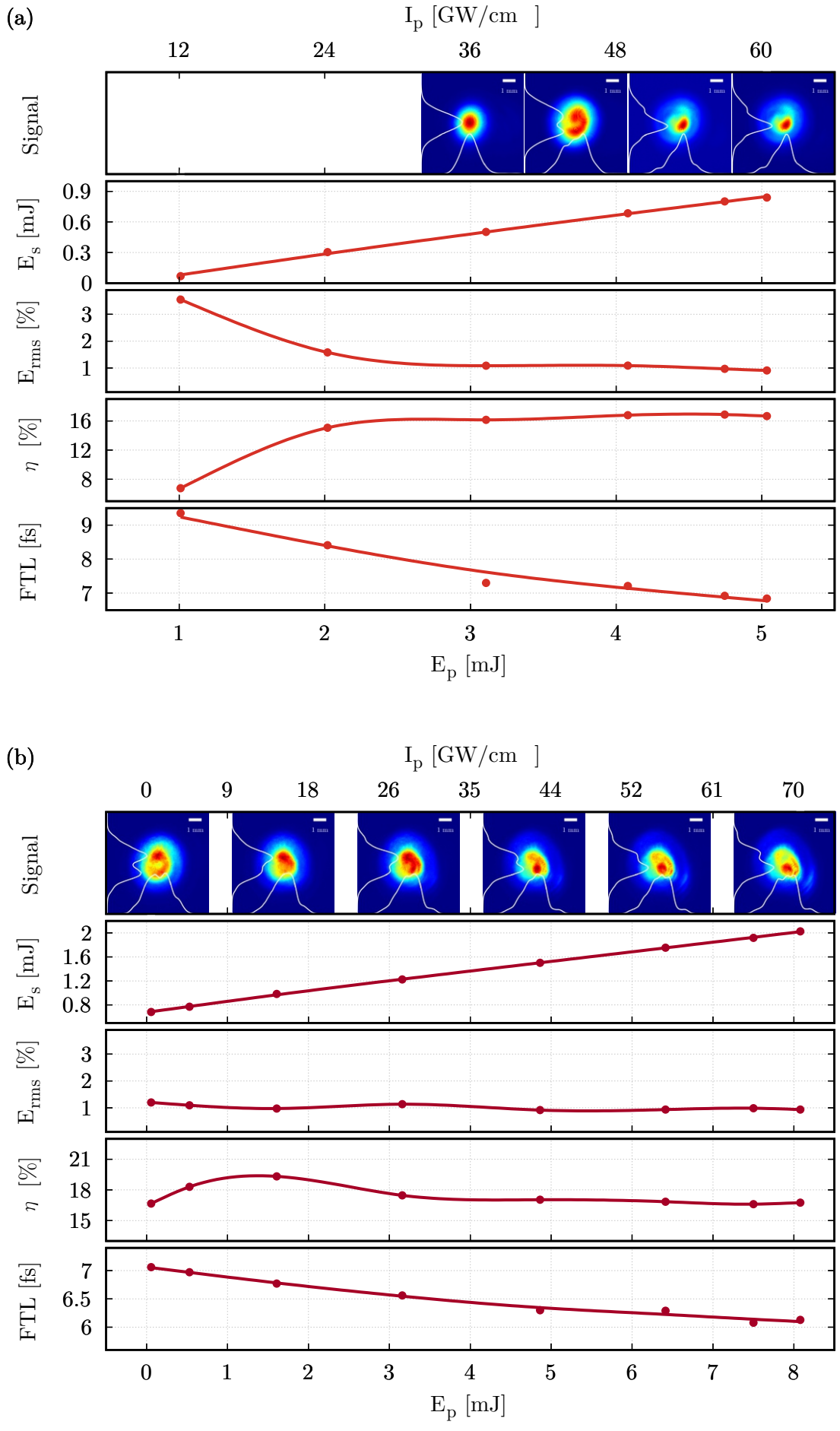

Figure 6.22.: Amplification characteristics in (a) OPA 2 and (b) OPA 3. The beam profile on top represents the amplified signal in the crystal plane.

making a small sacrifice in conversion efficiency. The potential drawbacks of this approach are investigated in the following sections.

Estimation of Parametric Superfluorescence

The amount of generated PSF is investigated experimentally in two steps. First, the seed in front of the respective amplification stage is blocked while the pump is operated at full power. A powermeter[1] detects the emitted PSF at the position of the signal right after the OPA. In this scenario, no PSF power above the detection threshold according to equation 6.3 is detected throughout all the OPA stages.
In the second step, the seed is blocked in front of the preamplifier and all stages are operated in their usual setpoint. Now, the immeasurable small amount of PSF generated in OPA 1 serves as the seed which is further amplified in the poweramplifiers to 3.2 W in OPA 2 and up to 8.8 W in OPA 3, measured at the system output. This corresponds to ∼81 % of the total output power. However, based on the simulation results in section 6.2.1, a significant decrease is expected in the presence of the seed.
The final pulse contrast at the system output is estimated by taking into account the pulse compression of $\sim 2 \times 10^2$ and a conservative gain quenching factor of 10 in the preamplifier. This results in a contrast of $\sim 6.2 \times 10^{-4}$ and constitutes a value comparable to other high gain OPCPA systems [2, 82, 99, 102]. Since according to the simulation, much higher gain quenching values can be expected in the poweramplifiers, which have been neglected here, this value represents a lower limit for the real pulse contrast.

6.6.4. Pulse Compression

Analog to the setup described in section 6.5.3, the pulses are compressed in a DCM compressor (DCM11, venteon Laser Technologies GmbH) utilizing 13 bounces per mirror pair. After compression and a beamsplitter, which is used to transmits 1 % of the energy to the CEP slow loop and the diagnostics, a pulse energy of 1.8 mJ is available at the output, corresponding to a compression efficiency of 89 %.
Figure 6.23 (a) presents the pulse compression after the first (left) and the second poweramplifier (right), measured with SPIDER. Despite visible GD-oscillations and a small amount of TOD, a short pulse is obtained after OPA 2 and OPA 3 with a pulse duration of 1.21 × FTL and 1.15 × FTL, respectively. Only minor satellite pulses are visible due to higher-order dispersion, while more than 70 % of the total energy are contained within the main pulse after final amplification. This results in a peak power as high as 169 GW.
The long-term stability of the amplifier chain is attested by continuous pulse duration measurement every 10 s over a period of 30 min, presented in figure 6.23 (b). A mean pulse duration of 7.16 fs with a standard deviation of only 199 as is evaluated, corresponding to 2.6 optical cycles at the central wavelength of 810.7 nm.

Reducing the nonlinearities in the pump beam enables compression of the amplified signal pulses close to the FTL with only minor satellite pulses. Despite forth- and backconversion between the involved beams in the oversaturated operating regime, the higher-order

[1] Gentec XLP12-3S-H2, Noise Equivalent Power = 0.5 μW

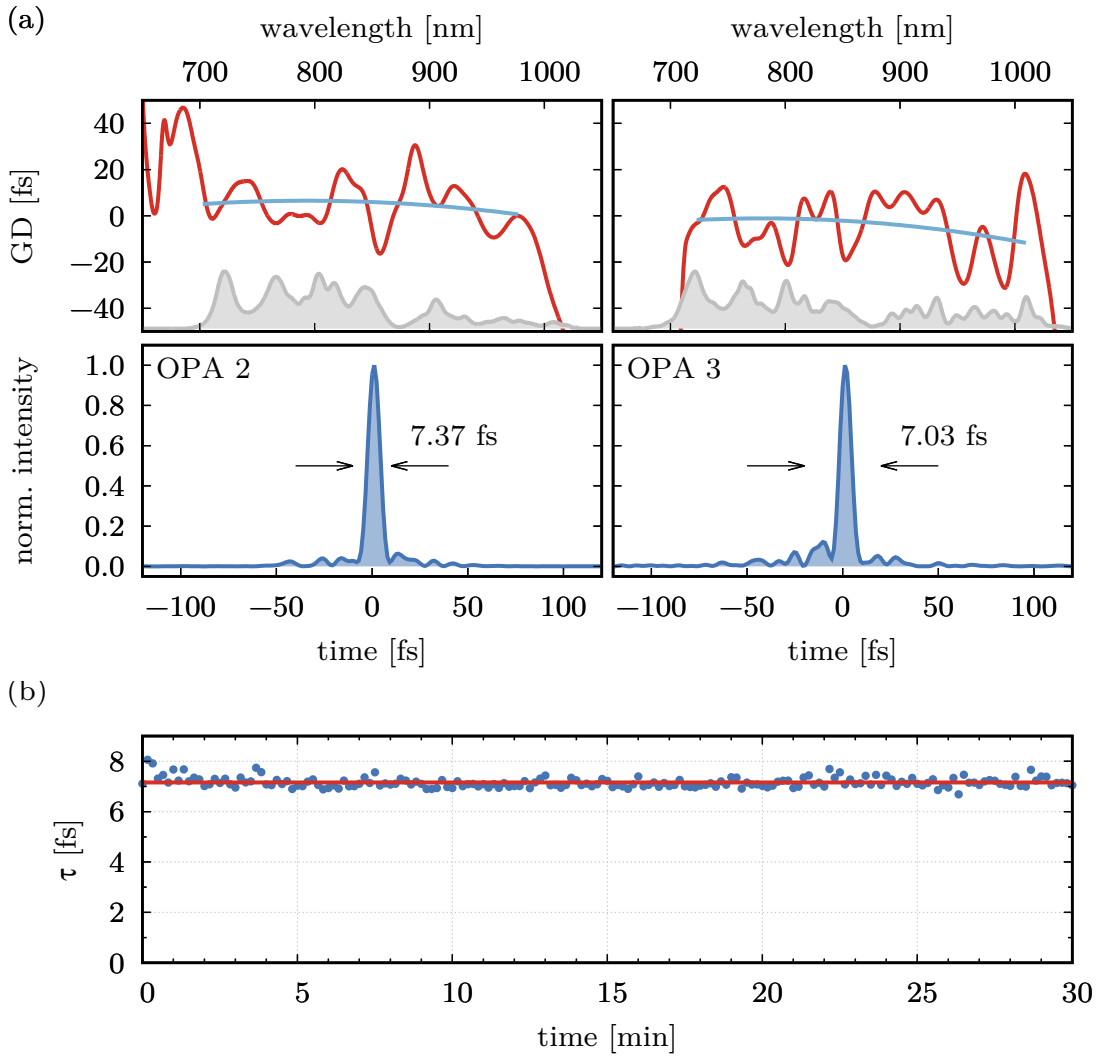

Figure 6.23.: (a) Pulse characteristics after amplification in OPA 2 (left) and OPA 3 (right), measured with SPIDER. The upper graphs show the GD (red) and its second order polynomial fit (blue). As reference, the normalized spectrum is indicated in grey. In the bottom, the reconstructed pulse shape is displayed. (b) Long-term pulse duration measurement at full energy with a mean pulse duration of $\tau = 7.16\,\mathrm{fs}$ (red) and a standard deviation of 199 as.

parametric phase contributions are small enough to not distort the pulse shape. Utilizing PVWC geometry in OPA 3 at first prevented clean pulse compression at full energy due to pronounced GD ripples, leading to considerable satellite pulses. By changing the geometry to TPM, those satellites are reduced significantly and the majority of the energy is now confined within the main pulse. This might be enabled by the absence of parasitic SHG and the associated phase jump [32].

6.6.5. Long-Term Performance

The compressed output power of the OPCPA system is recorded over 13 hours of operation, as plotted in figure 6.24. The measurement starts after the one hour warm-up phase of the regenerative amplifier, when thermal drifts have largely settled. As soon as the pump beam is automatically aligned by the integrated beam stabilization to the OPA stages and the temporal overlap is locked via the PSS, the full output power of more than 10.8 W is available.

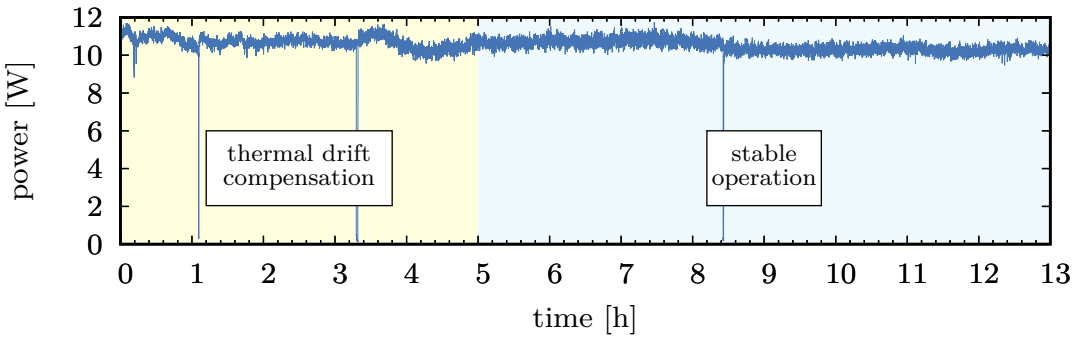

Figure 6.24.: Long-term power measurement of the OPCPA output.

In the first 5 h, small readjustments of the pump are necessary from time to time as the regenerative amplifier still suffers from slow thermal drifts (compare section 4.9). At $t \approx 1$ h and 3.2 h, large spatial offsets were introduced during automated alignment by the beam stabilization, causing large power drops at the output. After 5 h, no more intervention was necessary with exception at $t \approx 8.4$ h, as by this time thermal drifts are reduced to a minimum. In the time period between $t = 5$ h and 8.4 h and $t = 8.4$ h and 13 h, the power fluctuation is evaluated to be 1.8 % rms. Pulse-to-pulse energy monitoring over 100 000 pulses in a time period of ∼17 min reveals the same value, proving the absence of high-frequency noise in the system which is often hidden by the low-pass properties of thermopile detectors. Compared to the short-term pulse-to-pulse fluctuations of 1 % rms, measured in section 6.6.3 over less than 1 s, the increase to 1.8 % is attributed mainly to slow spatial drifts which are not sufficiently compensated by the rather slow and inaccurate beam stabilization.
This assumption is verified by recording the interdependence of output power and beam pointing. The latter is detected by one of the camera-based detectors used in the beam stabilization. The data is depicted in figure 6.25.

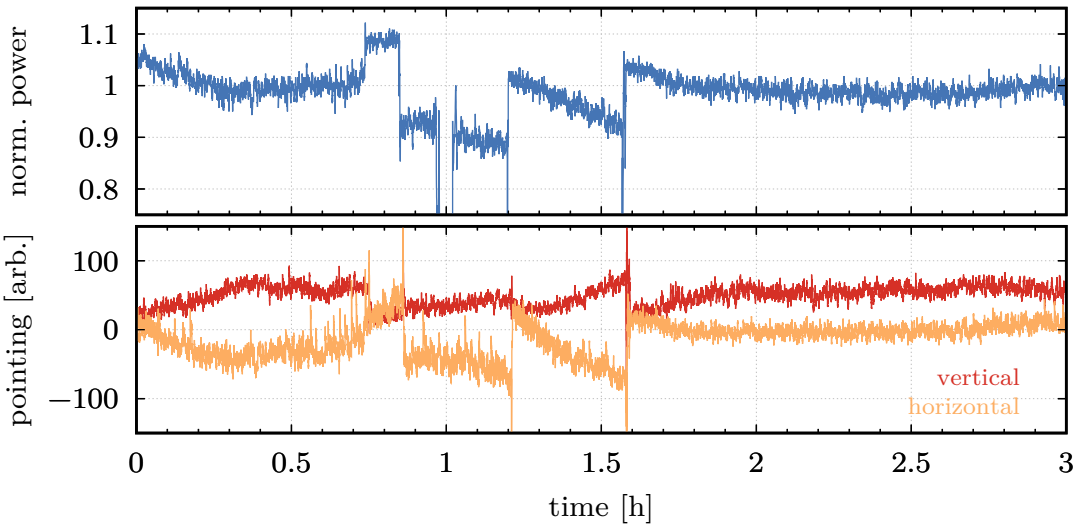

Figure 6.25.: Parallel measurement of OPCPA output power and beam pointing, as it is detected by one of the cameras used in the beam stabilization setup.

Every sudden change in power is a consequence of a pump beam realignment, either performed manually (i.e. at $t \approx 0.7\,\mathrm{h}$ and $0.9\,\mathrm{h}$) or automatically by the beam stabilization, if the beam centroid deviation from the setpoint exceeds a specific threshold value (i.e. at $t \approx 1.2\,\mathrm{h}$ and $1.6\,\mathrm{h}$). A clear correlation between the course of output power and beam pointing is evident, especially in the horizontal direction. Power variations of $\pm 10\,\%$ are measured in dependence of the pump beam alignment and even after automatic realignment of the beam to the center, slight variations in output power remain because the setpoint cannot be exactly reproduced. In the time period $>2\,\mathrm{h}$, as thermal drifts have settled and the alignment of the pump does not change any more, also the output power stays constant.

The obvious solution to gain better control over the alignment is to allow only minimal deviations from the beam stabilization setpoint by lowering the deviation threshold. However, this leads to uncontrolled behavior in the movement of the motorized mirrors, with occasional large deviations of some millimeters, induced by the beam stabilization algorithm itself. Such uncontrolled behavior represents a menace to the system components and therefore hinders this approach. In the future, a in-house developed beam stabilization is planned which allows full control over all feedback parameters and will potentially enhance the long-term stability of the system down to the short-term pulse fluctuations of $1\,\%$ rms.

6.6.6. Summary

With an adapted system design, pulse amplification to more than $2\,\mathrm{mJ}$ is accomplished in three OPA stages. By minimizing the nonlinearities affecting the pump and changing the geometry of the final poweramplifier, pulse compression to $\sim 7\,\mathrm{fs}$ in a double-chirped mirror compressor is realized without additional active pulse-shaping devices. Compressed pulses with energies of $1.8\,\mathrm{mJ}$ ($10.8\,\mathrm{W}$) are available at the output, exhibiting peak powers as high

as 169 GW. On a short timescale, pulse fluctuations as low as ∼1 % rms are measured, while the long-term stability of 1.8 % rms is slightly larger due to a slowly drifting pump beam. The implemented beam stabilization is not capable to compensate for those slow drifts as expected and will thus be replaced in the future.

6.7. Carrier-Envelope Phase

To detect the CEP after amplification, a commercial f-to-2f common path interferometer (APS800, Menlosystems GmbH) is integrated after the pulse compression. The schematic setup is depicted in figure 6.26.

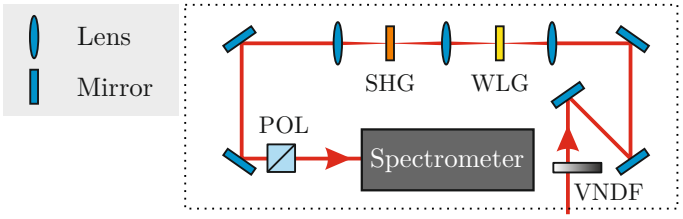

Figure 6.26.: Schematic setup of the common path f-to-2f interferometer for CEP detection. VNDF: variable neutral density filter, WP: waveplate, WLG: white-light generation, SHG: second harmonic generation, POL: polarizer.

The basic principle of the detection scheme follows reference [8]. Approximately 18 µJ are transmitted at the beamsplitter after compression towards the interferometer. A pinhole and a variable neutral density filter are used to select the central part of the beam and adjust the energy to generate a single, stable filament in a 1 mm-short sapphire plate. Here, the spectrum is extended to more than one optical octave by WLG. Another lens focuses the beam into a 0.5 mm-thin BBO crystal, where a fraction is frequency doubled to cover the spectral range of the blue-shifted fundamental spectrum around 520 nm. The signal is recollimated by a third lens and a polarizing cube enables interference of both signals by selecting a common polarization component of both beams. The resulting interferogram $S(\omega)$ of the white light with intensity I_{WL} and phase ϕ_{WL} and the SHG with intensity I_{SHG} and phase ϕ_{SHG} can be expressed as

$$\begin{aligned} S(\omega) =&(1-a)I_{WL}(\omega) + aI_{SHG}(\omega) + 2\sqrt{a(1-a)I_{WL}(\omega)I_{SHG}(\omega)} \\ &\times \cos(\phi_{SHG}(\omega) - \phi_{WL}(\omega) + \omega\tau_0 + \varphi), \end{aligned} \tag{6.4}$$

where the coefficient a describes the transmission of the SHG light through the polarizer. The time delay τ_0 between both signals is given by the dispersion of the employed sapphire plate and the BBO crystal. Timing jitter between the interfering beams, which would directly affect the fringe pattern and disturb the measurement, is neglegible thanks to the colinear geometry. A spectrometer (SP3, Thorlabs GmbH) detects the interferogram from which the relative CEP change $\delta\varphi$ is extracted by the standard algorithm of Fourier transform spectral interferometry [101].

Figure 6.27 depicts a typical interferogram, acquired at a spectrometer integration time of 167 µs, hence integrating over a single pulse only. The spectral region used to compute

the CEP is colored in orange. Towards higher wavelengths, the tail of the white light continuum is visible, while the frequency doubled signal is located at lower wavelengths. Given the spectrometer dead time of 10 ms, the CEP is recorded at an acquisition rate of 100 Hz. The measured CEP behaviour is shown in figure 6.28. In the free running case, the

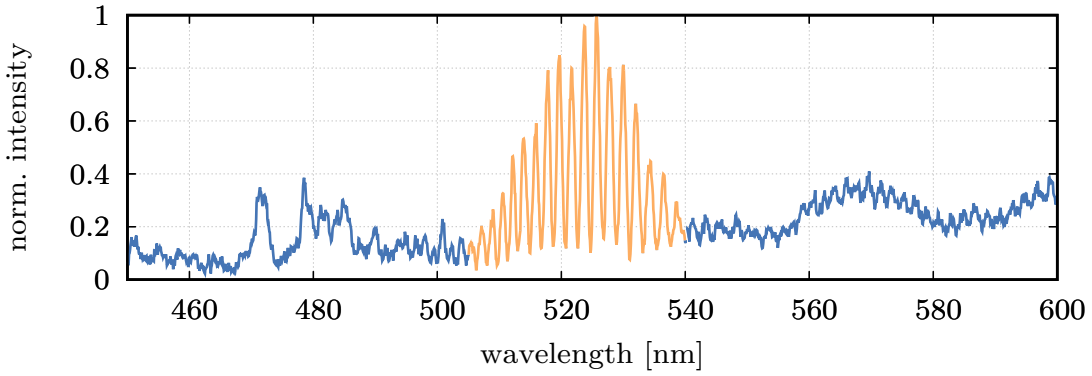

Figure 6.27.: Typical interferogram detected in the f-to-2f interferometer at an integration time of 167 µs, integrating over a single pulse. The relative CEP is extracted from the fringe pattern colored in orange.

CEP of the amplified pulses fluctutates with an amplitude of more than π, hindering the reproducible generation of high harmonics [7]. After activation of the slow loop feedback to the seed oscillator, the relative phase offset is locked with a residual standard deviation of only 169 mrad, being 2.4× higher than the specified phase noise from the oscillator itself.

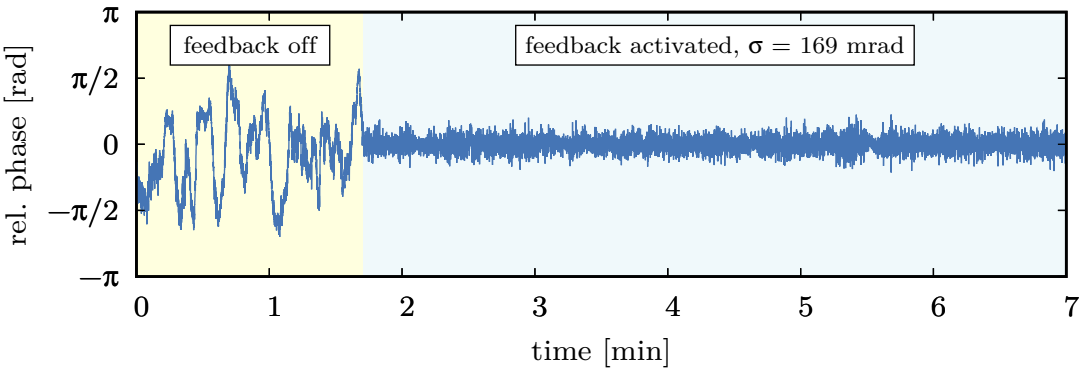

Figure 6.28.: CEP behaviour detected by the f-to-2f interferometer without (yellow shaded area) and with activated slow loop feedback (blue shaded area) to the seed oscillator. In the latter case, the relative phase error amounts to $\sigma = 169$ mrad, integrated over a single pulse.

Possible origins of additional CEP noise during parametric amplification are pump-intensity coupling [78], pump-seed-timing jitter [34] and detection noise in the f-to-2f interferometer. Influence resulting from the stretcher/compressor setup can be excluded, because no pointing-sensitive devices are used. Pump-intensity coupling is estimated to be well below the CEP noise of the oscillator (∼70 mrad rms), given the excellent pump-energy stability in the green of 1 % rms. The same assumption holds for the small remaining timing jitter of 0.8 % × τ_p rms.

The majority of the detected CEP noise is thus attributed to detection noise in the employed f-to-2f interferometer, resulting from amplitude-to-phase coupling in the process of WLG. A peak-to-peak phase-shift of $\phi_{WL} = 84\,\text{mrad}$ was observed by Baltuška et al. to accompany a pulse-energy jump of only 1 % [8]. Taking into account the long-term amplified signal-pulse energy fluctuation of 1.8 % rms, a detection limit of >150 mrad rms is expected, which limits the final CEP noise. This could be improved in the future by eliminating the process of WLG, e.g. by using a 2f-to-3f interferometer.

6.8. OPCPA Output Characteristics

In the following, potential drawbacks originating from operation of an oversaturated amplifier are investigated to qualify the system for its usability in HHG experiments.

6.8.1. Beam Caustic

Due to forth- and backconversion between signal, idler and pump pulse in the deeply saturated amplification regime of OPA 3, the near field beam profile at the system output is inhomogeneous and modulated in space. However, since most high-field experiments are performed in the focal plane, the far field beam profile is usually of greater interest. Hence, the focusability of the beam is investigated by measuring the caustic at different central wavelengths, selected by a bandpass filter with 10 nm FWHM around a specified central wavelength (FBXXX-10 series, Thorlabs). A fraction of the main beam is split off with help of a beam sampler and focused by a spherical silver-coated mirror with $f = 1000\,\text{mm}$. The beam is characterized along the beam axis with the M^2-measurement setup described in section 4.7.

As comparison, the output beam after amplification in OPA 1 and 2 is measured at first, leaving OPA 3 unpumped (figure 6.29 (a)). The onset of backconversion in the second amplifier is indicated by the central dip in the otherwise Gaussian-shaped near-field beam profile. Bandpass filter around 750 nm, 850 nm and 950 nm are used to analyze the chromatic error. In the horizontal axis (top), all wavelengths are focused in the same plane, whereas in the vertical axis (bottom), a wavelength dependent focal shift of $z_0(750\,\text{nm}) - z_0(950\,\text{nm}) = 0.33 \cdot z_R$ is observed, where z_R is the Rayleigh length at $\lambda = 850\,\text{nm}$ according to equation 4.3 and $z_0(\lambda)$ is the position of the focal plane at the central wavelength λ. The measured M^2 values are close to that of the pump laser, which also defines the beam astigmatism (compare to section 4.7). In the far field, a Gaussian beam profile is obtained. The circle marks the area around the beam center, in which 80 % of the total energy is contained. A high energy confinement with low diffraction losses is indicated by the small radius, attesting a good focusability.
The same measurement is performed at full output power with all three OPA stages pumped, presented in (b). Despite the previously mentioned modulated near-field beam profile, a good beam quality is acquired in the far field, indicated by the spatial confinement of the energy. In the vertical plane, the wavelength-dependent focal shift remains unchanged, whereas in the horizontal plane a chromatic error of the same order ($0.33 \cdot z_R$) is detected. An increase of the M^2 values is observed which can be compensated in the

experiment by using shorter focal lengths to match the desired far-field spot size. The astigmatism remains unchanged and can be compensated by cylindrical mirrors if necessary.

The characterization of the beam caustic reveals that even with a non-uniform beam profile, a good focusability can be attained. Since all wavelengths are focused within the Rayleigh length, no detrimental influence on intensity dependent applications as e.g. HHG is expected. A typical HHG-intensity of $10^{15}\,\mathrm{W/cm^2}$ can be generated at a $1/e^2$-beam radius of $w \approx 100\,\mu\mathrm{m}$ with the presented system parameters.

(a) OPA 3 unpumped

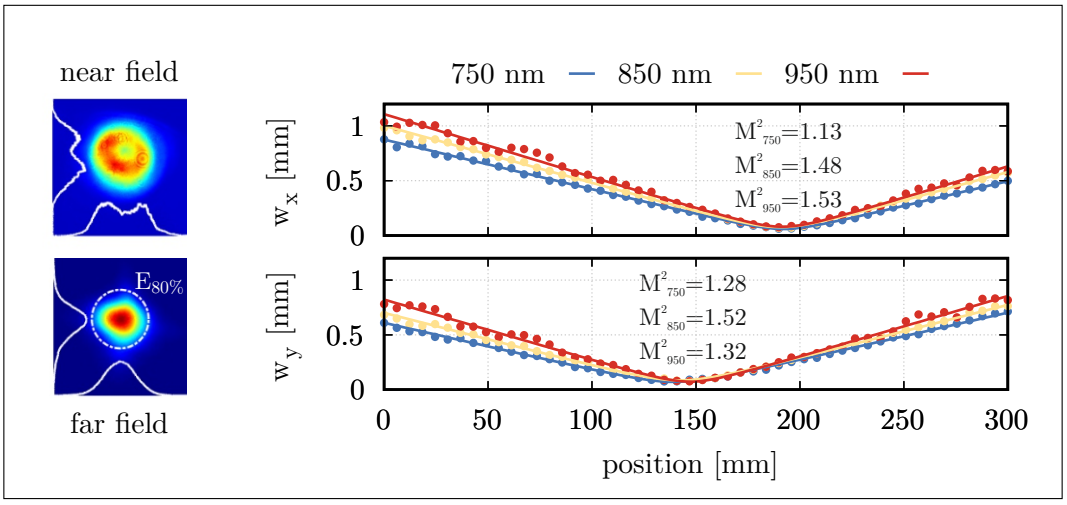

(b) all OPA stages

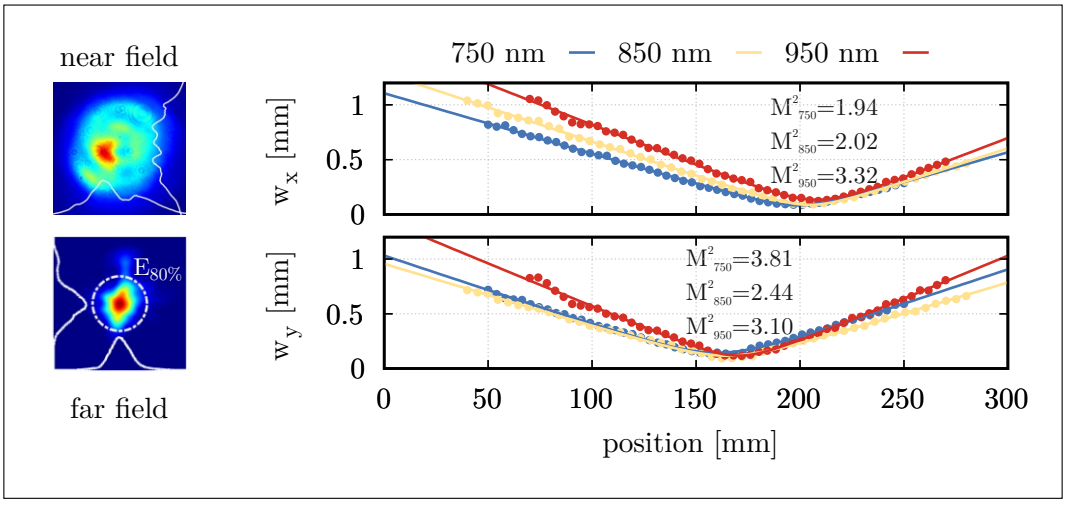

Figure 6.29.: Near and far field beam profile of the OPCPA and beam caustic in horizontal (top) and vertical axis (bottom) at different wavelengths. A bandpass filter (FWHM 10 nm) is used to select central wavelengths of 750 nm, 850 nm and 950 nm. The circle in the far-field beam profile marks the area in which 80 % of the total energy is confined. (a) OPA 3 left unpumped, (b) all OPA stages pumped.

6.8.2. Spatial Chirp

Forth- and backconversion as well as a pulse front tilt between pump and seed beam are known to induce a spatial chirp on the beam profile [32]. Due to spatiotemporal and spatiospectral coupling in the amplification process, this eventually results in a distorted spectral phase and/or impairs the focusability of the beam.
Thus, the spatial chirp is characterized by moving a 100 µm-thin vertical slit along the horizontal axis of the near field beam in steps of 0.5 mm, which is imaged to a spectrometer. Figure 6.30 depicts the position-dependent normalized spectra along the beam. To allocate the spectra to the respective part of the beam, the beam profile (rotated by 90°) is indicated as well.

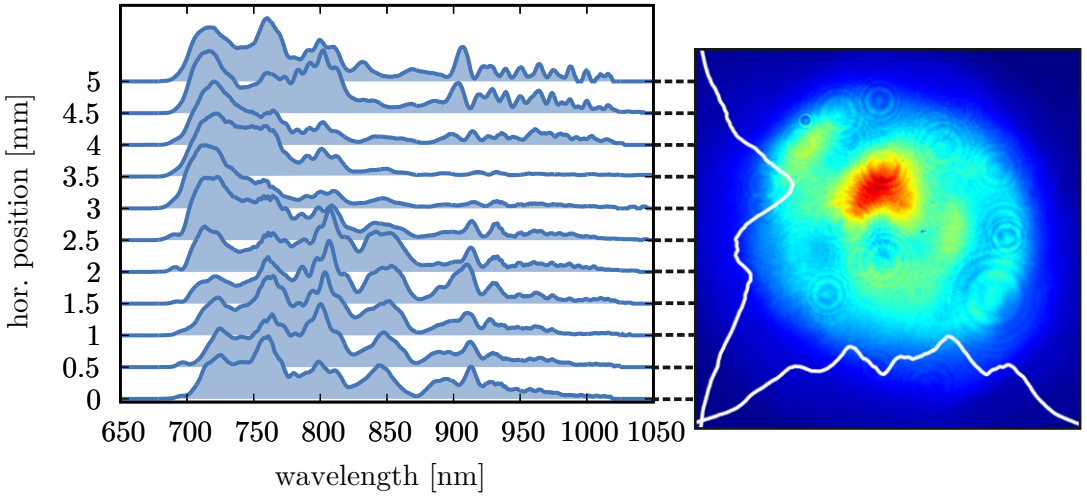

Figure 6.30.: Spatially resolved spectral distribution throughout the near field beam profile. A 100 µm thin slit imaged to a spectrometer is used to select different spatial slices of the beam. Every measured spectrum is normalized and plotted on a linear scale.

In the vicinity of maximum intensity, the spectrum is pronounced around 750 nm. Apart from this, only small spectral variations are detected. The detected small spatial chirp neither prevents pulse compression nor hinders the focusability of the beam in this system, which has already been confirmed in sections 6.6.4 and 6.8.1.

6.8.3. Temporal Contrast

One of the main advantages of using an ultrashort pump pulse is the absence of a comparably long PSF pedestal around the main pulse, which is common when using longer pump-pulse durations [104]. To validate this fact in the case of the developed system and to identify possible pre- or post-pulses, the home-build THG-AC presented in appendix B is used to measure the temporal contrast around the pulse. Compared to section 4.8, the setup has been adjusted to the central wavelength of the OPCPA signal by exchanging the conversion crystals. Short material lengths of 1.12 mm and 0.16 mm are used for SHG and THG, respectively, to achieve broadband conversion, covering the majority of the amplified spectrum. In addition, the detector is replaced by a gallium phosphide diode (FGAP71,

Thorlabs) which is more sensitive in the detection bandwidth around 280 nm. To enhance the measurement contrast up to 10^{-7}, a photodiode amplifier (PDA200C, Thorlabs) is used at different amplification levels to detect the signal. Because the dispersion in both arms is not matched, the measurement is not able to resemble the actual pulse contrast of the main pulse and the PSF pedestal. However, potential unwanted side pulses are readily identified. Figure 6.31 presents the acquired autocorrelation trace in a timeframe of 100 ps.

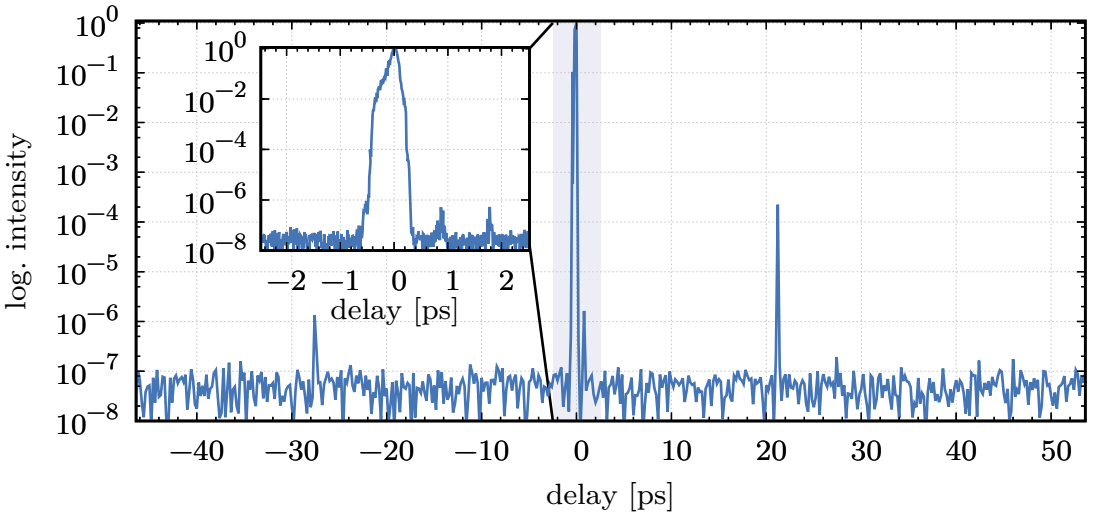

Figure 6.31.: Third-harmonic autocorrelation of the OPCPA output. Pre-pulses are located at negative delays, post-pulses at positive delays. A high resolution measurement (inset) around the main pulse attests of the excellent contrast.

As expected, the main pulse exhibits no temporal pedestal outside the ∼1 ps-short pump window. A post-pulse at $t = 21.2$ ps with a corrected intensity of $I/I_0 = 2.5 \times 10^{-4}$ is identified which likely originates from the backside reflection of the second OPA crystal. The less intense pulses at 0.9 ps, 1.8 ps and −28 ps constitute measurement artifacts introduced from parasitic reflections of the nonlinear crystals inside the autocorrelator.

Without the need for additional pulse-cleaning techniques using e.g. XPW [46] or a plasma mirror [24], the OPCPA generates an isolated main pulse of high contrast which contains almost the full energy. With the exception of only one post-pulse, which could be eliminated in the future by utilizing a nonlinear crystal cut at a slightly different angle in OPA 2, no other side-pulses are visible up to a contrast of 10^{-7}. The excellent temporal contrast discriminates the presented system from conventional Ti:Sa-based amplifiers which typically suffer from an ASE-pedestal spanning up to several nanoseconds and thus require either additional (lossy) pulse-cleaning or the implementation of complex ASE-supression techniques [43, 45, 77].

6.9. Summary

Using a commercial Ti:Sa-oscillator as the master seed source and the developed thin-disk regenerative amplifier as the pump source, a high-energy few-cycle OPCPA system with

unique output characteristics has been developed. Utilizing the previously designed PSS, the temporal overlap in the three BBO-based OPA stages is fixed with less than 10 fs rms remaining timing jitter which guarantees stable amplification from pulse to pulse. By employing a positive dispersion concept, the seed pulse duration is optimized inherently throughout every amplification stage without any intermediate adjustment. One major challenge in the system design is imposed by the manifestation of nonlinear effects in air, which has been investigated by numerical simulations and experimental observations. Three different system designs have been tested, in which the nonlinearities of the pump beam were gradually reduced to decrease the detrimental influence in terms of Kerr lensing and higher order phase distortions.

In the final setup, pulse energies of >1.8 mJ at a repetition rate of 6 kHz with >10.8 W average power are obtained. Excellent long-term stability over >13 h has been demonstrated, including short-term pulse-to-pulse fluctuations below 1 % rms, measured over 4000 samples (0.6 s), and long-term power fluctuations of only 1.8 % rms in a timeframe of >4 h. The spectral bandwidth covers 329 nm at −10 dB, centered around $\lambda = 810.7$ nm, with a corresponding FTL of 6.1 fs. In a DCM-compressor, pulse compression down to an average pulse duration of 7.16 fs is realized, measured over 30 min with only 199 as standard deviation. No active phase-shaping device is used in the whole setup. With more than 70 % of the total energy contained in the main pulse, peak powers as high as 169 GW are reached. Slow CEP-drifts in the system are compensated by a slow-loop feedback system to the oscillator, reducing the remaining CEP fluctuations at the output to <170 mrad rms, only limited by detection noise. On a timescale of ±50 ps around the main pulse, only one post-pulse with an intensity of $I/I_0 = 2.5 \times 10^{-4}$ relative to the main pulse is observed in a THG-AC measurement, which can be eliminated in the future by using slightly wedged OPA-crystals. Apart from the only ∼1 ps-short PSF pedestal, a pulse contrast better than 10^{-7} is obtained.

Those outstanding system characteristics have been partially enabled by operating the poweramplifier deeply in the saturation regime. As a consequence, the beam profile is inhomogeneous and notably modulated, which at first glance represents a drawback of the system design. Detailed characterization of spatial chirp, spectral phase and wavelength-dependent caustic disprove this impression. The presence of a minor spatial chirp does neither prevent pulse compression nor focusabililty of the beam with a high energy confinement in the far field. Above that, all wavelengths are focused within 0.3× the Rayleigh-length. Thanks to the high energy, spot sizes of $w \approx 100$ µm are sufficient to achieve typical HHG intensities of 10^{15} W/cm^2. The observed increase of M^2 values to ∼3 can thus be readily compensated by decreasing the ROC of the focusing optics, which might be even beneficial if a compact setup is required.

With the obtained parameters, the developed OPCPA system is able to replace the Ti:Sa-based pump lasers and their associated pulse-shortening setups in state-of-the-art attosecond beamlines such as [29, 41, 52, 92]. In many of those beamlines, most of the pump parameters are even outperformed by the OPCPA.

7. High Harmonic Generation

The suitability of the developed OPCPA system for HHG is tested in a first experiment. This chapter presents the experimental setup and the acquired results.

7.1. Experimental Setup

Figure 7.1 presents a schematic of the experimental setup used to generate and characterize high harmonics in Neon, utilizing the OPCPA system as the pump source.

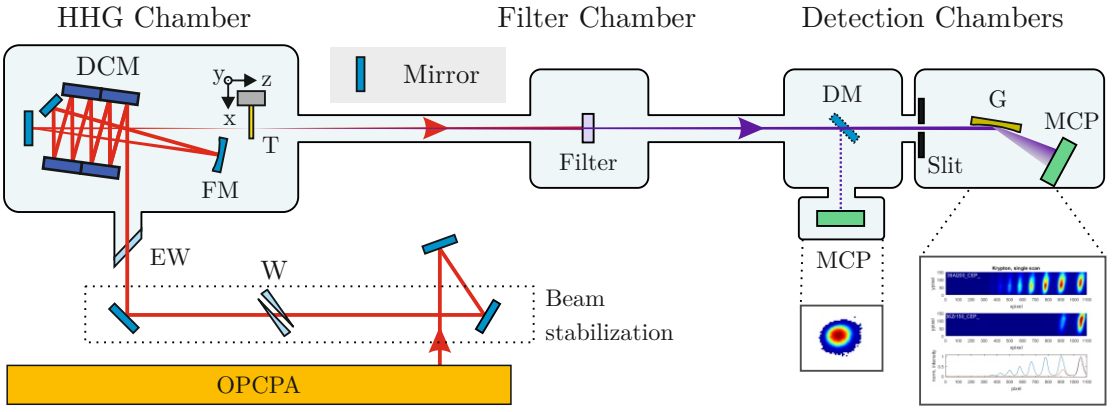

Figure 7.1.: Schematic of the experimental setup used for generation and characterization of high harmonics in Neon. The light blue area is located in vacuum. W: wedge pair, EW: vacuum entrance window, DCM: double-chirped mirror compressor, FM: focusing mirror, T: target, DM: removable deflection mirror, MCP: microchannel plate detector, G: XUV-grating.

After exiting the amplifier, the beam passes a beam stabilization system that is primarily used to guarantee reproducible alignment into the setup and furthermore allows the compensation of thermal drifts arising from within the OPCPA during the day. A pair of fused silica wedges is inserted into the beam under Brewster's angle in order to adjust dispersion and CEP of the pulses without the need to open the cover of the amplifier to access the

internal wedge pair, which would disturb the thermal equilibrium. A 1 mm-thin calcium fluoride window mounted under Brewster's angle marks the entrance to the vacuum. Final pulse compression is performed inside the vacuum chamber by passing two DCM pairs with a total of four bounces per pair, while the number of bounces inside the OPCPA system has been reduced accordingly. This approach is chosen to prevent nonlinear effects in air and degradation of the entrance window due to high laser-intensities [11]. The collimated beam with a $1/e^2$-radius of $w \approx 4.7\,\mathrm{mm}$ is focused to a spotsize of $w_f \approx 100\,\mu\mathrm{m}$ by a spherical mirror with ROC = 1400 mm. Assuming transmission of the complete available energy of 1.8 mJ to the HHG, this results in an intensity of $\sim 10^{15}\,\mathrm{W/cm^2}$. In the focal plane, a ceramic target nozzle with an inner diameter of 1 mm and a circular aperture of 300 µm is placed which confines the interacting gas and allows to achieve gas backing pressures of a few hundred millibar while maintaining 1×10^{-2} mbar vacuum pressure in the remaining part of the HHG-chamber. To optimize the target position, the nozzle is mounted on a motorized XYZ-stage. In the filter chamber, aluminum (Al) or zirconium (Zr) thin-foil filters are used to separate the fundamental from the generated XUV beam. Finally, the harmonics are characterized spatially and spectrally in the detection chambers by means of a microchannel plate (MCP) (MCP-45-2-40-P43-CF100, German Image Detector Systems GmbH) which is imaged by a camera (C920, Logitech) and a home-built XUV-spectrometer. A removable deflection mirror is used to switch between the devices.

Due to losses on the intermediate optics, pulse energies of only 0.87 mJ are measured at the target, reducing the intensity in the focal plane to $\sim 5 \times 10^{14}\,\mathrm{W/cm^2}$. The reason for the energy decrease of >50 % are contaminated surfaces of the optical components inside the HHG-chamber. Because the ceramic nozzle was not available at the beginning, a steel nozzle was used in the early phase of the experiments that suffered continuous material ablation caused by alignment and drift of the OPCPA. The generated metal particles finally attach to the optics, forming a thin, absorbing layer which degrades the overall reflectivity and eventually leads to damages in the coating. In addition, a lack of heat transfer and the disability of the employed silver-coated mirrors to withstand high powers lead to the appearance of burned spots, especially on the folding mirror between target and focusing mirror, where the beam size is smallest. The example of a contaminated DCM is shown in figure 7.2. Although with the change towards the ceramic nozzle all contaminated mirrors have been replaced, key components such as the DCM and the focusing mirror had to remain, because substitutes were not available.

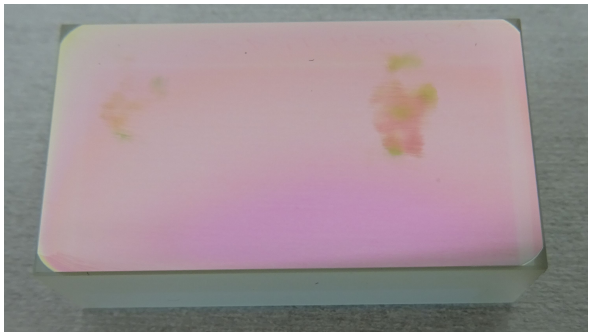

Figure 7.2.: Example of a contaminated DCM surface. The stains are located at the former beam positions.

The described experimental setup is used for all the herefater presented experiments. The optimum z-position of the target and the gas backing pressure are determined by maximizing the signal on the first MCP after a 150 nm-thin Zr-filter. This on-axis phase matching is typically associated with an optimization for the short trajectories [83]. In this configuration, the target is usually located not in the direct focus point, but shortly after the focal plane, where the atomic dispersion can compensate for the Gouy phase of the focused laser beam. However, a specific target position cannot be determined because the exact focal position in the experiment is unknown.
As soon as a stable and intense harmonic signal is obtained, the deflecting mirror is removed from the beam path and the signal is transmitted to the XUV-spectrometer. The schematic setup of the XUV-spectrometer is depicted in figure 7.3. After the signal passes an adjustable slit controlling the resolution versus the photon flux, it is diffracted by a grating (Shimadzu 30-002, 1200 lines/mm) onto a chevron-type MCP (Beam Imaging Solutions, B0S-40-IAA-CH-MS). The spectrum is converted to the visible via a phosphor screen (Beam Imaging Solutions, P-43), which is imaged by a camera (UI-5240CP-M-GL, Image Development Systems GmbH).

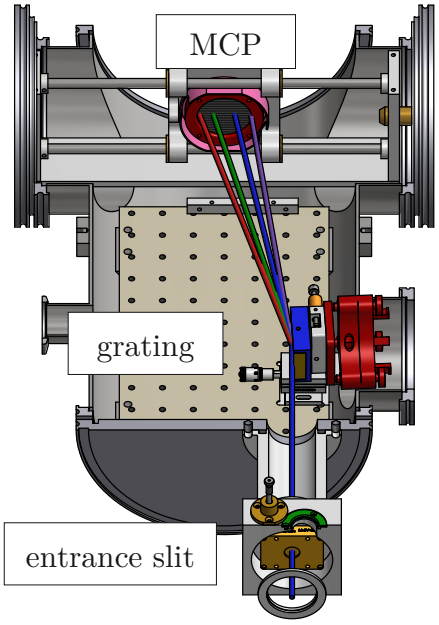

Figure 7.3.: Schematic setup of the XUV-spectrometer. After passing an adjustable slit, a grating mounted under grazing incidence diffracts the beam to an MCP, where the spectrum is converted to the visible with a phosphor screen which is imaged by a camera (not shown). Graphic provided by Thomas Gaumnitz, ETH Zurich.

7.2. Results

7.2.1. HHG Spectrum

Photon energies up to 93 eV are observed in the generated spectrum, corresponding to harmonics of 61st order as shown in figure 7.4.

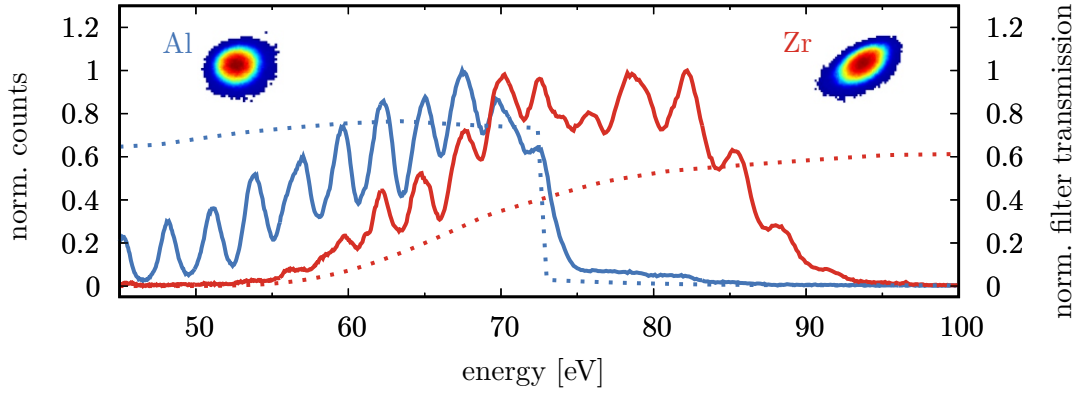

Figure 7.4.: HHG spectrum and spatial beam profile in Neon, measured after spectral filtering with Al (red) and Zr (blue). The respective filter transmission curves are indicated as dotted lines. A cut-off energy of 93 eV is reached.

The blue line represents the detected spectrum, filtered by a 200 nm-thin Al-filter, while the red line represents the spectrum filtered by a 150 nm-thin Zr-filter. The filter transmission curves, which are used for calibration, are indicated as dotted lines. According to the transmittance of each filter, different regions of the spectrum can be observed. In addition, the beam profiles after each filter are shown.
Although no means have been implemented to compensate for spatiotemporal or spatiospectral effects, the homogenous beam profiles indicate a well phase matched process. No attosecond lighthouse effect [114] occured in the experiment, which indicates that the spatial chirp is negligible in the context of HHG. The minor astigmatism and the chromatic aberration of the fundamental beam observed in section 6.8.1 do not seem to affect the HHG process and the selection of the short trajectories as well. Astigmatism only results in a slightly elliptic shape of the high harmonic beam profile, while the chromatic aberration is too small in comparison to induce any detectable effect on the spectrum of the harmonics. Primarily, both effects result in a lower intensity of the fundamental beam in the focal plane. The fact that high harmonics are generated at the preset intensity and with a homogeneous beam profile suggests that the existing impurities do not notably impair the far field beam quality and affect the phase matching conditions. Therefore, comparable conversion efficiencies to other state-of-the-art HHG sources on the order of 1×10^{-9}, considering a 1 % energy bandwidth in the plateau regime, are expected [22].

Higher cut-off energies can potentially be achieved in an optimized setup with increased energy transmission, optimized focal spot size and compensated beam astigmatism by means of cylindrical mirrors.

7.2.2. CEP Dependency

In a second experiment, the characteristic dependency of the harmonic spectra on the CEP with a π-period is validated [7]. To that end, several spectra are recorded with different CEP offsets in the range from 0 to π in steps of 0.3 rad. Controlled CEP-changes are realized by adding an offset to the setpoint of the slow-loop CEP-stabilization. The acquired spectra, filtered by a 150 nm-thin Zr-foil for isolating the harmonics above 60 eV, are shown in figure 7.5 (a).

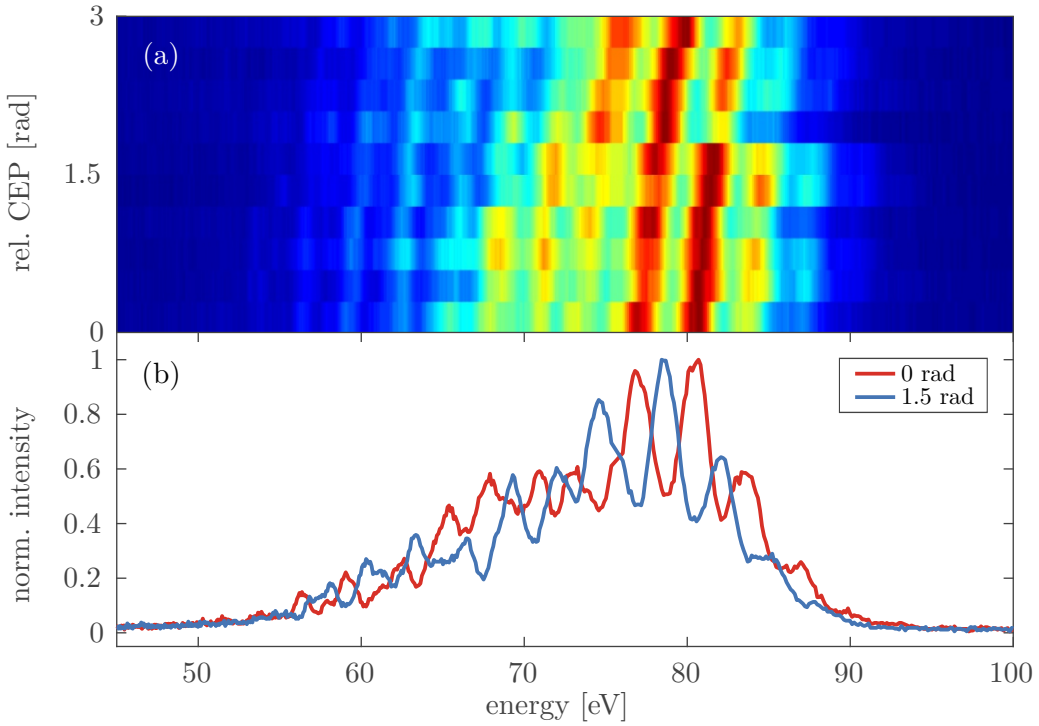

Figure 7.5.: (a) HHG spectra as a function of the relative CEP of the driving OPCPA pulses. The π-period of the spectral peaks is clearly visible. (b) Lineouts of two HHG spectra with a CEP change of $\sim \pi/2$ between them.

The CEP-dependent shift of the harmonic peaks with a π-period is clear and in good agreement with the literature for few-cycle, CEP-stabilized pulses [7, 71]. In (b), the anticipated shift from even to odd harmonics, induced by a relative CEP-offset of $\pi/2$, is illustrated. A distinct cut-off is not visible from the obtained data, which is attributed to the low SNR of the measurement.

With CEP-stability and -control being proved, the system brings all requirements to be used in pump-probe experiments.

7.3. Summary

HHG in Neon has been successfully demonstrated in a proof-of-principle experiment. Although less than 50 % of the initial pulse energy were available at the target, reducing the intensity to $\sim 5 \times 10^{14}\,\mathrm{GW/cm^2}$, photon energies up to 93 eV are generated. Spatiotemporal and spatiospectral effects do not seem to impair the process, as indicated by

the homogeneous beam profiles and the absence of the attosecond lighthouse effect. Full CEP-control of the fundamental pulse is proven by the characteristic shift of the high harmonic peak positions with varying CEP offset. Further enhancement towards higher photon energies can potentially be achieved by optimizing the energy transmission, adapting the focal spot size and compensating for the remaining impurities of the beam. Even without those means, the OPCPA system already fulfills the required application purpopse without difficulty.

8. Conclusion

In this work, the design, implementation and application of a table-top high-energy few-cycle OPCPA system with unique parameters has been presented. Essential subsystems such as the pump source and the pump-seed synchronization have been developed in this context and can be used as standalone systems. The suitability of the system for HHG has been demonstrated in a first experiment and underlines the aspiration of OPCPA technology to replace existing Ti:Sa-based amplifiers in the field of ultrafast physics in the future. The key components of the system are briefly reviewed in the following.

Seed Source

The commercial Ti:Sa-oscillator *venteon dual CEP* from venteon Laser Technologies GmbH acts as the master seed source, simultaneously seeding the OPCPA chain and the regenerative amplifier. Pulse energies of 2.5 nJ at 80 MHz repetition rate are available at the broadband output, centered around 800 nm with a spectral bandwidth exceeding 380 nm at −10 dB and a corresponding FTL below 5 fs. Active CEP stabilization provides a constant carrier-envelope offset of $\pi/4$ with less than 70 mrad rms remaining phase noise at the output. A small fraction of the octave spanning spectrum around 1030 nm is split up to seed the pump source, optically synchronizing both systems.

Thin-Disk Regenerative Amplifier

Amplification to pulse energies up to 28.9 mJ at 6 kHz and a central wavelength of 1030 nm is realized in a regenerative amplifier, designated to pump the OPCPA. The active medium is a Yb-based thin-disk, pumped directly into the zero-phonon line by fiber-coupled diodes at 969 nm with up to 400 W. At optical efficiencies of 44.6 %, 173 W average output power are available after pulse compression to 1.3 ps. Pulse-to-pulse fluctuations below 0.65 % rms, measured over 100 000 consecutive pulses and power fluctuations <0.33 % rms measured over a timespan of 4 h attest an excellent stability. As expected from a thin-disk laser, a superb beam quality with M^2 values of 1.41 and 1.22 in the horizontal and vertical plane is obtained. By careful optimization of the temporal contrast, frequency

doubling with 63 % conversion efficiency could be achieved in a single LBO-based SHG-stage, yielding 104 W (17.3 mJ) at 515 nm .

Pump-Seed Synchronization

The existing timing fluctuations between pump and seed pulses are actively compensated by the PSS. Based on a spectrally resolved OPA, the timing offset is first translated into a spectral shift and subsequently detected by the combination of a transmission grating, a projection lens and a position-sensitive detector. A minimum seed energy of only 4 pJ in combination with 10 μJ pump energy is sufficient to generate the optical error signal, allowing the integration into almost any OPCPA system without sacrificing much energy. In a high-power OPCPA system operated at 300 kHz, pump and seed pulses were synchronized in time with only 2.76±0.04 fs rms remaining timing jitter in a bandwidth between 0.1 Hz to 1 kHz, corresponding to less than 0.2 % of the pump pulse duration. Simultaneously, a detection range of 21 ps is realized, which, to the best of my knowledge, represents the highest dynamic range in a pulse synchronization system today. Integration of the PSS in the herein developed OPCPA system reduces the timing jitter to 9.0±0.01 fs rms or 0.7 % of the pump pulse duration, virtually eliminating timing-related amplification instabilities.

Optical Parametric Chirped Pulse Amplifier

In a three-stage OPCPA system utilizing BBO as the nonlinear interaction medium, the seed pulses are amplified from the sub-nJ level to more than 2 mJ before compression. The spectral bandwidth covers 329 nm at −10 dB around the central wavelength of 810.7 nm, corresponding to a FTL of 6.1 fs. Due to nonlinear effects in air affecting the pump beam, an adapted system design had to be developed to prevent optical damages and detrimental effects on the signal while maintaining picosecond-pump duration and operation in air. Without using an active phase shaping device, the amplified pulses are compressed in a DCM compressor down to an average pulse duration of 7.16 fs with only 199 as standard deviation, measured over 30 min. After compression, pulse energies as high as 1.8 mJ are available at the output, corresponding to 10.8 W average power at the repetition rate of 6 kHz. With more than 70 % of the total energy confined in the main pulse, peak powers of 169 GW are obtained. Slow CEP drifts are detected after compression and compensated by an active feedback to the oscillator, reducing the remaining CEP fluctuations to <169 mrad rms, only limited by detection noise. A temporal contrast better than 10^{-7} is revealed by a THG-autocorrelation on a timescale of ±50 ps around the main pulse outside the ∼1 ps-short PSF-pedestal, exhibiting only one weak post-pulse after 21 ps. Long-term energy and power fluctuations are below 1.8 % rms, evaluated over >4 h, while on a short timescale, pulse-to-pulse fluctuations below 1 % rms are measured within 4000 consecutive samples. Those outstanding system characteristics are partially enabled by operating the final poweramplifier deeply in the saturation regime, which results in a modulated near field beam profile and an increased M^2. Careful analysis of spatial chirp, spectral phase and wavelength-dependent caustic attest no additional detrimental influence on the signal beam. Neither temporal pulse compression nor focusability with a high energy confinement

in the far field is prevented. Thanks to the high pulse energies, the increased M^2 values can be readily compensated by decreasing the ROC of the focusing optics, which might be even beneficial for a compact experimental setup.

In a first proof-of-principle experiment, the OPCPA system was used to generate high harmonics in neon. Despite a reduced on-target energy of 0.87 mJ due to transmission losses in the beamline and a corresponding intensity decrease in the focal plane to $\sim 5 \times 10^{14}\,\mathrm{W/cm^2}$, photon energies up to 93 eV could be achieved. Good phase matching is attested by homogeneous high-harmonic beam profiles. No influence of spatiotemporal or spatiospectral impurities of the fundamental beam on the HHG process could be observed. The characteristic dependency of the high-harmonic spectrum on the CEP with a π-period could be verified experimentally, proving the full CEP control of the system. Even without the planned improvements presented in the following chapter, the OPCPA system already fulfills all requirements to replace existing Ti:Sa-amplifier in attosecond pump-probe-experiments and other ultrafast applications.

9. Outlook

In the near future, the following improvements are planned to enhance the overall system performance:

- *Replacement of the seed source*
  To reduce the system complexity, the seed will be be directly derived from the picosecond-pulses of the regenerative amplifier. Cross-polarized wave-generation, followed by WLG and DFG allows the generation of a broadband, passively CEP-stabilized continuum covering a wavelength range between 450 nm and 2800 nm by employing ∼1.6 mJ of the fundamental pulse energy [28]. Employing such a scheme would not only replace the current seed source, but in addition eliminate the need for a pump-seed synchronization thanks to the massively reduced path-length differences.

- *Improved beam-pointing stabilization*
  As discussed in section 6.6.5, the OPCPA long-term stability is currently impaired by the inadequate active beam-pointing stabilization of the pump beam. This will be replaced in the future by an in-house development with an increased position fidelity. In addition, imaging pump and seed to the OPA stages could add improved pointing stability.

- *Chirped pump pulse*
  It has become apparent that nonlinear effects affecting the intense pump beam during propagation in air represent a serious challenge to the design of a high-energy OPCPA system. Stretching the pump pulses in time reduces the peak power and thus decreases the influence of nonlinearities, which in turn allows for a simplified system design. Simultaneously, an increased conversion efficiency and an improved beam quality are expected. However, the dispersion concept has to be adjusted accordingly to account for the increased pulse durations.

- *Alternative CEP detection*
  The noisy detection scheme in an f-to-2f interferometer based on WLG will be replaced by a more accurate scheme. This could be an 3f-to-2f interferometer or a direct beating of suitable residual spectral components generated in the OPA process, as demonstrated e.g. in [35].

After the aforementioned features have been successfully integrated, the next step in OPCPA development is a further increase of pulse energy and average power by utilizing the next generation of powerful pump lasers. Right now, those systems are approaching the kW-regime, delivering pulse energies of several hundreds of mJ with near-diffraction limited beam quality [68,90,105], bearing the potential to lift OPCPA development to the next level.

List of Figures

1.1. Simplified interrelationship between the core components of the OPCPA systems and the resulting structure of this thesis. 3

2.1. DFG/OPA interaction geometry and energy-level description. 7
2.2. Interaction geometry and phase matching curves in the noncollinear configuration. 9
2.3. Representation of the CEP in the time and frequency domain. 13
2.4. The three-step model of high harmonic generation. 14

3.1. Schematic layout of the venteon dual CEP. 18
3.2. CEP noise analysis of the seed source. 18
3.3. Measured output spectrum and compressed pulse of the seed source. 19

4.1. Basic concept of the disk-laser head. 22
4.2. Thin-disk laser head by TRUMPF Laser GmbH + Co. KG and pump spot on the disk. 23
4.3. Basic concept of a regenerative amplifier. 24
4.4. Ring cavity design of the regenerative amplifier. 26
4.5. B-Integral calculated for amplification of a chirped 600 ps-pulse in the designed cavity. 27
4.6. Schematic layout of the regenerative amplifier. 28
4.7. Seed spectrum and amplified spectrum before compression of the regenerative amplifier. 29
4.8. Regenerative amplifier autocorrelation trace and amplification characteristics after compression. 30
4.9. Bifurcation diagram of the regenerative amplifier. 31
4.10. M^2 measurement of the regenerative amplifier and selected beam profiles. . 32
4.11. M^2 measurement of the regenerative amplifier and selected beam profiles after optimization with a tilted lens. 33
4.12. Beam profile at the regenerative amplifier output. 33
4.13. Cavity leakage around the main pulse with optimized PC settings and at a 5 % reduced voltage. 34
4.14. THG-AC of the regenerative amplifier at low pump power, utilizing different pre-amplification configurations. 35
4.15. Impression of the regenerative amplifier. 36

4.16. Typical output power over time of the regenerative amplifier. 36
4.17. Beam pointing and resonator ambient temperature over time of the regenerative amplifier. 37
4.18. Conversion characteristics and autocorrelation trace of a single SHG stage, employed after the regenerative amplifier. 38

5.1. Exemplary evolution of the relative timing delay between pump and seed pulse without active synchronization. 42
5.2. Concept of intensity cross-correlation. 43
5.3. Concept of balanced optical cross-correlation. 43
5.4. Concept of spectrally resolved cross-correlation. 44
5.5. Schematic setup of the PSS, based on SR-OPA. 46
5.6. Determination of the minimum seed pulse energy. 47
5.7. Measured spectral system behavior of the PSS. 48
5.8. Calculated system behavior of PSS_{α}. 50
5.9. Calculated system behavior of PSS_{β} and $PSS_{\beta,2}$. 50
5.10. Measured PSD characteristics. 51
5.11. PSS_{α} calibration results using the large delay method. 53
5.12. PSS_{β} calibration results using the large delay method. 54
5.13. Short-term timing jitter with and without synchronization. 55
5.14. Power spectral density and integrated timing jitter in PSS_{α}. 56
5.15. Comparison between PSS in-loop and out-of-loop performance. 57
5.16. Beam pointing of the pump source in the SR-OPA crystal plane. 58
5.17. Detection unit and delay line of the commercially available PSS. 59

6.1. Broadband phase matching curves of BBO and LBO. 62
6.2. Visualization of the region of significant gain in an OPCPA. 63
6.3. Simulated evolution of the temporal seed pulse shape throughout the amplification stages by applying a positive dispersion concept. 64
6.4. Simulated preamplification dynamics with increasing pump intensity I_p. . . 66
6.5. Simulated PSF evolution at different I_p with and without seed. 67
6.6. Simulated evolution of PSF and signal energy with increasing seed energy. . 68
6.7. Simulated compression of the preamplified pulse at $I_p = 120\,\mathrm{GW/cm^2}$. . . . 68
6.8. Simulated signal energy E_s, FTL and peak power P_p after amplification of increasingly chirped seed pulses. 69
6.9. Preamplification dynamics with increasing pump intensity I_p. 70
6.10. Simulated beam propagation along z of a collimated beam. 71
6.11. Simulated beam propagation of a divergent beam. 73
6.12. Schematic setup of OPCPA concept A. 74
6.13. Frequency doubled pump beam profile at low and high energy. 75
6.14. Schematic setup of OPCPA concept B. 76
6.15. Pump and signal beam profiles of the poweramplification stages. 77
6.16. Signal spectra after amplification in the three OPA stages. 78

6.17. Pulse characteristics after amplification up to OPA 2 and OPA 3, measured with SPIDER. . . . 79
6.18. Schematic setup of OPCPA concept C. . . . 80
6.19. Measured characteristics of SHG 3 under the influence of strong and weak nonlinear effects. . . . 82
6.20. Pump beam profiles in the poweramplification stages OPA 2 and OPA 3 at low and high energy. . . . 82
6.21. Signal spectra after amplification in the three OPA stages. . . . 83
6.22. Amplification characteristics in OPA 2 and OPA 3. . . . 84
6.23. Pulse characteristics after amplification in OPA 2 and OPA 3 and long-term pulse duration measurement, measured with SPIDER. . . . 86
6.24. Long-term power measurement of the OPCPA output. . . . 87
6.25. Parallel measurement of OPCPA output power and beam pointing. . . . 88
6.26. Schematic setup of the common path f-to-2f interferometer for CEP detection. 89
6.27. Typical interferogram detected in the f-to-2f interferometer. . . . 90
6.28. CEP behaviour detected by the f-to-2f interferometer without and with activated feedback. . . . 90
6.29. Near and far field beam profile of the OPCPA and beam caustic in horizontal and vertical axis at different wavelengths. . . . 92
6.30. Spatially resolved spectral distribution throughout the OPCPA near field beam profile. . . . 93
6.31. Third-harmonic autocorrelation of the OPCPA output. . . . 94

7.1. Schematic of the experimental setup used for generation and characterization of high harmonics in various gases. . . . 97
7.2. Example of a contaminated DCM surface. . . . 98
7.3. Schematic setup of the XUV-spectrometer. . . . 99
7.4. HHG spectrum and spatial beam profile in neon. . . . 100
7.5. HHG spectrum as a function of the relative CEP of the driving pulses. . . . 101

B.1. Schematic setup of the THG-AC. . . . 130
B.2. Linearity of the THG-AC detection system. . . . 131

List of Tables

4.1. Distances and optical elements used in the regenerative amplifier cavity. . . 26

5.1. Differing parameters between the PSS systems. 55

6.1. Concept B: Experimental parameters in the three OPA stages. 76
6.2. Concept C: Experimental parameters for second harmonic generation in the three SHG stages. 81
6.3. Concept C: Experimental parameters in the three OPA stages. 82

B.1. Differing key components of the setup in both configurations. 131

List of acronyms

PSS$_\alpha$	PSS system, implemented in the μJ-OPCPA
PSS$_{\beta,2}$	PSS system, temporary used in the mJ-OPCPA
PSS$_\beta$	PSS system, implemented in the mJ-OPCPA
Al	aluminum
AR	anti-reflection
ASE	amplified spontaneous emission
BBO	β-barium borate, $Ba(BO_2)_2$
CEP	carrier-envelope phase
CFBG	chirped fiber Bragg grating
CPA	chirped-pulse amplification
DCM	double-chirped mirror
DFG	difference-frequency generation
FA	fiber amplifier
FTL	Fourier-transform limit
FWHM	full-width-at-half-maximum
FWM	four-wave mixing
GD	group delay
GDD	group-delay dispersion
GVD	group-velocity dispersion
GVM	group-velocity mismatch
HHG	high-harmonic generation

HR highly reflective

LBO lithium triborate, LiB_3O_5

MCP microchannel plate

OPA optical parametric amplification

OPCPA optical parametric chirped pulse amplification

PC Pockels cell

PI proportional-integral

PSD position-sensitive detector

PSF parametric superfluorescence

PSS pump-seed synchronization

PVWC Poynting-vector-walk-off compensation

PwrSD power spectral density

rms root-mean-square

ROC radius of curvature

SFG sum-frequency generation

SHG second-harmonic generation

SNR signal-to-noise ratio

SPM self-phase modulation

SR-OPA spectrally-resolved optical parametric amplification

TFP thin-film polarizer

THG third-harmonic generation

THG-AC third-harmonic-generation autocorrelator

Ti:Sa Titanium-sapphire

TOD third-order dispersion

TPM tangential-phase matching

WLG white-light generation

XPW cross-polarized wave generation

XUV extreme ultraviolet

Yb ytterbium

Zr zirconium

Bibliography

[1] Coherent Ultrafast-Lasersysteme - Katalog 2016. `https://edge.coherent.com/assets/pdf/2016-Ultrafast-Laser-Systems-Catalog.pdf`. Accessed: 2018-01-22.

[2] J. Ahrens, O. Prochnow, T. Binhammer, T. Lang, B. Schulz, M. Frede, and U. Morgner. Multipass OPCPA system at 100 kHz pumped by a CPA-free solid-state amplifier. *Optics Express*, 24(8):8074–8080, Apr 2016.

[3] Y. Akahane, M. Aoyama, K. Ogawa, K. Tsuji, S. Tokita, J. Kawanaka, H. Nishioka, and K. Yamakawa. High-energy, diode-pumped, picosecond Yb:YAG chirped-pulse regenerative amplifier for pumping optical parametric chirped-pulse amplification. *Optics Letters*, 32(13):1899, 2007.

[4] V. Bagnoud, J. D. Zuegel, N. Forget, and C. Le Blanc. High-dynamic-range temporal measurements of short pulses amplified by OPCPA. *Optics Express*, 15(9):5504, 2007.

[5] A. Baltuška, T. Fuji, and T. Kobayashi. Controlling the Carrier-Envelope Phase of Ultrashort Light Pulses with Optical Parametric Amplifiers. *Physical Review Letters*, 88(13), 2002.

[6] A. Baltuška, T. Fuji, and T. Kobayashi. Visible pulse compression to 4 fs by optical parametric amplification and programmable dispersion control. *Optics Letters*, 27(5):306, 2002.

[7] A. Baltuška, T. Udem, M. Uiberacker, M. Hentschel, E. Goulielmakis, C. Gohle, R. Holzwarth, V. S. Yakovlev, A. Scrinzi, T. W. Hänsch, and F. Krausz. Attosecond control of electronic processes by intense light fields. *Nature*, 421(6923):611–615, 2003.

[8] A. Baltuška, M. Uiberacker, E. Goulielmakis, R. Kienberger, V. S. Yakovlev, T. Udem, T. W. Hansch, and F. Krausz. Phase-controlled amplification of few-cycle laser pulses. *IEEE Journal of Selected Topics in Quantum Electronics*, 9(4):972–989, 2003.

[9] F. Batysta, R. Antipenkov, J. T. Green, J. A. Naylon, J. Novák, T. Mazanec, P. Hříbek, C. Zervos, P. Bakule, and B. Rus. Pulse synchronization system for picosecond pulse-pumped OPCPA with femtosecond-level relative timing jitter. *Optics Express*, 22(24):30281, 2014.

[10] R. Berera, R. van Grondelle, and J. T. M. Kennis. Ultrafast transient absorption spectroscopy: Principles and application to photosynthetic systems. *Photosynthesis Research*, 101(2):105–118, 2009.

[11] B. Bernhardt, A. Ozawa, A. Vernaleken, I. Pupeza, J. Kaster, Y. Kobayashi, R. Holzwarth, E. Fill, F. Krausz, T. W. Hänsch, and T. Udem. Vacuum ultraviolet frequency combs generated by a femtosecond enhancement cavity in the visible. *Optics Letters*, 37(4):503–505, 2012.

[12] D. Blazquez-Sanchez, B. Weichelt, A. Austerschulte, A. Voss, T. Graf, A. Killi, H.-C. Eckstein, M. Stumpf, A. L. Matthes, and U. D. Zeitner. Improving the brightness of a multi-kilowatt single thin-disk laser by an aspherical phase front correction. *Optics Letters*, 36(6):799–801, 2011.

[13] S. Bohman, A. Suda, T. Kanai, S. Yamaguchi, and K. Midorikawa. Generation of 5.0 fs, 5.0 mJ pulses at 1kHz using hollow-fiber pulse compression. *Optics Letters*, 35(11):1887–1889, 2010.

[14] R. W. Boyd. *Nonlinear optics*. Academic Press, Burlington, MA, 3rd edition, 2008.

[15] R. Budriunas, T. Stanislauskas, J. Adamonis, A. Aleknavičius, G. Veitas, D. Gadonas, S. Balickas, A. Michailovas, and A. Varanavičius. 53 W average power CEP-stabilized OPCPA system delivering 55 TW few cycle pulses at 1 kHz repetition rate. *Optics Express*, 25(5):5797, 2017.

[16] G. Cerullo and S. de Silvestri. Ultrafast optical parametric amplifiers. *Review of Scientific Instruments*, 74(1):1, 2003.

[17] C. Chen. *Nonlinear optical borate crystals: Principles and applications*. Wiley-VCH, Weinheim, Germany, 2012.

[18] Corkum. Plasma perspective on strong field multiphoton ionization. *Physical Review Letters*, 71(13):1994–1997, 1993.

[19] A. Couairon, M. Franco, G. Méchain, T. Olivier, B. Prade, and A. Mysyrowicz. Femtosecond filamentation in air at low pressures: Part I: Theory and numerical simulations. *Optics Communications*, 259(1):265–273, 2006.

[20] X. Dangpeng, W. Jianjun, L. Mingzhong, L. Honghuan, Z. Rui, D. Ying, D. Qinghua, H. Xiaodong, W. Mingzhe, D. Lei, and T. Jun. Weak etalon effect in wave plates can introduce significant FM-to-AM modulations in complex laser systems. *Optics Express*, 18(7):6621–6627, 2010.

[21] S. Demmler, J. Rothhardt, S. Hädrich, J. Bromage, J. Limpert, and A. Tünnermann. Control of nonlinear spectral phase induced by ultra-broadband optical parametric amplification. *Optics Letters*, 37(19):3933–3935, 2012.

[22] S. Demmler, J. Rothhardt, S. Hädrich, M. Krebs, A. Hage, J. Limpert, and A. Tünnermann. Generation of high-photon flux-coherent soft x-ray radiation with few-cycle pulses. *Optics Letters*, 38(23):5051–5054, 2013.

[23] J. Dörring, A. Killi, U. Morgner, A. Lang, M. Lederer, and D. Kopf. Period doubling and deterministic chaos in continuously pumped regenerative amplifiers. *Optics Express*, 12(8):1759–1768, Apr 2004.

[24] G. Doumy, F. Quéré, O. Gobert, M. Perdrix, P. Martin, P. Audebert, J. C. Gauthier, J.-P. Geindre, and T. Wittmann. Complete characterization of a plasma mirror for the production of high-contrast ultraintense laser pulses. *Physical Review E*, 69:026402, Feb 2004.

[25] R. Ell, U. Morgner, F. X. Kärtner, J. G. Fujimoto, E. P. Ippen, V. Scheuer, G. Angelow, T. Tschudi, M. J. Lederer, A. Boiko, and B. Luther-Davies. Generation of 5-fs pulses and octave-spanning spectra directly from a Ti:Sapphire laser. *Optics Letters*, 26(6):373, 2001.

[26] T. Y. Fan. Heat generation in Nd:YAG and Yb:YAG. *IEEE Journal of Quantum Electronics*, 29(6):1457–1459, 1993.

[27] H. Fattahi, C. Skrobol, M. Ueffing, Y. Deng, A. Schwarz, Y. Kida, V. Pervak, T. Metzger, Z. Major, and F. Krausz. High efficiency, multi-mJ, sub 10 fs, optical parametric amplifier at 3 kHz. In *Quantum Electronics and Laser Science Conference*, OSA technical digest (online), page CTh1N.6, Washington, DC, 2012. OSA, The Optical Society.

[28] H. Fattahi, H. Wang, A. Alismail, G. Arisholm, V. Pervak, A. M. Azzeer, and F. Krausz. Near-PHz-bandwidth, phase-stable continua generated from a Yb:YAG thin-disk amplifier. *Optics Express*, 24(21):24337, 2016.

[29] F. Frank, C. Arrell, T. Witting, W. A. Okell, J. McKenna, J. S. Robinson, C. A. Haworth, D. Austin, H. Teng, I. A. Walmsley, J. P. Marangos, and J. W. G. Tisch. Invited review article: Technology for attosecond science. *The Review of Scientific Instruments*, 83(7):071101, 2012.

[30] A. Giesen, H. Hügel, A. Voss, K. Wittig, U. Brauch, and H. Opower. Scalable concept for diode-pumped high-power solid-state lasers. *Applied Physics B*, 58(5):365–372, 1994.

[31] A. Giesen and J. Speiser. Fifteen Years of Work on Thin-Disk Lasers: Results and Scaling Laws. *IEEE Journal of Selected Topics in Quantum Electronics*, 13(3):598–609, 2007.

[32] A. Giree, M. Mero, G. Arisholm, Vrakking, Marc J. J., and F. J. Furch. Numerical study of spatiotemporal distortions in noncollinear optical parametric chirped-pulse amplifiers. *Optics Express*, 25(4):3104–3121, 2017.

[33] E. Goulielmakis, M. Schultze, M. Hofstetter, V. S. Yakovlev, J. Gagnon, M. Uiberacker, A. L. Aquila, E. M. Gullikson, D. T. Attwood, R. Kienberger, F. Krausz, and U. Kleineberg. Single-cycle nonlinear optics. *Science*, 320(5883):1614–1617, 2008.

[34] S. Hadrich, J. Rothhardt, M. Krebs, S. Demmler, J. Limpert, and A. Tunnermann. Improving carrier-envelope phase stability in optical parametric chirped-pulse amplifiers by control of timing jitter. *Optics Letters*, 37(23):4910–4912, 2012.

[35] S. Hädrich, J. Rothhardt, M. Krebs, S. Demmler, J. Limpert, and A. Tünnermann. Improving carrier-envelope phase stability in optical parametric chirped-pulse amplifiers by control of timing jitter. *Optics Letters*, 37(23):4910–4912, Dec 2012.

[36] Hanieh Fattahi. *Third-generation femtosecond technology.* PhD thesis, LMU, München, 2014.

[37] M. Hentschel, R. Kienberger, C. Spielmann, G. A. Reider, N. Milosevic, T. Brabec, P. Corkum, U. Heinzmann, M. Drescher, and F. Krausz. Attosecond metrology. *Nature*, 414(6863):509–513, 2001.

[38] D. Herrmann, L. Veisz, R. Tautz, F. Tavella, K. Schmid, V. Pervak, and F. Krausz. Generation of sub-three-cycle, 16 TW light pulses by using noncollinear optical parametric chirped-pulse amplification. *Optics Letters*, 34(16):2459, 2009.

[39] N. Hodgson and H. Weber. *Optical Resonators: Fundamentals, Advanced Concepts and Applications.* Springer London, London, 1997.

[40] C. Homann and E. Riedle. Direct measurement of the effective input noise power of an optical parametric amplifier. *Laser & Photonics Reviews*, 7(4):580–588, 2013.

[41] M. Huppert, I. Jordan, and H. J. Wörner. Attosecond beamline with actively stabilized and spatially separated beam paths. *The Review of Scientific Instruments*, 86(12):123106, 2015.

[42] N. Ishii, C. Y. Teisset, T. Fuji, S. Kohler, K. Schmid, L. Veisz, A. Baltuška, and F. Krausz. Seeding of an eleven femtosecond optical parametric chirped pulse amplifier and its Nd^{3+} picosecond pump laser from a single broadband Ti:Sapphire oscillator. *IEEE Journal of Selected Topics in Quantum Electronics*, 12(2):173–180, 2006.

[43] J. Itatani, J. Faure, M. Nantel, G. Mourou, and S. Watanabe. Suppression of the amplified spontaneous emission in chirped-pulse-amplification lasers by clean high-energy seed-pulse injection. *Optics Communications*, 148(1):70 – 74, 1998.

[44] Joachim Stuiber. *Aufbau und Charakterisierung eines Autokorrelators dritter Ordnung zur Pulsdiagnostik ultrakurzer Laserpulse unter Ausnutzung der SHG und SFG.* Bachelor thesis, Hochschule für angewandte Wissenschaften FH, München, 18.09.2015.

[45] A. Jullien, X. Chen, A. Ricci, J.-P. Rousseau, R. Lopez-Martens, L. P. Ramirez, D. Papadopoulos, A. Pellegrina, F. Druon, and P. Georges. High-fidelity front-end for high-power, high temporal quality few-cycle lasers. *Applied Physics B*, 102(4):769–774, 2011.

[46] A. Jullien, C. G. Durfee, A. Trisorio, L. Canova, J.-P. Rousseau, B. Mercier, L. Antonucci, G. Chériaux, O. Albert, and R. Lopez-Martens. Nonlinear spectral cleaning of few-cycle pulses via cross-polarized wave (XPW) generation. *Applied Physics B*, 96(2):293–299, 2009.

[47] A. Jullien, T. Pfeifer, M. J. Abel, P. M. Nagel, M. J. Bell, D. M. Neumark, and S. R. Leone. Ionization phase-match gating for wavelength-tunable isolated attosecond pulse generation. *Applied Physics B*, 93(2-3):433–442, 2008.

[48] J. Koerner, C. Vorholt, H. Liebetrau, M. Kahle, D. Kloepfel, R. Seifert, J. Hein, and M. C. Kaluza. Measurement of temperature-dependent absorption and emission spectra of Yb:YAG, Yb:LuAG, and Yb:CaF_2 between 20 °C and 200 °C and predictions on their influence on laser performance. *Journal of the Optical Society of America B*, 29(9):2493, 2012.

[49] F. Krausz and M. I. Stockman. Attosecond metrology: from electron capture to future signal processing. *Nature Photonics*, 8(3):205–213, 2014.

[50] T. Lang, A. Harth, J. Matyschok, T. Binhammer, M. Schultze, and U. Morgner. Impact of temporal, spatial and cascaded effects on the pulse formation in ultra-broadband parametric amplifiers. *Optics Express*, 21(1):949–959, 2013.

[51] M. Lewenstein, P. Balcou, M. Y. Ivanov, A. L'Huillier, and P. B. Corkum. Theory of high-harmonic generation by low-frequency laser fields. *Physical Review A*, 49(3):2117–2132, 1994.

[52] R. Locher, M. Lucchini, J. Herrmann, M. Sabbar, M. Weger, A. Ludwig, L. Castiglioni, M. Greif, M. Hengsberger, L. Gallmann, and U. Keller. Versatile attosecond beamline in a two-foci configuration for simultaneous time-resolved measurements. *The Review of Scientific Instruments*, 85(1):013113, 2014.

[53] B. J. Lurie and P. J. Enright. *Classical feedback control: With MATLAB and Simulink*. Automation and Control Engineering. CRC Press, Boca Raton, FL, 2nd ed (online-ausg.) edition, 2012.

[54] C. Manzoni, S.-W. Huang, G. Cirmi, P. Farinello, J. Moses, F. X. Kartner, and G. Cerullo. Coherent synthesis of ultra-broadband optical parametric amplifiers. *Optics Letters*, 37(11):1880–1882, 2012.

[55] H. Mashiko, K. Oguri, and T. Sogawa. Attosecond pulse generation in carbon K-edge region (284 eV) with sub-250 uJ driving laser using generalized double optical gating method. *Applied Physics Letters*, 102(17):171111, 2013.

[56] J. Matyschok, T. Lang, T. Binhammer, O. Prochnow, S. Rausch, M. Schultze, A. Harth, P. Rudawski, C. L. Arnold, A. L'Huillier, and U. Morgner. Temporal and spatial effects inside a compact and CEP stabilized, few-cycle OPCPA system at high repetition rates. *Optics Express*, 21(24):29656, 2013.

[57] T. Metzger. *High-repetition-rate picosecond pump laser based on an Yb:YAG disk amplifier for optical parametric amplification*. PhD thesis, TU Berlin, Berlin, 2009.

[58] T. Metzger, A. Schwarz, C. Y. Teisset, D. Sutter, A. Killi, R. Kienberger, and F. Krausz. High-repetition-rate picosecond pump laser based on a Yb:YAG disk amplifier for optical parametric amplification. *Optics Letters*, 34(14):2123–2125, Jul 2009.

[59] T. Miura, K. Kobayashi, K. Takasago, Z. Zhang, K. Torizuka, and F. Kannari. Timing jitter in a kilohertz regenerative amplifier of a femtosecond-pulse Ti:Al_2O_3 laser. *Optics Letters*, 25(24):1795–1797, 2000.

[60] J. Moses and S.-W. Huang. Conformal profile theory for performance scaling of ultrabroadband optical parametric chirped pulse amplification. *Journal of the Optical Society of America B*, 28(4):812–831, Apr 2011.

[61] J. Moses, C. Manzoni, S.-W. Huang, G. Cerullo, and F. X. Kärtner. Temporal optimization of ultrabroadband high-energy OPCPA. *Optics Express*, 17(7):5540, 2009.

[62] P. F. Moulton. Spectroscopic and laser characteristics of Ti:Al_2O_3. *Journal of the Optical Society of America B*, 3(1):125, 1986.

[63] J. E. Murray and W. H. Lowdermilk. Nd:YAG regenerative amplifier. *Journal of Applied Physics*, 51(7):3548–3556, 1980.

[64] M. Nisoli, S. de Silvestri, O. Svelto, R. Szipöcs, K. Ferencz, C. Spielmann, S. Sartania, and F. Krausz. Compression of high-energy laser pulses below 5 fs. *Optics Letters*, 22(8):522, 1997.

[65] M. Nisoli, P. Decleva, F. Calegari, A. Palacios, and F. Martin. Attosecond Electron Dynamics in Molecules. *Chemical Reviews*, 2017.

[66] S. Nolte, C. Momma, H. Jacobs, A. Tünnermann, B. N. Chichkov, B. Wellegehausen, and H. Welling. Ablation of metals by ultrashort laser pulses. *Journal of the Optical Society of America B*, 14(10):2716, 1997.

[67] S. Nolte, F. Schrempel, and F. Dausinger. *Ultrashort Pulse Laser Technology*, volume 195. Springer International Publishing, Cham, 2016.

[68] T. Nubbemeyer, M. Kaumanns, M. Ueffing, M. Gorjan, A. Alismail, H. Fattahi, J. Brons, O. Pronin, H. G. Barros, Z. Major, T. Metzger, D. Sutter, and F. Krausz. 1 kW, 200 mJ picosecond thin-disk laser system. *Optics Letters*, 42(7):1381–1384, 2017.

[69] R. Paschotta and U. Keller. Passive mode locking with slow saturable absorbers. *Applied Physics B*, 73(7):653–662, 2001.

[70] M. D. Perry and G. Mourou. Terawatt to petawatt subpicosecond lasers. *Science*, 264(5161):917–924, 1994.

[71] Piotr Rudawski, Anne Harth, Chen Guo, Eleonora Lorek, Miguel Miranda, Christoph M. Heyl, Esben W. Larsen, Jan Ahrens, Oliver Prochnow, Thomas Binhammer, Uwe Morgner, Johan Mauritsson, Anne L'Huillier, Cord L. Arnold. Carrier-envelope phase dependent high-order harmonic generation with a high-repetition rate OPCPA-system. *The European Physical Journal D*, 69:70(69):1434–6060, 2015.

[72] S. Prinz, M. Häfner, C. Y. Teisset, R. Bessing, K. Michel, Y. Lee, X. T. Geng, S. Kim, D. E. Kim, T. Metzger, and M. Schultze. CEP-stable, sub-6 fs, 300-kHz OPCPA

system with more than 15 W of average power. *Optics Express*, 23(2):1388–1394, 2015.

[73] B. S. Rao, A. Moorti, R. Rathore, J. A. Chakera, P. A. Naik, and P. D. Gupta. High-quality stable electron beams from laser wakefield acceleration in high density plasma. *Physical Review Special Topics - Accelerators and Beams*, 17(1), 2014.

[74] P. Raybaut, F. Balembois, F. Druon, and P. Georges. Numerical and experimental study of gain narrowing in ytterbium-based regenerative amplifiers. *IEEE Journal of Quantum Electronics*, 41(3):415–425, 2005.

[75] ISO Standard 11146. Lasers and laser-related equipment - Test methods for laser beam widths, divergence angles and beam propagation ratios. Norm, International Organization for Standardization, Geneva, Switzerland, 2005.

[76] JCGM 100:2008. Evaluation of measurement data - Guide to the expression of uncertainty in measurement. Guide, Joint Committee for Guides in Metrology, 2008.

[77] A. Renault, F. Augé-Rochereau, T. Planchon, P. D?Oliveira, T. Auguste, G. Chériaux, and J.-P. Chambaret. ASE contrast improvement with a non-linear filtering Sagnac interferometer. *Optics Communications*, 248(4):535 – 541, 2005.

[78] A. Renault, D. Z. Kandula, S. Witte, A. L. Wolf, R. T. Zinkstok, W. Hogervorst, and K. S. E. Eikema. Phase stability of terawatt-class ultrabroadband parametric amplification. *Optics Letters*, 32(16):2363–2365, Aug 2007.

[79] W. H. Renninger and F. W. Wise. Fundamental Limits to Mode-Locked Lasers: Toward Terawatt Peak Powers. *IEEE Journal of Selected Topics in Quantum Electronics*, 21(1):63–70, 2015.

[80] F. Röser, T. Eidam, J. Rothhardt, O. Schmidt, D. N. Schimpf, J. Limpert, and A. Tünnermann. Millijoule pulse energy high repetition rate femtosecond fiber chirped-pulse amplification system. *Optics Letters*, 32(24):3495, 2007.

[81] I. N. Ross, P. Matousek, G. H. C. New, and K. Osvay. Analysis and optimization of optical parametric chirped pulse amplification. *Journal of the Optical Society of America B*, 19(12):2945, 2002.

[82] J. Rothhardt, S. Demmler, S. Hädrich, J. Limpert, and A. Tünnermann. Octave-spanning OPCPA system delivering CEP-stable few-cycle pulses and 22 W of average power at 1 MHz repetition rate. *Optics Express*, 20(10):10870–10878, May 2012.

[83] P. Salières, B. Carré, L. Le Déroff, F. Grasbon, G. G. Paulus, H. Walther, R. Kopold, W. Becker, D. B. Milosević, A. Sanpera, and M. Lewenstein. Feynman's path-integral approach for intense-laser-atom interactions. *Science*, 292(5518):902–905, 2001.

[84] S. M. Saltiel, K. Koynov, B. Agate, and W. Sibbett. Second-harmonic generation with focused beams under conditions of large group-velocity mismatch. *Journal of the Optical Society of America B*, 21(3):591, 2004.

[85] G. Sansone, L. Poletto, and M. Nisoli. High-energy attosecond light sources. *Nature Photonics*, 5(11):655–663, 2011.

[86] C. J. Saraceno, F. Emaury, C. Schriber, M. Hoffmann, M. Golling, T. Südmeyer, and U. Keller. Ultrafast thin-disk laser with 80 muJ pulse energy and 242 W of average power. *Optics Letters*, 39(1):9–12, 2014.

[87] T. R. Schibli, J. Kim, O. Kuzucu, J. T. Gopinath, S. N. Tandon, G. S. Petrich, L. A. Kolodziejski, J. G. Fujimoto, E. P. Ippen, and F. X. Kärtner. Attosecond active synchronization of passively mode-locked lasers by balanced cross correlation. *Optics Letters*, 28(11):947, 2003.

[88] D. N. Schimpf, T. Eidam, E. Seise, S. Hädrich, J. Limpert, and A. Tünnermann. Circular versus linear polarization in laser-amplifiers with Kerr-nonlinearity. *Optics Express*, 17(21):18774–18781, Oct 2009.

[89] M. Schultze, T. Binhammer, G. Palmer, M. Emons, T. Lang, and U. Morgner. Multi-muJ, CEP-stabilized, two-cycle pulses from an OPCPA system with up to 500 kHz repetition rate. *Optics Express*, 18(26):27291–27297, 2010.

[90] M. Schultze, C. Wandt, S. Klingebiel, C. Y. Teisset, M. Häfner, R. Bessing, T. Herzig, S. Prinz, S. Stark, K. Michel, and T. Metzger. Toward Kilowatt-Level Ultrafast Regenerative Thin-Disk Amplifiers. In *Lasers Congress 2016 (ASSL, LSC, LAC)*, page ATu4A.4. Optical Society of America, 2016.

[91] A. Schwarz, M. Ueffing, Y. Deng, X. Gu, H. Fattahi, T. Metzger, M. Ossiander, F. Krausz, and R. Kienberger. Active stabilization for optically synchronized optical parametric chirped pulse amplification. *Optics Express*, 20(5):5557–5565, 2012.

[92] W. Schweinberger, A. Sommer, E. Bothschafter, J. Li, F. Krausz, R. Kienberger, and M. Schultze. Waveform-controlled near-single-cycle milli-joule laser pulses generate sub-10 nm extreme ultraviolet continua. *Optics Letters*, 37(17):3573–3575, 2012.

[93] I. J. Sola, E. Mével, L. Elouga, E. Constant, V. Strelkov, L. Poletto, P. Villoresi, E. Benedetti, J.-P. Caumes, S. Stagira, C. Vozzi, G. Sansone, and M. Nisoli. Controlling attosecond electron dynamics by phase-stabilized polarization gating. *Nature Physics*, 2(5):319–322, 2006.

[94] A. Sommer, E. M. Bothschafter, S. A. Sato, C. Jakubeit, T. Latka, O. Razskazovskaya, H. Fattahi, M. Jobst, W. Schweinberger, V. Shirvanyan, V. S. Yakovlev, R. Kienberger, K. Yabana, N. Karpowicz, M. Schultze, and F. Krausz. Attosecond nonlinear polarization and light-matter energy transfer in solids. *Nature*, 534(7605):86–90, 2016.

[95] A. Stolow, A. E. Bragg, and D. M. Neumark. Femtosecond time-resolved photoelectron spectroscopy. *Chemical reviews*, 104(4):1719–1757, 2004.

[96] D. Strickland and G. Mourou. Compression of amplified chirped optical pulses. *Optics Communications*, 55(6):447 – 449, 1985.

[97] B. Stuart, M. Feit, S. Herman, A. Rubenchik, B. Shore, and M. Perry. Nanosecond-to-femtosecond laser-induced breakdown in dielectrics. *Physical Review B*, 53(4):1749–1761, 1996.

[98] L. Sudrie, A. Couairon, M. Franco, B. Lamouroux, B. Prade, S. Tzortzakis, and A. Mysyrowicz. Femtosecond laser-induced damage and filamentary propagation in fused silica. *Physical Review Letters*, 89(18):186601, 2002.

[99] T. Stanislauskas and I. Balčiunas and V. Tamuliene and R. Budriunas and A. Varanavičius. Analysis of parametric fluorescence amplified in a noncollinear optical parametric amplifier pumped by the second harmonic of a femtosecond Yb:KGW laser. *Lithuanian Journal of Physics*, 56(1):1–8, 2016.

[100] E. J. Takahashi, P. Lan, O. D. Mücke, Y. Nabekawa, and K. Midorikawa. Attosecond nonlinear optics using gigawatt-scale isolated attosecond pulses. *Nature Communications*, 4:2691, 2013.

[101] M. Takeda, H. Ina, and S. Kobayashi. Fourier-transform method of fringe-pattern analysis for computer-based topography and interferometry. *Journal of the Optical Society of America*, 72(1):156–160, Jan 1982.

[102] F. Tavella, A. Marcinkevicius, and F. Krausz. Investigation of the superfluorescence and signal amplification in an ultrabroadband multiterawatt optical parametric chirped pulse amplifier system. *New Journal of Physics*, 8(10):219, 2006.

[103] F. Tavella, Y. Nomura, L. Veisz, V. Pervak, A. Marcinkevičius, and F. Krausz. Dispersion management for a sub-10-fs, 10 TW optical parametric chirped-pulse amplifier. *Optics Letters*, 32(15):2227, 2007.

[104] F. Tavella, K. Schmid, N. Ishii, A. Marcinkevičius, L. Veisz, and F. Krausz. High-dynamic range pulse-contrast measurements of a broadband optical parametric chirped-pulse amplifier. *Applied Physics B*, 81(6):753–756, 2005.

[105] C. Teisset, M. Schultze, R. Bessing, M. Häfner, S. Prinz, D. Sutter, and T. Metzger. 300 W Picosecond Thin-Disk Regenerative Amplifier at 10 kHz Repetition Rate. In *Advanced Solid-State Lasers Congress Postdeadline*, page JTh5A.1. Optical Society of America, 2013.

[106] H. Telle, G. Steinmeyer, A. Dunlop, J. Stenger, D. Sutter, and U. Keller. Carrier-envelope offset phase control: A novel concept for absolute optical frequency measurement and ultrashort pulse generation. *Applied Physics B*, 69(4):327–332, Oct 1999.

[107] A. Thai, C. Skrobol, P. K. Bates, G. Arisholm, Z. Major, F. Krausz, S. Karsch, and J. Biegert. Simulations of petawatt-class few-cycle optical-parametric chirped-pulse amplification, including nonlinear refractive index effects. *Optics Letters*, 35(20):3471–3473, 2010.

[108] Tino Lang. *Ultrashort laser pulses from optical parametric amplifiers and oscillators*. PhD thesis, Leibniz Universität Hannover, Hannover, 2014.

[109] P. Tournois. Acousto-optic programmable dispersive filter for adaptive compensation of group delay time dispersion in laser systems. *Optics Communications*, 140(4-6):245–249, 1997.

[110] J. A. Valdmanis, R. L. Fork, and J. P. Gordon. Generation of optical pulses as short as 27 femtoseconds directly from a laser balancing self-phase modulation, group-velocity dispersion, saturable absorption, and saturable gain. *Optics Letters*, 10(3):131–133, Mar 1985.

[111] K. Varjú, P. Johnsson, J. Mauritsson, A. L'Huillier, and R. López-Martens. Physics of attosecond pulses produced via high harmonic generation. *American Journal of Physics*, 77(5):389–395, 2009.

[112] A. Vaupel, N. Bodnar, B. Webb, L. Shah, and M. Richardson. Concepts, performance review, and prospects of table-top, few-cycle optical parametric chirped-pulse amplification. *Optical Engineering*, 53(5):051507, 2014.

[113] F. Verluise, V. Laude, Z. Cheng, C. Spielmann, and P. Tournois. Amplitude and phase control of ultrashort pulses by use of an acousto-optic programmable dispersive filter:?pulse compression and shaping. *Optics Letters*, 25(8):575–577, Apr 2000.

[114] H. Vincenti and F. Quéré. Attosecond lighthouses: How to use spatiotemporally coupled light fields to generate isolated attosecond pulses. *Physical Review Letters*, 108(11):113904, 2012.

[115] B. L. Volodin, S. V. Dolgy, E. D. Melnik, E. Downs, J. Shaw, and V. S. Ban. Wavelength stabilization and spectrum narrowing of high-power multimode laser diodes and arrays by use of volume Bragg gratings. *Optics Letters*, 29(16):1891, 2004.

[116] I. Walmsley, L. Waxer, and C. Dorrer. The role of dispersion in ultrafast optics. *Review of Scientific Instruments*, 72(1):1–29, 2001.

[117] I. A. Walmsley and C. Dorrer. Characterization of ultrashort electromagnetic pulses. *Advances in Optics and Photonics*, 1(2):308–437, Apr 2009.

[118] B. Weichelt, A. Voss, M. A. Ahmed, and T. Graf. Enhanced performance of thin-disk lasers by pumping into the zero-phonon line. *Optics Letters*, 37(15):3045, 2012.

[119] A. M. Weiner. Femtosecond pulse shaping using spatial light modulators. *Review of Scientific Instruments*, 71(5):1929–1960, 2000.

[120] S. Witte and K. S. E. Eikema. Ultrafast Optical Parametric Chirped-Pulse Amplification. *IEEE Journal of Selected Topics in Quantum Electronics*, 18(1):296–307, 2012.

[121] S. Witte, R. T. Zinkstok, W. Hogervorst, and K. Eikema. Numerical simulations for performance optimization of a few-cycle terawatt NOPCPA system. *Applied Physics B*, 87(4):677–684, 2007.

[122] P. Xi, Y. Andegeko, D. Pestov, V. V. Lovozoy, and M. Dantus. Two-photon imaging using adaptive phase compensated ultrashort laser pulses. *Journal of Biomedical Optics*, 14(1):014002, 2009.

[123] J. Xu and J. R. Knutson. Chapter 8: Ultrafast Fluorescence Spectroscopy via Upconversion. In *Fluorescence Spectroscopy*, volume 450 of *Methods in Enzymology*, pages 159–183. Elsevier, 2008.

[124] D. Yelin, D. Meshulach, and Y. Silberberg. Adaptive femtosecond pulse compression. *Optics Letters*, 22(23):1793–1795, Dec 1997.

Appendix

A. Measurement Devices

In the following, the measurement devices are listed which were used by default to characterize the different properties of the beam, if not stated otherwise in the text. The list is formatted according to

- **Measured property** (optional range) Device type, Model, *Manufacturer*.

In all cases, the energy is obtained by dividing the measured power by the repetition rate.

- **Power** (<3 W) Powermeter, XLP12-3S-H2-D0, *Gentec-EO*
- **Power** (<10 W) Powermeter, UP12E-10S-H5, *Gentec-EO*
- **Power** (<20 W) Powermeter, UP12E-20H-H5, *Gentec-EO*
- **Power** (>20 W) Powermeter, UP55M-500W-H12-DO, *Gentec-EO*
- **Relative Energy** Photodiode, DET-10A, *Thorlabs GmbH*
- **Spectrum** ($\lambda = 1030$ nm) Spectrometer, HR4000, *Ocean Optics, Inc.*
- **Spectrum** ($\lambda = 500$ nm - 1100 nm) Spectrometer, AvaSpec Dual-channel, *Avantes BV*
- **Beam Profile** Beam Profiler, SP620U, *Ophir Spiricon GmbH*
- **Pulse duration** ($\lambda = 515$ nm and 1030 nm) SHG-Autocorrelator, pulseCheck150, *APE GmbH*
- **Pulse duration** (broadband pulses around $\lambda = 800$ nm) SPIDER, Pulse:Four SPIDER, *venteon Laser Technologies GmbH*

B. THG-Autocorrelator

The utilized third-harmonic-generation autocorrelator (THG-AC) was initially designed and set up in the context of the Bachelors thesis of Joachim Stuiber [44]. Excerpts from his work are used in this section with his consent.

Figure B.1 shows the schematic setup of the device, which can be used for the characterization of a narrowband pulse with a fundamental wavelength around 1030 nm, e.g. from the regenerative amplifier or a broadband pulse centered around 800 nm, e.g. from the OPCPA system.

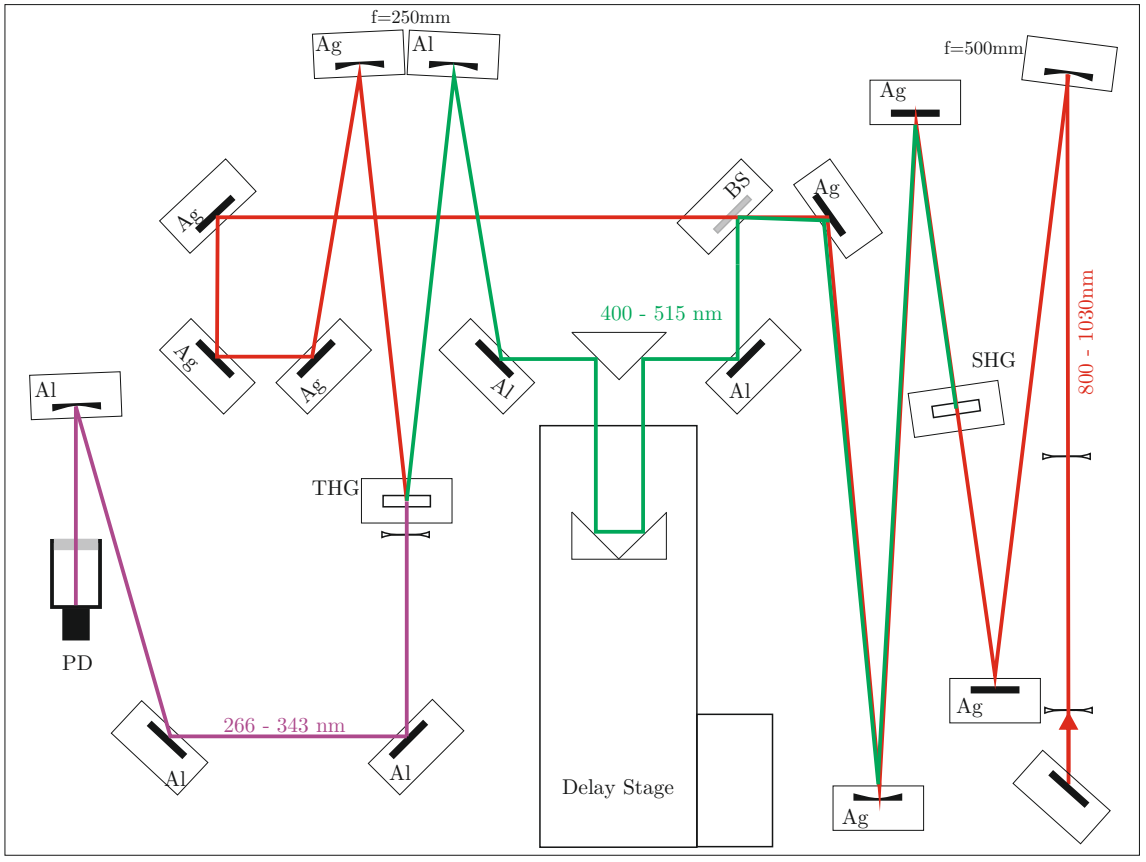

Figure B.1.: Schematic setup of the THG-AC. Ag: silver mirror, SHG: second harmonic generation, BS: beam splitter, Al: aluminum mirror, THG: third harmonic generation, PD: photodiode.

The incoming beam is first frequency doubled in the SHG-stage. A dichroic beamsplitter (DMLP650, Thorlabs GmbH) is used to separate the fundamental and second harmonic beam. Both beams are then guided to the THG-stage, where they overlap under an angle to generate a sum-frequency signal in Type II configuration. The SHG-beam is delayed with respect to the fundamental in minimum steps of 0.7 fs with a maximum range of 167 ps by passing an all-reflective retroreflector, mounted on a delay stage (PI M-126.DG1, Physik Instrumente GmbH). The resulting THG-signal is spatially separated from the other beams and focused on a photodiode for detection (SM05PD2A, Thorlabs GmbH). An additional bandpass filter (FGUV11-UV, Thorlabs GmbH) enclosing the photodiode housing prevents the unwanted detection of straylight. The measured signal

is amplified and converted to a voltage by a photodiode amplifier (PDA200C, Thorlabs GmbH). An Analog-Digital-Converter (UM202, Meilhaus Electronic) allows the transfer and evaluation of the data on a computer with help of a Labview software.
Table B.1 summarizes the differing key components of the setup, used for the characterization of a narrowband signal around 1030 nm and for a broadband signal around 800 nm. The crystal lengths are listed according to the manufacturers calibration report. Both photodiodes are supplied by Thorlabs GmbH.

Table B.1.: Differing key components of the setup as used for the characterization of a narrowband signal around 1030 nm and for a broadband signal around 800 nm.

	$\lambda_c = 1030\,\text{nm}$ (narrowband)	$\lambda_c = 800\,\text{nm}$ (broadband)
SHG crystal	BBO, $\theta = 39.7°$, $L = 1.12\,\text{mm}$	BBO, $\theta = 29.0°$, $L = 0.15\,\text{mm}$
THG crystal	BBO, $\theta = 39.7°$, $L = 1.12\,\text{mm}$	BBO, $\theta = 55.4°$ $L = 0.16\,\text{mm}$
PD	SM05PD2A (Silicon)	SM05PD7A (Gallium phosphide)

The linearity of the system was characterized at 1030 nm by attenuating the signal at a fixed energy using a set of calibrated neutral-density filter. In addition, the linear behavior of the photodiode amplifier was verified by measuring the signal output in dependence of the amplifier gain. Both measurements are presented in figure B.2 (a) and (b), respectively.

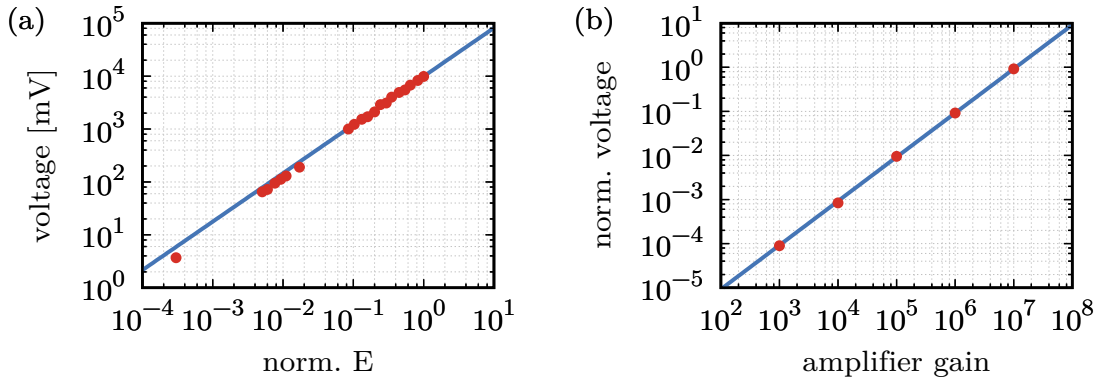

Figure B.2.: Linearity of the THG-AC detection system. (a) Output signal in dependence of incident signal energy E. (b) Output signal in dependence of the photodiode amplifier gain.

In both cases, the output signal linearly follows the input. The small offset from the linear fit in (a) towards lower incident energies is likely caused by the transmission uncertainty in the utilized filters, which is as high as ±5 % and increases at lower transmission values.

In case of the characterization of ultrashort pulses in the few-cycle regime, the system is currently limited by two aspects:

1. *Limited conversion bandwidth*
   Because of the limited phase matching bandwidth, no complete conversion of the fundamental beam is possible in the SHG and THG stage, which results in a loss of information carried in the spectral wings. Utilizing even shorter crystals might circumvent this issue in the future.

2. *Dispersion mismatch*

   Due to the transmission of the utilized dichroic beamsplitter, a significant amount of dispersion is introduced on the fundamental beam, but not on the frequency doubled copy. This dispersion mismatch prevents the exact temporal resolvement of the main pulse and the determination of the pulse contrast regarding the PSF pedestal. Utilizing a balanced beamsplitter (equal dispersion in transmission and reflection) or a spatial separation instead of a spectral one theoretically allows to improve this drawback in the future.

Danksagung

Die vorliegende Disseration entstand an der Fakultät für Physik, Lehrstuhl für Laser- und Röntgenphysik E11 der Technischen Universität München sowie bei der TRUMPF Scientific Lasers GmbH + Co. KG. An dieser Stelle möchte ich mich bei den Menschen bedanken, die auf unterschiedliche Art und Weise zum Gelingen dieser Arbeit beigetragen haben:

- Prof. Reinhard "Reini" Kienberger, für die hervorragende Betreuung dieser Arbeit und dafür, dass deine Türe während meiner gesamten Promotionszeit immer offen stand.
- Tom Metzger, ebenfalls für die ausgezeichnete Betreuung dieser Arbeit, Motivation wenn sie nötig war und den Ansporn, am Ende immer noch ein bisschen mehr rauszukitzeln.
- Marcel Schultze und Matthias Häfner, für eure fachkundige Unterstützung in den Bereichen Optik und Elektronik, das hohe Engagement und die vielen Dinge, die ich bei unserer Zusammenarbeit lernen durfte.
- Robert Bessing und Tobi Herzig, für die Lösung aller denkbaren mechanischen Herausforderungen.
- Sebastian Stark, für den überragenden Code zu nichtlinearer Pulspropagation.
- Catherine Teisset und Christoph Wandt, für die Einführung in die Welt der regenerativen Verstärker.
- Sandro Klingebiel, für gute Gesellschaft beim allmorgendlichen Kaffeeritual und zahlreiche spannende Diskussionen.
- Birgitta Bernhardt, Max Schnitzenbaumer, Denis Potamianos, Pascal Scigalla, Christian Schröder und Vahe Shirvanyan, für die super Zusammenarbeit bei der Durchführung der HHG-Experimente.
- Johann Riemensberger und Wolfram Helml für euer gesamtes Wissen rund um HHG, welches ihr immer gerne bereit wart zu teilen.
- Dem Team von venteon, Thomas, Stefan, Olli, Jan und Hauke, für spitzenmäßigen Support.
- Tino Lang, für die geniale Simulationssoftware chi2D.

- Ludwig Blümel, Martin Wolferstetter und Philipp Heck, für die Unterstützung im Rahmen der Installation der CEP-Stabilisierung.
- Nicolas Forget, for giving me the opportunity to test Dazzler and Wizzler in my system.
- Thomas Gaumnitz und Arohi Jain, für die Möglichkeit zur Nutzung eures XUV-Spektrometers.
- Allen Kollegen am Lehrstuhl für Laser- und Röntgenphysik, für die nette Aufnahme und eine tolle Zeit!
- Dem gesamten Team von TRUMPF Scientific Lasers - ihr seid einzigartig!
- LUR – CHI!
- Meiner Familie, Arne, Birgit, Anja, Fabian, für den uneingeschränkten Rückhalt und eure Unterstützung, auf die man sich immer verlassen kann. Ohne euch geht nichts!
- Den wichtigsten Menschen in meinem Leben - Carina, Henri und Luis. Danke, dass es euch gibt!